

Dark Matter Working Group

recommendation for Two Higgs Doublet

Model (draft title)

Authorlist to be compiled: **Antonio Boveia,**^{3,*}
Caterina Doglioni,^{8,*} **Kristian Hahn,**^{14,*} **Ulrich Haisch,**^{15,16,*} **Steven**
Lowette,²² **Tim M.P. Tait,**^{25,*}

*DMWG organizers

³Ohio State University, 191 W. Woodruff Avenue Columbus, OH 43210

⁸Fysiska institutionen, Lunds universitet, Lund, Sweden

¹⁴Department of Physics and Astronomy, Northwestern University, Evanston, Illinois 60208,
USA

¹⁵Rudolf Peierls Centre for Theoretical Physics, University of Oxford, Oxford, OX1 3PN,
United Kingdom

¹⁶CERN, TH Department, CH-1211 Geneva 23, Switzerland

²²Physics Department, Vrije Universiteit Brussel, Brussels, Belgium

²⁵Department of Physics and Astronomy, University of California, Irvine, California 92697,
USA

Editor's E-mail: antonio.boveia@cern.ch, caterina.doglioni@cern.ch,
kristian.hahn@cern.ch, ulrich.haisch@physics.ox.ac.uk, ttait@uci.edu

Abstract. Draft abstract.

Contents

1	Introduction	1
2	The model	1
2.1	Evolution of theories for Dark Matter searches at colliders	2
2.2	Scalar Model Description	3
3	Model parameters	6
4	Parameter grid	12
4.1	Parameter scans on masses, couplings and mixing angles	12
4.1.1	Results of studies	12
4.1.2	Studies of the $h(bb) + E_T^{\text{miss}}$ signature	13
4.1.3	Studies of the mono-Z (leptonic) signature	24
4.2	Studies of the mono-Z (hadronic) signature	36
4.2.1	Studies of DM+heavy flavor signature	40
4.2.2	Scanning the parameter space	41
4.2.3	Comparison with DMsimp Pseudoscalar Model	43
4.2.4	Recasting existing $tt+E_T^{\text{miss}}$ and $bb+E_T^{\text{miss}}$ signatures	45
4.2.5	Flavour scheme recommendations and studies	47
4.2.6	Motivation for a dedicated $tW+E_T^{\text{miss}}$ search	53
4.2.7	Uncovered signatures with $tth + E_T^{\text{miss}}$	53
4.2.8	Top pair resonant searches	55
4.2.9	Four tops final states	57
4.2.10	2HDM+scalar sensitivity studies	58
4.2.11	Other signatures	60
4.2.12	Monojet	60
4.2.13	Resonant Production at Collider (Comparison)	60
4.2.14	Final proposal for parameter scan	64
5	Connection with cosmology	64
5.1	Pseudoscalar	64
5.2	Technical setup	64
5.3	Results	65
5.4	Scalar	65
6	Comparisons with non-collider experiments	72
6.1	Direct detection	72
6.2	Direct Detection	72
6.2.1	Scalar	72
6.3	Pseudoscalar	73
6.4	Indirect detection	76

1 Introduction

Reasoning behind this effort

- Simplified models only one signature at a time, sometimes not gauge invariant
- One step beyond this: less-simplified models
- Compare and confront different search sensitivity
- Combinations among different signatures
- Find new kinematic regimes / improve searches by exploring different signatures
- Still keeping the choice of model generic enough that this is reusable for theorists

Reasoning behind this effort

- Reasoning behind the choice of model
- Highlights more than one signature at a time, depending on parameters
- Leaves room for new unexplored kinematic signatures within existing searches (left for future work)
- Complete enough, still simplified so that one can choose grid planes
- Existing theory effort (HXSWG)

2 The model

Description of the model

- Citations: [? ? ? ? ?]
- Particles, masses, couplings, mixing angles

Comparison with existing models How does the model compare with other 2HDMs/scalar models (with and without DM).

- Scalar to SSM to 2HDM evolution
- Other models:
 - S. Ipek, D. McKeen, A. Nelson, [?]
 - Bell, Busoni, Sanderson, [?]
 - No, Goncalves, Machado, [? ?]
 - Higgs Cross-section Working Group

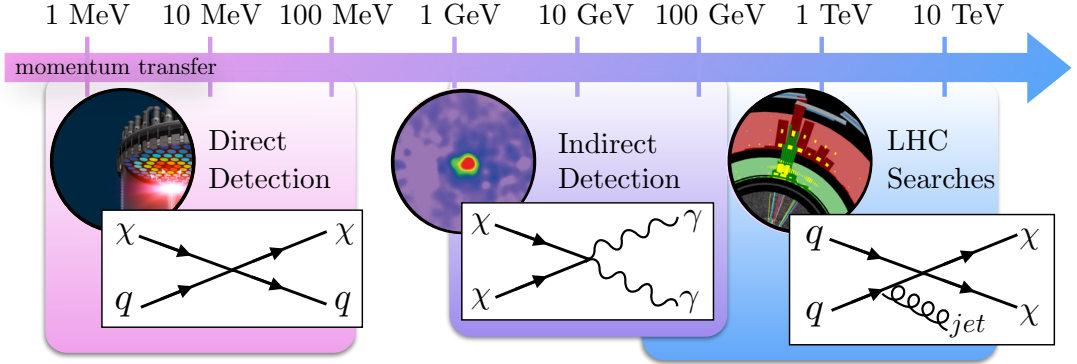


Figure 1: Range of momenta probed in Direct Detection experiments, Indirect Detection experiments and LHC searches for weak scale Dark Matter candidates.

2.1 Evolution of theories for Dark Matter searches at colliders

For two of the three Dark Matter search strategies -direct and indirect detection- experimental results are presented in terms of effective field theories (EFTs). The operators in these EFTs are build from SM fermions and Dark Matter fields,

$$\mathcal{L}_{\text{EFT}} = \sum_{f=u,d,\ell} \left(\frac{C_1^f}{\Lambda^2} \bar{f} f \bar{\chi} \chi + \frac{C_2^f}{\Lambda^2} \bar{f} f \bar{\chi} \gamma^5 \chi + \frac{C_3^f}{\Lambda^2} \bar{f} \gamma^5 f \bar{\chi} \chi + \frac{C_4^f}{\Lambda^2} \bar{f} \gamma^5 f \bar{\chi} \gamma^5 \chi + \dots \right), \quad (2.1)$$

where χ denotes a Dirac fermion DM candidate and the sum over $f = u, d, \ell$ extends over SM quarks and leptons. The EFT is fully described by the parameters

$$\{m_\chi, \Lambda, C_i^f\}, \quad (2.2)$$

where m_χ is the mass of the DM candidate. This ansatz is justified for the small momentum transfer $q^2 \ll \Lambda^2$ in DM-nucleon scattering (set by the non-relativistic velocities of DM in the halo) and in DM annihilation (set by the mass of the annihilating DM candidate), illustrated in Fig. 1. Early papers on DM searches at colliders refer to these EFTs to quantify the reach of the LHC in the parameter space defined by (2.2) [? ? ?]. The momentum transfer accessible at the LHC is larger than the suppression scale $\Lambda \ll q_{\text{LHC}}^2$ for many theories of DM. In this case, the mediator of the interaction between the dark sector and the SM can be resonantly produced and predictions derived from the EFT framework are bound to fail []. The kinematics of on-shell propagators can be captured in simplified models, which aim to represent a large number of extensions of the SM, while keeping only the degrees of freedom relevant for LHC phenomenology. In the case of a pseudoscalar mediator the corresponding interactions between DM, SM fermions and the mediator a read

$$\mathcal{L}_{\text{simp}} = -i g_\chi a \bar{\chi} \gamma_5 \chi - i a \sum_i \left(g_u y_i^u \bar{u}_i \gamma_5 u_i + g_d y_i^d \bar{d}_i \gamma_5 d_i + g_\ell y_i^\ell \bar{\ell}_i \gamma_5 \ell_i \right), \quad (2.3)$$

in which i is a flavour index. In addition, there is the scalar potential including a potential Higgs portal

$$V(H, a) = \frac{1}{2} m_a^2 a^2 + b_a a H^\dagger H + \lambda_{H a} a^2 H^\dagger H + \lambda a^4. \quad (2.4)$$

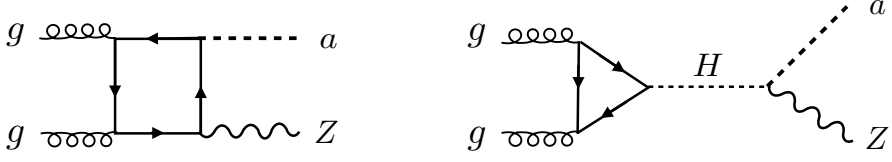


Figure 2: Feynman diagrams contributing to $\sigma(pp \rightarrow aZ)$ in the simplified model with a pseudoscalar singlet mediator a (left) and in the 2HDM+ a model (right).

The Higgs portal is generally considered irrelevant, otherwise there are constraints from Higgs coupling strength measurements and of the Higgs CP property stronger than all limits from searches for DM at the LHC []. The quartic couplings in (2.4) are not relevant for collider searches for DM. This simplified model is therefore fully described by the parameters

$$\{m_\chi, m_a, g_\chi, g_u, g_d, g_\ell\}, \quad (2.5)$$

and matches to the EFT (2.1) with $C_4^f/\Lambda^2 = g_\chi g_f y_f/m_a^2$ and $C_i^f = 0$ for all other Wilson coefficients, but retains the full momentum dependence of the pseudoscalar propagator. The operators in both \mathcal{L}_{EFT} and $\mathcal{L}_{\text{simp}}$ violate gauge invariance, because of the chiral SM fermions. In the case of the EFT this suggests the scaling of the Wilson coefficients $C_i^f = c_i^f m_{f_i}/\Lambda$ [], whereas for the simplified model restoring gauge invariance requires the embedding of the mediator a into an electroweak multiplet. The absence of gauge invariance leads to unitarity violating amplitudes. For example on the left of Fig. 2, we show the diagram contributing to the amplitude for the production of the pseudoscalar mediator in association with a Z -boson, which diverges with the center-of-mass energy $\mathcal{M}(pp \rightarrow Za) \propto \log^2(s)$ in the simplified model, signaling the omission of additional diagrams. Since this divergence is only logarithmic, the simplified model does not break down for the energies accessible at the LHC []. More importantly, the additional degrees of freedom necessary to unitarize the amplitudes cannot be arbitrarily heavy and change the phenomenology of the simplified model significantly. For example, the $pp \rightarrow Za$ cross section can be made finite by the exchange an additional scalar H with a coupling to a and Z , and the corresponding diagram is shown on the right of Fig. 2. Since resonant production is strongly enhanced compared to initial state radiation, the hierarchy of initial state mono-X signals, mono-jet > mono-photon > mono- Z > mono-Higgs, can be turned upside-down with different kinematics requiring adapted experimental search strategies. The embedding of the pseudoscalar mediator model (2.3) is not unique. Both the mediator and the DM can be embedded in different electroweak multiplets, resulting in additional model-dependent and model-independent signals []. In this whitepaper, we consider the simplest embedding with a single SM-singlet DM candidate, which captures the maximal number of interesting signatures.

2.2 Scalar Model Description

We shall consider a Dirac DM candidate, χ , and expand the scalar sector of the SM to include two Higgs doublets, Φ_1 and Φ_2 , in addition to a real singlet scalar field, S . Following

the discussion in [?], we outline the scalar potential which controls the mixing between the CP even scalars, and the Yukawa structure which dictates the coupling of those scalars to the DM and SM fermions.

It is convenient to rotate $\{\Phi_1, \Phi_2\}$ to the Higgs basis $\{\Phi_h, \Phi_H\}$, which is defined such that only one of the two doublets obtains a vev. Taking $\langle\Phi_H\rangle = 0$ and $\langle\Phi_h\rangle = v \sim 246$ GeV, the two Higgs doublets are then defined by

$$\Phi_h = \cos\beta\Phi_1 + \sin\beta\Phi_2 = \begin{pmatrix} G^+ \\ \frac{v+h+iG^0}{\sqrt{2}} \end{pmatrix}, \quad (2.6)$$

$$\Phi_H = -\sin\beta\Phi_1 + \cos\beta\Phi_2 = \begin{pmatrix} H^+ \\ \frac{H+iA}{\sqrt{2}} \end{pmatrix}. \quad (2.7)$$

The scalar potential consists of the usual 2HDM potential, augmented by terms involving the new singlet scalar S . We will assume that the scalar potential has a spontaneously broken \mathbb{Z}_2 symmetry for the particle S . This may arise naturally, for example, in the case where S is part of a complex scalar charged under a dark $U(1)$ gauge group. The scalar potential is thus given by

$$\hat{V}(\Phi_h, \Phi_H, S) = \hat{V}_{2\text{HDM}}(\Phi_h, \Phi_H) + \hat{V}_S(S) + \hat{V}_{S2\text{HDM}}(\Phi_h, \Phi_H, S), \quad (2.8)$$

where

$$\begin{aligned} \hat{V}_{2\text{HDM}}(\Phi_h, \Phi_H) &= \hat{M}_{hh}^2 \Phi_h^\dagger \Phi_h + \hat{M}_{HH}^2 \Phi_H^\dagger \Phi_H + (\hat{M}_{hH}^2 \Phi_H^\dagger \Phi_h + h.c.) + \frac{\hat{\lambda}_h}{2} (\Phi_h^\dagger \Phi_h)^2 + \frac{\hat{\lambda}_H}{2} (\Phi_H^\dagger \Phi_H)^2 \\ &\quad + \hat{\lambda}_3 (\Phi_h^\dagger \Phi_h)(\Phi_H^\dagger \Phi_H) + \hat{\lambda}_4 (\Phi_H^\dagger \Phi_h)(\Phi_h^\dagger \Phi_H) + \frac{\hat{\lambda}_5}{2} ((\Phi_H^\dagger \Phi_h)^2 + h.c.), \end{aligned} \quad (2.9)$$

$$\hat{V}_S(S) = \frac{1}{2} \hat{M}_{SS}^2 S^2 + \frac{1}{4} \hat{\lambda}_S S^4, \quad (2.10)$$

$$\hat{V}_{S2\text{HDM}}(\Phi_h, \Phi_H, S) = \frac{\hat{\lambda}_{HHS}}{2} (\Phi_H^\dagger \Phi_H) S^2 + \frac{\hat{\lambda}_{hhs}}{2} \Phi_h^\dagger \Phi_h S^2 + \frac{1}{2} (\hat{\lambda}_{hHS} \Phi_H^\dagger \Phi_h S^2 + h.c.). \quad (2.11)$$

In general, there would be mass mixing between all three neutral CP even scalars of the model, h , H , and S . We shall, however, impose a generalized Higgs “alignment limit” which decouples the SM Higgs, h , from the other two states. This is desirable because it reduces the scalar mixing to a 2-state problem and guarantees that h couples like the SM Higgs. We thus set

$$\hat{\lambda}_h = \hat{\lambda}_H = \hat{\lambda}_3 + \hat{\lambda}_4 + \hat{\lambda}_5, \quad (2.12)$$

$$\hat{\lambda}_{hhs} = 0, \quad (2.13)$$

where the first of these conditions is sufficient to impose alignment in a standard 2HDM, and the second clearly prevents h - S mixing (refer to [?] for further discussion of the alignment limit). The remaining H - S mass matrix is then diagonalized to obtain two mass eigenstate scalars, S_1 and S_2 , such that

$$H = \cos\theta S_1 - \sin\theta S_2, \quad (2.14)$$

Model	ϵ_d	ϵ_u	ϵ_l
Type I	$\cot \beta$	$\cot \beta$	$\cot \beta$
Type II	$-\tan \beta$	$\cot \beta$	$-\tan \beta$
Type X	$\cot \beta$	$\cot \beta$	$-\tan \beta$
Type Y	$-\tan \beta$	$\cot \beta$	$\cot \beta$
Inert	0	0	0

Table 1: Values of the Yukawa scaling factors, $\epsilon_{u,d,l}$ which correspond to models with discrete \mathcal{Z}_2 symmetries.

$$S = v_S + \sin \theta S_1 + \cos \theta S_2, \quad (2.15)$$

where

$$\sin 2\theta = \frac{2\hat{\lambda}_{hHs}vv_S}{M_{S_1}^2 - M_{S_2}^2}. \quad (2.16)$$

The scalar mass spectrum then simplifies to

$$M_A^2 = M_{H^+}^2 + (\hat{\lambda}_4 - \hat{\lambda}_5) \frac{v^2}{2}, \quad (2.17)$$

$$M_{S_{1,2}}^2 = \frac{1}{2} \left(M_A^2 + \hat{\lambda}_5 v^2 \right) \left(1 \pm \frac{1}{\cos 2\theta} \right) + \hat{\lambda}_S v_S^2 \left(1 \mp \frac{1}{\cos 2\theta} \right). \quad (2.18)$$

Taking h to be the observed SM Higgs boson then fixes $\hat{\lambda}_h$ and hence also fixes $\hat{\lambda}_H$ via the alignment condition (2.12). Using the previous equations, we can rewrite M_A and M_{H^+} as a function of $M_{S_{1,2}}$, θ , and $\hat{\lambda}_{4,5}$:

$$M_{H^+}^2 = M_{S_1}^2 \cos^2 \theta + M_{S_2}^2 \sin^2 \theta - (\hat{\lambda}_4 + \hat{\lambda}_5) \frac{v^2}{2}, \quad (2.19)$$

$$M_A^2 = M_{S_1}^2 \cos^2 \theta + M_{S_2}^2 \sin^2 \theta - \hat{\lambda}_5 v^2. \quad (2.20)$$

The only portal between the DM and other fields is via its Yukawa coupling to the singlet scalar,

$$\mathcal{L}_{\text{DM}} = -y_\chi S \bar{\chi} \chi. \quad (2.21)$$

We will assume that the DM particle has no bare mass term, and that its mass is instead generated by the vacuum expectation value of the singlet scalar, i.e. $m_\chi = y_\chi v_s$ with $\langle S \rangle = v_s$. Although this is not strictly necessary, such a scenario arises naturally if DM is a chiral fermion charged under some dark gauge group that is broken spontaneously by the vev of S . This assumption adds a constraint between the DM mass and the DM Yukawa coupling, removing the freedom to accommodate the relic density by varying these two parameters independently.

We will express the Yukawa interactions of the SM fermions with the Higgs doublets as

$$L_{\text{Yukawa}} = - \sum_{n=h,H} \left(Y_{n,ij}^U \bar{Q}_L^i u_R^j \tilde{\Phi}_n + Y_{n,ij}^D \bar{Q}_L^i d_R^j \Phi_n + Y_{n,ij}^L \bar{L}_L^i l_R^j \Phi_n + h.c. \right), \quad (2.22)$$

and we will assume that the Yukawa matrices of the additional doublet are proportional to the SM ones:

$$Y_h^i \equiv Y_{\text{SM}}^i, \quad (2.23)$$

$$Y_H^i = \epsilon_i Y_{\text{SM}}^i, \quad (2.24)$$

where the ϵ_i are Yukawa scaling factors, with $i = u, d, l$. This Yukawa structure is the so-called Aligned Yukawa model [? ? ? ? ?], which satisfies Natural Flavour Conservation. In special cases where the ϵ_i satisfy certain relationships, the Aligned Yukawa structure can correspond to one of the Z_2 symmetric Yukawa structures (Type I, II, X or Y), as shown in Table 2. While we will determine constraints for both Type I and Type II Yukawa structures, we will also include results for more general choices of the scaling factors that satisfy the Aligned Yukawa criteria. See [?] for a more detailed discussion of the Yukawa structure in these models.

3 Model parameters

Description of the model Two Higgs doublet models provide natural, consistent embeddings of scalar and pseudoscalar mediators to a dark sector. Besides the SM scalar h , it predicts a neutral scalar H , a charged scalar H^\pm , and a pseudoscalar spin-0 state A . Several shortcomings and unmotivated assumptions in the simplified model are remedied in this framework. Couplings between SM fermions and the physical (pseudo)scalar are renormalizable. The custodial symmetry of the SM electroweak sector is protected at tree-level and therefore contributions to electroweak precision observables are loop-suppressed. Flavour- and CP-changing neutral currents are protected at tree-level if a discrete symmetry is imposed on the two scalar doublets H_1 and H_2 , under which $H_1 \rightarrow H_1$ and $H_2 \rightarrow -H_2$. This Z_2 symmetry is the minimal condition necessary to guarantee the absence of FCNCs at tree-level [? ?] and such a symmetry is realized in many well-motivated complete ultraviolet theories in the form of supersymmetry, a $U(1)$ symmetry or a discrete symmetry acting on the Higgs doublets. The Yukawa structure of 2HDMs differentiate between the different types,

$$\mathcal{L}_Y = - \sum_{i=1,2} \left(\bar{Q} Y_u^i \tilde{H}_i u_R + \bar{Q} Y_d^i H_i d_R + \bar{L} Y_\ell^i H_i \ell_R + \text{h.c.} \right), \quad (3.1)$$

and we collect the different models in Table 2 below. The signatures discussed in this paper are largely independent of the type of 2HDM, but different signatures are more or less prominent depending on the Yukawa structure. Minimal flavour violating Yukawa structures with an explicitly broken Z_2 symmetry allow for additional decay channels and collider signatures. In general, the presence of vacuum expectation values $\langle H_i \rangle = (0, v_i/\sqrt{2})^T$, breaks the Z_2 symmetry. If the vacuum respects the Z_2 symmetry, *i.e.* one of the vevs vanishes, the corresponding Higgs doublet is *inert*. The lightest component of this doublet is stable and provides a natural DM candidate []. The inert 2HDM is a elegant, consistent model of scalar DM as a component of an $SU(2)_L$ doublet. For more general DM candidates, the coupling of the physical (pseudo)scalar to DM requires additional assumptions.

For a SM singlet, Dirac fermion χ , the operators $\bar{\chi}\chi$ and $\bar{\chi}\gamma_5\chi$ are singlets and renormalizable couplings to H_1 or H_2 are not possible. For the physical (pseudo)scalar to be a mediator to a dark sector, either additional $SU(2)_L$ doublet fermions or $SU(2)_L$ singlet scalars are necessary. If these degrees of freedom are decoupled from the spectrum, one can consider dimension five couplings to DM

$$\mathcal{L} = \frac{H_1^\dagger H_2}{\Lambda} \bar{\chi}\chi + \frac{H_1^\dagger H_2}{\Lambda} \bar{\chi}\gamma_5\chi + h.c., \quad (3.2)$$

in which $\Lambda \gg v$ denotes the mass scale of these additional states. This framework captures the universal properties of such a (pseudo)scalar mediator [6]. If the additional states are light, $\Lambda \lesssim v$, additional signatures allow to distinguish the mediator structure. We focus on a class of models with an additional, real singlet, which either transforms as a scalar S or pseudoscalar P with DM couplings

$$\mathcal{L}_{P\chi} = -iy_\chi P\bar{\chi}\gamma_5\chi, \quad (3.3)$$

$$\mathcal{L}_{S\chi} = -y_\chi S\bar{\chi}\chi, \quad (3.4)$$

It is straightforward to embed the real scalar S and pseudoscalar P a complex field $\phi = S + iP$, and a potential vev of S can contribute to the DM mass [6].

Pseudoscalar Mediator In order to identify the CP eigenstates with the mass eigenstates, two scalars h and H , two pseudoscalars a and A , and a charged scalar H^\pm , we choose all parameters of the scalar potential real. The most general scalar potential can be written as

$$V(P, H) = V_H + V_{PH} + V_P, \quad (3.5)$$

with the potential for the two Higgs doublets

$$\begin{aligned} V_H = & \mu_1 H_1^\dagger H_1 + \mu_2 H_2^\dagger H_2 + (\mu_3 H_1^\dagger H_2 + h.c.) + \lambda_1 (H_1^\dagger H_1)^2 + \lambda_2 (H_2^\dagger H_2)^2 \\ & + \lambda_3 (H_1^\dagger H_1)(H_2^\dagger H_2) + \lambda_4 (H_1^\dagger H_2)(H_2^\dagger H_1) + [\lambda_5 (H_1^\dagger H_2)^2 + h.c.], \end{aligned} \quad (3.6)$$

potential terms which connect doublets and singlets

$$V_{HP} = P (ib_P H_1^\dagger H_2 + h.c.) + P^2 (\lambda_{P1} H_1^\dagger H_1 + \lambda_{P2} H_2^\dagger H_2), \quad (3.7)$$

Model	up-type	down-type	leptons
Type I	H_2	H_2	H_2
Type II	H_2	H_1	H_1
Type III (X)	H_2	H_2	H_1
Type IV (Y)	H_2	H_1	H_2

Table 2: Categorization of the different Yukawa sectors for models with discrete Z_2 symmetries. The two Higgs doublet models of Type III and IV are also called Type X and Y or *lepton-specific* and *flipped* in the literature.

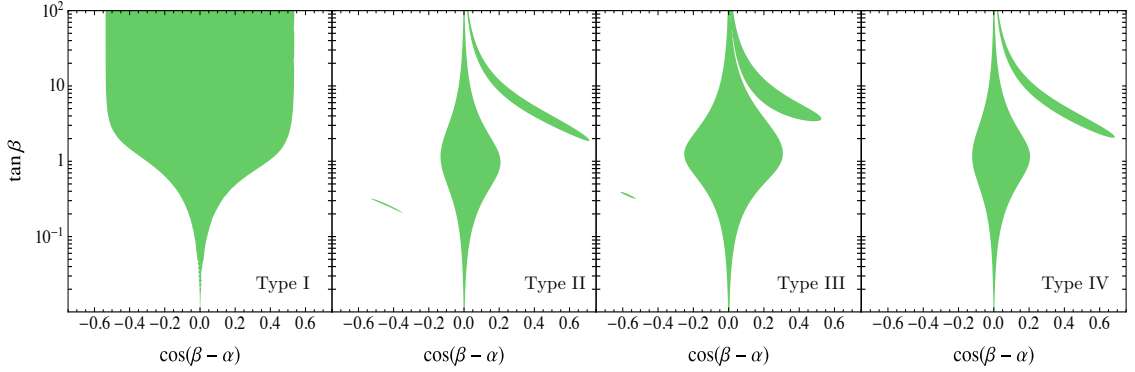


Figure 3: Parameter space allowed by a global fit to Higgs coupling strength measurements for (from left to right) a Yukawa sector of type I ($Y_u^1 = Y_d^1 = Y_\ell^1 = 0$), type II ($Y_u^1 = Y_d^2 = Y_\ell^2 = 0$), type III ($Y_u^1 = Y_d^1 = Y_\ell^2 = 0$), and type IV ($Y_u^1 = Y_d^2 = Y_\ell^1 = 0$).

and the singlet potential

$$V_P = \frac{1}{2} m_P^2 P^2 + \lambda_P P^4. \quad (3.8)$$

Upon rotation to the mass eigenbasis, we trade the five dimensionful and eight dimensionless parameters in the potential for physical masses and mixing angles and three quartic couplings

$$\left\{ \begin{array}{l} \mu_1, \mu_2, \\ \mu_3, m_P^2, b_P \\ \lambda_1, \lambda_2, \lambda_3, \lambda_4, \lambda_5 \\ \lambda_{P1}, \lambda_{P2}, \lambda_P \end{array} \right\} \longleftrightarrow \left\{ \begin{array}{l} v, M_h, \cos(\beta - \alpha) \\ M_a, M_A, M_H, M_{H^\pm} \\ t_\beta, \cos(\theta), \\ \lambda_3, \lambda_{P1}, \lambda_{P2}, \lambda_P \end{array} \right\}. \quad (3.9)$$

Out of these parameters, the electroweak scale $v = 246$ GeV and the mass of the SM-like CP-even mass eigenstate $M_h = 125$ GeV are fixed. The mixing angle α between the CP-even scalars h and H is constrained by Higgs coupling strength measurements [] and we show the allowed parameter space in the $\cos(\beta - \alpha)$ plane in Fig. 3 for the Yukawa sector of a 2HDM of type II. For arbitrary values of $t_\beta = v_2/v_1$ only the limit $\cos(\beta - \alpha) \approx 0$ is allowed, for which the couplings of the CP-even state h align with the couplings of the SM Higgs boson. For the analyses discussed in the remainder of this paper, we choose this so-called alignment limit and treat t_β as a free parameter. Electroweak precision measurements constrain the splitting between the masses M_H, M_A, M_a and M_{H^\pm} , since loops of spin-0 states modify the propagators of the electroweak gauge bosons at one-loop. For $M_H = M_{H^\pm}$ and $\cos(\beta - \alpha) = 0$, these corrections vanish due to a custodial symmetry in the tree-level potential V_H [] and the masses of the CP-odd mass eigenstates can be treated as free parameters. This custodial symmetry is also present in V_H if $M_A = M_{H^\pm}$ and $\cos(\beta - \alpha) = 0$, but the presence of the pseudoscalar mixing term in V_P softly breaks this symmetry. As a consequence, the pseudoscalar mixing angle θ and the mass splitting between M_H, M_A and M_a are constrained in this situation. In Fig. 4, we show these constraints as maximally allowed $\sin \theta$ contours in the (M_a, M_H) plane. Flavour observables

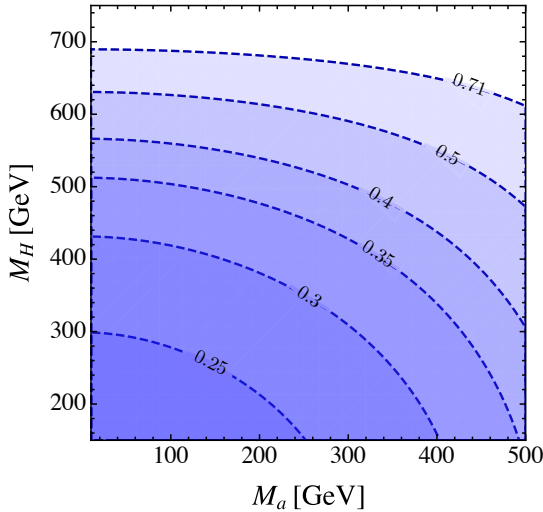


Figure 4: Values of M_H and M_a allowed by electroweak precision constraints for $\cos(\beta - \alpha) = 0$, $M_{H^\pm} = M_A = 750$ GeV, and varying values of the pseudoscalar mixing angle $\sin \theta = 0.25, 0.3, 0.35, 0.4, 0.5$, and maximal mixing angle $\sin \theta = 1/\sqrt{2} \approx 0.71$. The parameter space below and to the left of the dashed contours is excluded. The same plot can be produced for the scalar mediator model for $\cos(\beta - \alpha) = 0$, $M_{H^\pm} = M_H = 750$ GeV by exchanging $M_a \rightarrow M_{S_1}$ and $M_H \rightarrow M_A$.

are mostly sensitive to corrections from one-loop exchanges of the charged scalar H^\pm , whose contributions to $b \rightarrow X_s \gamma$ [? ? ?] and $B_s - \bar{B}_s$ mixing [? ? ? ?] lead to the strongest indirect constraints on M_{H^\pm} . Since the couplings of the charged scalar only depend on t_β , these constraints result in the bound $\tan \beta \gtrsim 0.8$ for $M_{H^\pm} = 750$ GeV, independent of the choice of the Yukawa sector.

In addition to these constraints, the potential V_H needs to give rise to a stable vacuum breaking the electroweak symmetry, whereas the parameters in V_P need not introduce a vacuum expectation value for P , and scattering amplitudes should remain perturbative [? ?] and unitary [? ? ? ?] up to the UV scale, where the 2HDM+a is UV completed. These conditions impose additional constraints on the quartic couplings in the potential, which are satisfied for $M_H, M_A, M_a \lesssim \mathcal{O}(1)$ TeV and $\lambda_3, \lambda_{P1}, \lambda_{P2}$ and λ_P of $\mathcal{O}(1)$ as long as t_β is not too much smaller than one. For the case of fixed¹ $\lambda_3, \lambda_{P1}, \lambda_{P2}$, the stability condition therefore leads to additional constraints on the mixing angle θ and the masses. The parameter space of the 2HDM+a is strongly constrained, as summarized below.

¹The singlet quartic λ_P is entirely irrelevant for the phenomenology of the 2HDM+a.

$$\begin{aligned}
v, M_h, \cos(\beta - \alpha) &\longleftrightarrow \text{fixed by Higgs measurements,} \\
M_{H^\pm}, &\longleftrightarrow \text{constrained by flavour observables,} \\
\sin(\theta), M_H \text{ or } M_A &\longleftrightarrow \text{constrained by EWPM,} \\
\lambda_3, \lambda_{P1}, \lambda_{P2}, \lambda_P &\longleftrightarrow \text{constrained by stability, perturbativity and unitarity constraints.}
\end{aligned}$$

This leaves us with effectively three free parameters from the potential, the Dark Matter mass and the coupling of the mediator to the DM candidate

$$\{m_\chi, M_a, t_\beta, M_H \text{ or } M_A, y_\chi\}. \quad (3.10)$$

Scalar Mediator For a scalar mediator, the most general potential

$$V(S, H) = V_H + V_{SH} + V_S \quad (3.11)$$

can be conveniently given in the Higgs basis, which is defined by

$$\begin{pmatrix} \Phi_h \\ \Phi_H \end{pmatrix} = \begin{pmatrix} \cos \beta & \sin \beta \\ -\sin \beta & \cos \beta \end{pmatrix} \begin{pmatrix} H_1 \\ H_2 \end{pmatrix}, \quad (3.12)$$

such that $\langle \Phi_H \rangle = 0$ and $\langle \Phi_h \rangle = v$. In this basis, the potential in (3.6) is given by (we denote couplings and potentials in the Higgs basis by a hat)

$$\begin{aligned}
\hat{V}_H &= \hat{M}_{hh}^2 \Phi_h^\dagger \Phi_h + \hat{M}_{HH}^2 \Phi_H^\dagger \Phi_H + (\hat{M}_{hH}^2 \Phi_H^\dagger \Phi_h + h.c.) + \frac{\hat{\lambda}_h}{2} (\Phi_h^\dagger \Phi_h)^2 + \frac{\hat{\lambda}_H}{2} (\Phi_H^\dagger \Phi_H)^2 \\
&+ \hat{\lambda}_3 (\Phi_h^\dagger \Phi_h) (\Phi_H^\dagger \Phi_H) + \hat{\lambda}_4 (\Phi_H^\dagger \Phi_h) (\Phi_h^\dagger \Phi_H) + \frac{\hat{\lambda}_5}{2} ((\Phi_H^\dagger \Phi_H)^2 + h.c.), \quad (3.13)
\end{aligned}$$

the part which allows for mixing between the scalar singlets and doublets reads

$$\hat{V}_{SH} = S^2 \left(\frac{\hat{\lambda}_{hhs}}{2} \Phi_h^\dagger \Phi_h + \frac{\hat{\lambda}_{HHS}}{2} (\Phi_H^\dagger \Phi_H) + \frac{1}{2} (\hat{\lambda}_{hHS} \Phi_H^\dagger \Phi_h + h.c.) \right), \quad (3.14)$$

and the scalar singlet self-interaction is given by

$$\hat{V}_S = \frac{1}{2} \hat{M}_{SS}^2 S^2 + \frac{1}{4} \hat{\lambda}_S S^4. \quad (3.15)$$

There are again 13 parameters, which can be exchanged for physical masses and mixing angles as well as a number of additional dimensionless parameters

$$\left\{ \begin{array}{l} \hat{M}_{hh}^2, \hat{M}_{HH}^2, \\ \hat{M}_{hM}^2, \hat{M}_{SS}^2, \\ \hat{\lambda}_h, \hat{\lambda}_H, \hat{\lambda}_3, \hat{\lambda}_4, \hat{\lambda}_5 \\ \hat{\lambda}_{hhs}, \hat{\lambda}_{HHS}, \hat{\lambda}_{hHS}, \hat{\lambda}_S \end{array} \right\} \longleftrightarrow \left\{ \begin{array}{l} v, M_h, \cos(\beta - \alpha) \\ M_{S_1}, M_A, M_{S_2}, M_{H^\pm} \\ t_\beta, \cos(\theta), \\ \hat{\lambda}_4, \hat{\lambda}_5, \hat{\lambda}_S, \hat{\lambda}_{HHS} \end{array} \right\}, \quad (3.16)$$

in which the additional neutral scalar state S_1 and S_2 are superpositions of S and H . Analogous to the case of a pseudoscalar mediator, several constraints reduce this number of parameters. Measurements of the 125 GeV Higgs mass and its couplings determine v, M_h as well as $\cos(\beta - \alpha) \approx 0$ and $\hat{\lambda}_{hHS} \approx 0$. The latter condition leads to suppressed $h-S$ -mixing. Constraints from electroweak precision measurements are very weak for $M_{H^\pm} = M_A$, in which the custodial symmetry is preserved, but relevant for $M_{H^\pm} = M_{S_2}$ and varying M_{S_1} . The calculation is exactly analogous to the pseudoscalar case for $M_H \leftrightarrow M_A$ and $M_a \leftrightarrow M_{S_1}$, and leads to the constraints shown in Fig. ?? for these replacements. Vacuum stability and perturbativity conditions constrain the quartic couplings and flavour observables are independent of the mediator structure and only depend on M_{H^\pm} . We summarize as before

$$\begin{aligned}
v, M_h, \cos(\beta - \alpha), \hat{\lambda}_{hhS} &\longleftrightarrow \text{fixed by Higgs measurements,} \\
M_{H^\pm}, &\longleftrightarrow \text{constrained by flavour observables,} \\
\sin(\theta), M_{S_2} \text{ or } M_A &\longleftrightarrow \text{constrained by EWPM,} \\
\hat{\lambda}_4, \hat{\lambda}_5, \hat{\lambda}_S, \hat{\lambda}_{HHS} &\longleftrightarrow \text{constrained by stability, perturbativity and unitarity constraints,}
\end{aligned}$$

which apart from the fermion couplings leaves the effective parameters

$$\{m_\chi, M_{S_1}, t_\beta, M_{S_2} \text{ or } M_A, y_\chi\}. \quad (3.17)$$

The effect of the quartic self-couplings The conditions under which the tree-level potential (3.5) remains bounded from below are $\lambda_{P_1}, \lambda_{P_2} > 0$ and [?]:

$$\lambda_1 > 0, \lambda_2 > 0, \lambda_3 > -\sqrt{\lambda_1 \lambda_2}, \lambda_3 + \lambda_4 - |\lambda_5| > -\sqrt{\lambda_1 \lambda_2} \quad (3.18)$$

which can be inferred from analyzing the scalar potential at large field values $H_1, H_2 \gg v$. For $M_{H^\pm} = M_{H_0}$, the first two conditions in (3.18) may be simply written as

$$\frac{m_h^2}{v^2}(1 - t_\beta^2) + \lambda_3 t_\beta^2 > 0, \quad \frac{m_h^2}{v^2}(1 - t_\beta^{-2}) + \lambda_3 t_\beta^{-2} > 0, \quad (3.19)$$

which result in the requirement $\lambda_3 > m_h^2/v^2 = 0.258$. In Fig. 5 we show the regions of parameter space in the (M_a, M_H) (left) and (s_θ, M_a) (right) planes for which the tree-level boundedness from below conditions (3.18) are satisfied, assuming $M_{H^\pm} = M_H = M_A$. For increasing λ_3 , the parameter space for which these conditions can be satisfied becomes larger. Importantly, the coupling of the 125 GeV Higgs to the two pseudoscalar degrees of freedom

$$\begin{aligned}
g_{aAh} &= \frac{c_\theta s_\theta}{M_H v} [M_h^2 + M_H^2 - M_a^2 - 2(\lambda_3 - \lambda_{P1} c_\beta^2 - \lambda_{P2} s_\beta^2)v^2] \\
&\xrightarrow{\lambda_3 \approx \lambda_{P1} \approx \lambda_{P2}} \frac{c_\theta s_\theta}{m_H v} [m_h^2 + m_H^2 - m_a^2]
\end{aligned} \quad (3.20)$$

is reduced in this region, unless $\lambda_3 \approx \lambda_{P1} \approx \lambda_{P2}$. Therefore, in the benchmarks for the

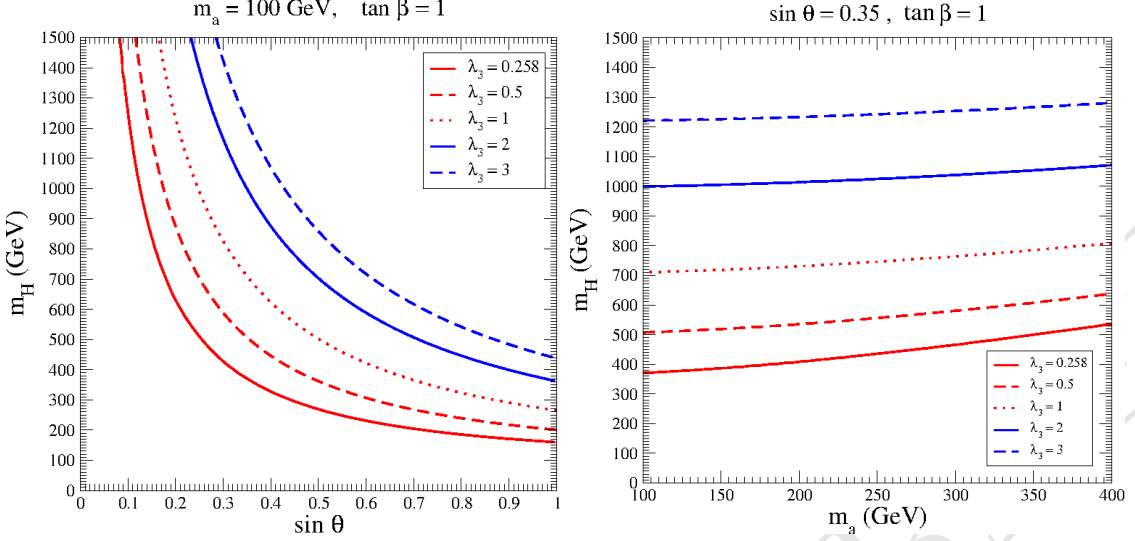


Figure 5: Regions of parameter space in the (M_a, M_H) (left) and $(\sin \theta, M_a)$ (right) planes for which the tree-level boundedness from below conditions (3.18) are satisfied, assuming $M_{H^\pm} = M_H = M_A$.

mono-Higgs signal $\sigma(pp \rightarrow A \rightarrow ah \rightarrow h + E_T^{\text{miss}})$, we consider this limit. The coupling of the heavy neutral scalar H to two pseudoscalar degrees of freedom in turn is independent of λ_{P1} and λ_{P2} for $\lambda_{P1} \approx \lambda_{P2}$,

$$g_{Haa} = \frac{1}{m_H v} \left[2 t_{2\beta}^{-1} s_\theta^2 (m_h^2 - \lambda_3 v^2) + s_{2\beta} c_\theta^2 v^2 (\lambda_{P1} - \lambda_{P2}) \right] \xrightarrow{\lambda_{P1} \approx \lambda_{P2}} \frac{1}{m_H v} \left[2 t_{2\beta}^{-1} s_\theta^2 (m_h^2 - \lambda_3 v^2) \right]. \quad (3.21)$$

In this limit, the partial decay width $\Gamma(H \rightarrow aa)$ is enhanced for sizable λ_3 , and the branching ratio $\text{Br}(H \rightarrow aZ)$ is reduced. Searches for mono-Z final states $\sigma(pp \rightarrow H \rightarrow aZ \rightarrow Z + E_T^{\text{miss}})$ are therefore most sensitive if λ_{P1} and λ_{P2} are small or sufficiently split.

4 Parameter grid

4.1 Parameter scans on masses, couplings and mixing angles

Logic of how we proceeded

- Starting from benchmark 3 of [?]
- Mapping the kinematics and sensitivity of the model by scanning some of the various parameters
- Checking whether other existing models can be rescaled

4.1.1 Results of studies

Each of the signatures should have the following plots in the planes of the final recommendation:

- efficiency at parton level with simplified, published cuts
- total and fiducial cross-section at parton level
- 2 - 3 kinematic plots of what has been scanned that are most representative for the analysis (here the analysers decide, then we harmonize at the end)

Signatures:

- Mono-Z (lep/had)
- MonoH \rightarrow bb
- Monojet
- ttbar+MET, with specific discussion about rescaling
- other signatures who have not yet presented at public meetings, in ATLAS and CMS

4.1.2 Studies of the $h(bb) + E_T^{\text{miss}}$ signature

The studies of the $h(bb) + E_T^{\text{miss}}$ channel presented here are based on MC simulations with version 2.4.3 of MADGRAPH 5 [?] using a Universal FeynRules Output [?] implementation of the 2HDM with a Yukawa sector of type II with DM mediator (2HDM+a), as provided by the authors of [?]. The NNPDF30_lo_as_0130 set of parton distribution functions (PDF) at leading order in the five-flavor scheme, which assumes a massless b -quark, with $\alpha_S(m_Z) = 0.130$ is used for these simulations [?]. For consistency, five-flavor scheme and $m_b = 0$ GeV are chosen for the matrix element (ME) computation in MADGRAPH 5.

The ME generated for the parton-level studies presented in the following is $gg \rightarrow h\chi\chi$ represented in ?? The only exception is the $M_a - \tan\beta$ scan which will be discussed in the following and is summarised in Figure 16. In this scan also the ME $bb \rightarrow h\chi\chi$ is generated because at high $\tan\beta$, the bb initiated process can have an amplitude of a similar magnitude as the gluon fusion initiated process from ?? [?]. The gluon fusion is dominant in all the remaining parameter space, therefore the bb initiated process and other negligible contributions are not considered explicitly for all the scans.

Signal kinematics The free parameters of the 2HDM+a model fall into two categories:

- those which only affect total signal cross section;
- those which, in addition to the total cross section, also affect the kinematics, primarily the E_T^{miss} distribution.

In the following, the free parameters of the 2HDM+a model are studied in the context of the $h(bb) + E_T^{\text{miss}}$ signature with a particular focus on the latter category of parameters, as it emphasizes the kinematic diversity of potential new physics contributions represented in this simplified model.

The masses M_A and M_a of the pseudoscalars A and a , which represent the two mediators in ??, affect the kinematics of the $h(bb) + E_T^{\text{miss}}$ in a profound way by changing the location of the Jacobian peak in the E_T^{miss} distribution. This effect is crucial to searches for $h(bb) + E_T^{\text{miss}}$ such as [?], since the E_T^{miss} observable can be used to reduce many SM backgrounds, which are typically characterised by low E_T^{miss} , unlike DM signal processes with potentially very high E_T^{miss} . In other words, the distribution of E_T^{miss} determines the sensitivity of the search.

The Jacobian peak is the result of a resonantly produced pseudoscalar A decaying in the $2 \rightarrow 1 \rightarrow 2$ process $gg \rightarrow A \rightarrow ah$, where the Higgs boson proceeds to decay into a visible final state as $h \rightarrow bb$, and the light pseudoscalar into an invisible one as $a \rightarrow \chi\chi$. Thus, the resonant $A \rightarrow ah$ process has a sharply peaked resonance in the invariant mass distribution of the final state system with a width determined by the widths of a , A , and h . This results in a peak in the momentum distribution of the DM system and in its transverse component that is reconstructed as E_T^{miss} in the detector.

Since it is determined by the masses of the particles involved in the decay, the location of the Jacobian peak can be calculated analytically [?]:

$$E_T^{\text{miss},\text{max}} \approx \frac{\sqrt{(M_A^2 - M_a^2 - M_h^2)^2 - 4M_a^2 M_h^2}}{2M_A}. \quad (4.1)$$

Thus, increasing M_A results in a Jacobian peak at higher E_T^{miss} , as shown in Figure 6. Conversely, models with higher M_a have a Jacobian peak at lower E_T^{miss} , as indicated in Figure 7.

In conclusion, the M_A and M_a parameters strongly affect the sensitivity of a search for the 2HDM+a model using the $h(bb) + E_T^{\text{miss}}$ signature because they determine the location of the Jacobian peak in the E_T^{miss} distribution. Therefore, one of the proposed parameter scans for the 2HDM+a model is in the (M_a, M_A) plane.

Some fraction of signal events is due to non-resonant $2 \rightarrow 3$ processes $gg \rightarrow h\chi\chi$ which is represented in ???. Due to the larger number of kinematic degrees of freedom, the invariant mass of the final state system is broadly distributed in these processes. Consequently, this results in a broad and soft E_T^{miss} distribution that is clearly distinct from the Jacobian peak discussed above. The models shown in Figure 6 and Figure 7 also have small contributions from non-resonant processes.

The mass of the heavy neutral scalar Higgs boson H has an indirect effect on the rate and kinematics of the signal. This is caused by the dependence of the coupling strengths and thus decay widths of the pseudoscalars A and a on M_H [?]. Therefore, a change of M_H can affect the relative contribution of resonant versus non-resonant signal processes, as illustrated in Figure 8. The choice $M_H = M_A$ results in a detectable total cross section for many signal points and a dominant contribution of the resonant signal process, resulting in diverse experimental signatures as demonstrated in Figure 6 and Figure 7. In addition,

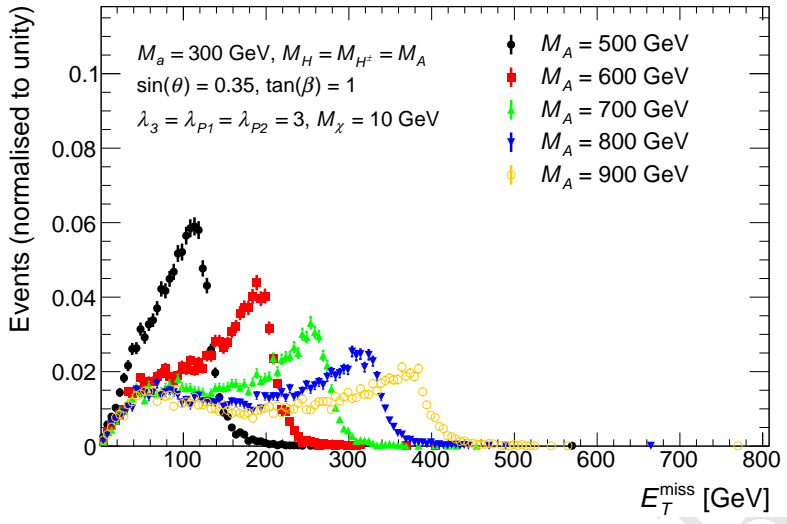


Figure 6: Missing transverse momentum distribution $h(bb) + E_T^{\text{miss}}$ signal events at parton level for five representative models with different $M_A (= M_H = M_{H^\pm})$ and fixed $M_a = 300$ GeV, $\sin \theta = 0.35$, $\tan \beta = 1$, $M_\chi = 10$ GeV and $\lambda_{P1} = \lambda_{P2} = \lambda_3 = 3$. Models with a larger $M_A - M_a$ splitting have harder E_T^{miss} (cf. Equation 4.1).

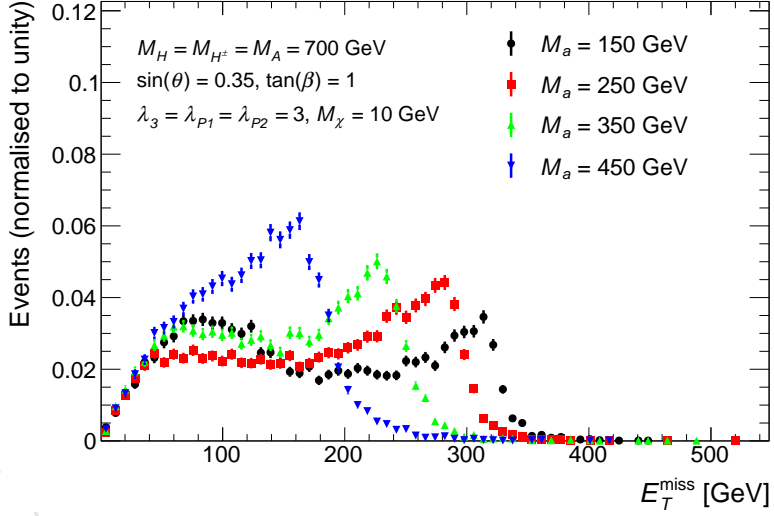


Figure 7: Missing transverse momentum distribution in $h(bb) + E_T^{\text{miss}}$ signal events at parton level for four representative models with different M_a and fixed $M_A = M_H = M_{H^\pm} = 700$ GeV, $\sin \theta = 0.35$, $\tan \beta = 1$, $M_\chi = 10$ GeV and $\lambda_{P1} = \lambda_{P2} = \lambda_3 = 3$. Models with higher M_a have softer E_T^{miss} (cf. Equation 4.1).

this choice results in about equal contributions to the sensitivity through the $Z + E_T^{\text{miss}}$ and $h + E_T^{\text{miss}}$ signatures, highlighting their complementarity. Henceforth, $M_H = M_A$ is adapted for all scans. For simplicity, the case of the neutral scalar H^\pm being mass-degenerate to H is considered in the following, as it does not affect the 2HDM+a model kinematics in the

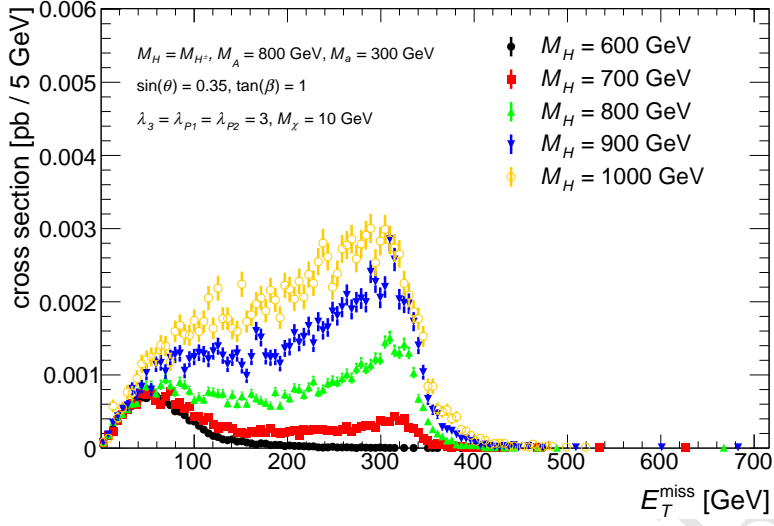


Figure 8: The E_T^{miss} distribution of the production cross section of $h(bb) + E_T^{\text{miss}}$ signal events for five representative models with different $M_H = M_{H^\pm}$ and fixed $M_A = 800$ GeV, $M_a = 300$ GeV, $\sin \theta = 0.35$, $\tan \beta = 1$, $M_\chi = 10$ GeV and $\lambda_{P1} = \lambda_{P2} = \lambda_3 = 3$.

$h(bb) + E_T^{\text{miss}}$ signature.

The sine of the mixing angle between the two pseudoscalars A and a , $\sin \theta$, affects not only the cross section, but also the shape of the E_T^{miss} distribution, as shown in Figure 9. For the resonant diagram $gg \rightarrow A \rightarrow ah \rightarrow \chi\bar{\chi}h$, the product of cross section times branching ratios $\mathcal{B}(A \rightarrow ah)\mathcal{B}(a \rightarrow \chi\bar{\chi})$ scales with $\sin^2 \theta \cos^6 \theta$, while for the diagram $gg \rightarrow a \rightarrow A^*h \rightarrow \chi\bar{\chi}h$, the product of cross section times branching ratios $\mathcal{B}(a \rightarrow Ah)\mathcal{B}(A \rightarrow \chi\bar{\chi})$ scales with $\sin^6 \theta \cos^2 \theta$. Therefore, at small $\sin \theta$, the resonant diagram $A \rightarrow ah$ is the dominant production mode and the E_T^{miss} distribution has a Jacobian peak following Equation 4.1; while at large $\sin \theta$, the $a \rightarrow A^*h$ diagram starts to dominate and produces a second peak at a lower E_T^{miss} value.

The shape of E_T^{miss} distribution also has a non-trivial dependence on $\tan \beta$, as can be seen in Figure 10. As discussed in the sensitivity study later, at small $\tan \beta$, the Yukawa coupling to top quark is large and the signal production mode is dominated by the non-resonant 3-body processes $gg \rightarrow h\chi\bar{\chi}$, which gives a broad and soft E_T^{miss} spectrum. As $\tan \beta$ increases, the contribution of resonant production increases as well and the Jacobian peak also appears. When the pseudoscalar A is produced off-shell, i.e. when $M_A < M_a + M_h$, the shapes of E_T^{miss} distributions become similar and the dependence on $\tan \beta$ disappears.

The mass of the DM fermion M_χ can change the total cross section and shape of the E_T^{miss} distribution, depending on the mass hierarchy of the A, a, h, χ particles. This is demonstrated in Figure 11. Provided on-shell decays $a \rightarrow \chi\chi$ are possible, i.e., $M_\chi < M_a/2$, the exact value of M_χ has no effect on either kinematics or the total cross section. The only exception is the case $M_a/2 > M_\chi > \frac{1}{2}(M_a - M_h)$. In this M_χ range, the non-resonant process $a \rightarrow hA^*(\chi\chi)$ is kinematically inaccessible. This reduces the overall cross section

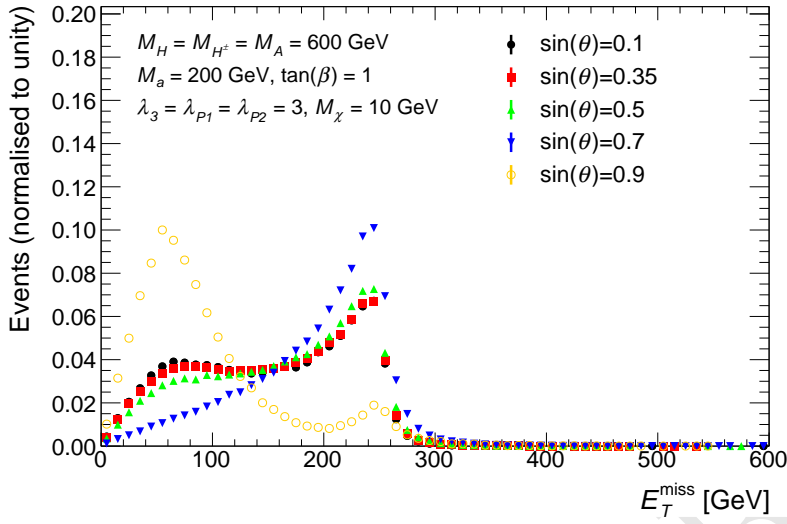


Figure 9: Missing transverse momentum distribution of $h \rightarrow bb + E_T^{\text{miss}}$ signal events at parton level for five representative models with different $\sin \theta$ and fixed $M_A = M_H = M_{H^\pm} = 600$ GeV, $M_a = 200$ GeV, $\tan \beta = 1$, and $\lambda_{P1} = \lambda_{P2} = \lambda_3 = 3$. The shape of the E_T^{miss} distribution does not change much for $\sin \theta < 0.7$, then changes significantly for $\sin \theta \geq 0.7$. When $\sin \theta = 0.9$, the diagram $gg \rightarrow a \rightarrow A^* h \rightarrow \chi\bar{\chi} h$, producing a E_T^{miss} peak at around 60 GeV, starts to dominate.

relative to the $M_\chi \leq \frac{1}{2}(M_a - M_h)$ case, and slightly changes the soft part of the total E_T^{miss} spectrum. But since the contribution of the $a \rightarrow hA^*$ ($\chi\chi$) is minor in any case, the differences are negligible.

If the DM particle mass is exactly on threshold, i.e., $M_\chi = M_a/2$, the total cross section is resonantly enhanced. This resonant threshold enhancement drops rapidly towards both higher and lower M_χ . Furthermore, the shape of the E_T^{miss} distribution at threshold, where amplitudes involving $a \rightarrow \chi\chi$ decays make up a larger fraction of the signal, differs significantly from the one below threshold. Below threshold ($M_\chi > M_a/2$), the total cross section quickly drops by several orders of magnitude. In this regime, the shape of the E_T^{miss} distribution changes with M_χ continuously.

Sensitivity estimate The sensitivity estimate of ATLAS and CMS to the 2HDM+a scenario through the $h(bb) + E_T^{\text{miss}}$ signature is based on limits on anomalous production of 125 GeV Higgs bosons in association with E_T^{miss} with minimal model dependence [?]. The limits are translated to parton level and compared to parton-level simulations of the 2HDM+a scenario for the sensitivity estimate. This approach avoids the simulation of the detector response, which requires a significant amount of computing resources, and more iterations and refinements of the signal grid can be performed.

The limits with minimal model dependence are provided in terms of the detector-level cross section of $h(bb) + E_T^{\text{miss}}$ events $\sigma_i^{\text{obs}, h(bb)+E_T^{\text{miss}}}$ as a function of E_T^{miss} in four bins $i = 1, \dots, 4$ [?]. To compare these values to the simulation results at parton level, an estimate

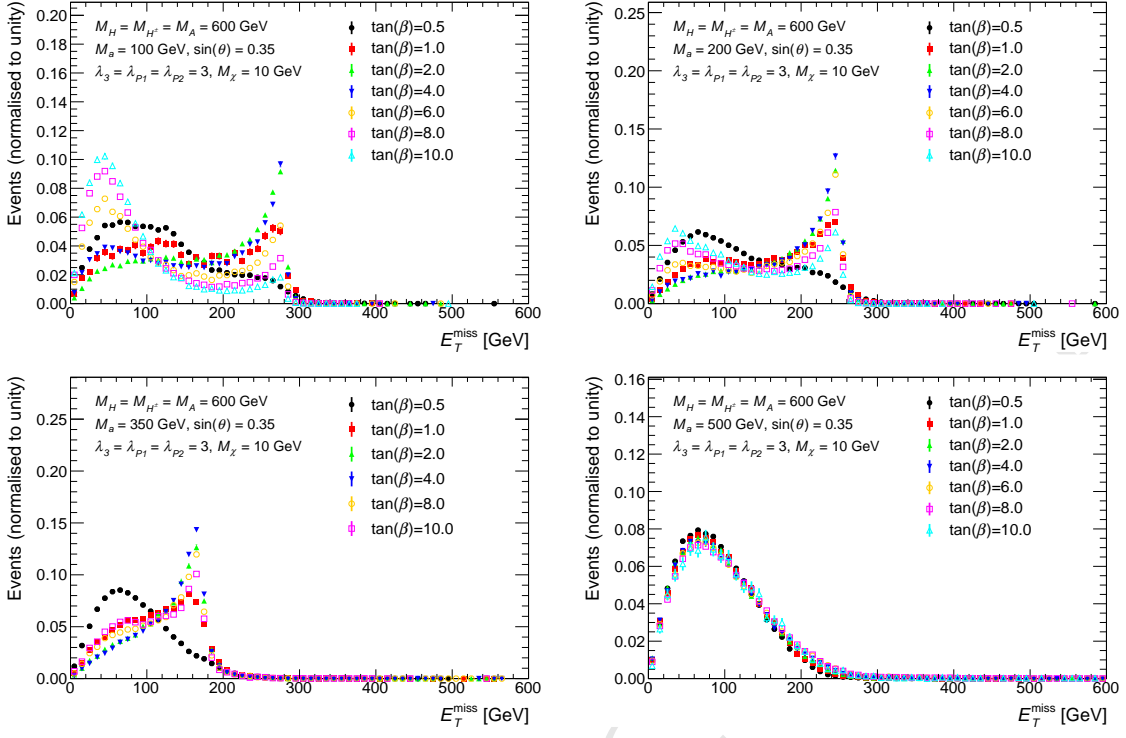


Figure 10: Missing transverse momentum distribution of $h \rightarrow bb + E_T^{\text{miss}}$ signal events at parton level with different $\tan\beta$ and fixed $M_A = M_H = M_{H^\pm} = 600 \text{ GeV}$, $M_\chi = 10 \text{ GeV}$, $\sin\theta = 0.35$, and $\lambda_{P1} = \lambda_{P2} = \lambda_3 = 3$. The values of M_a are set to 100, 200, 350, and 500 GeV, respectively. The shapes of the E_T^{miss} distributions for different $\tan\beta$ are similar when $M_A < M_h + M_a$. Note, in these figures, both the contributions of gg and $b\bar{b}$ initiated processes are included and a combined histogram is produced according to their corresponding cross sections.

of the detection efficiency ε times the kinematic acceptance \mathcal{A} of the event selections of the analysis is used for each of the four E_T^{miss} bins. Thus, the $(\mathcal{A} \times \varepsilon)_i$ figure represents the minimum probability that an event generated at parton level in a given E_T^{miss} bin i is reconstructed in that same E_T^{miss} bin and passes all analysis selections. Consequently, the cross section for $h + \text{DM}$ production in the 2HDM+a scenario at parton level $\sigma_i^{\text{parton}, h+\text{DM}}$ is calculated in the same E_T^{miss} bins as used in the $h(bb) + E_T^{\text{miss}}$ search. This starting point is shown in Figure 12 using the scan in (M_A, M_a) as a representative example. In the next step, the sensitivity S_i for each of the E_T^{miss} bins $i = 1, \dots, 4$ is calculated as

$$S_i \equiv \frac{\sigma_i^{\text{parton}, h+\text{DM}} \times \mathcal{B}^{\text{SM}, h \rightarrow bb} \times (\mathcal{A} \times \varepsilon)_i}{\sigma_i^{\text{obs}, h(bb) + E_T^{\text{miss}}}}, \quad (4.2)$$

where $\mathcal{B}^{\text{SM}, h \rightarrow bb}$ is the $h \rightarrow bb$ branching ratio predicted by the SM for the 125 GeV Higgs boson. A representative example for this step is given in Figure 13 for the scan in (M_A, M_a) . A particular point in the (M_A, M_a) parameter space is excluded if $S_i \geq 1$. Finally, to obtain a single estimate for the total sensitivity S_{tot} using all four E_T^{miss}

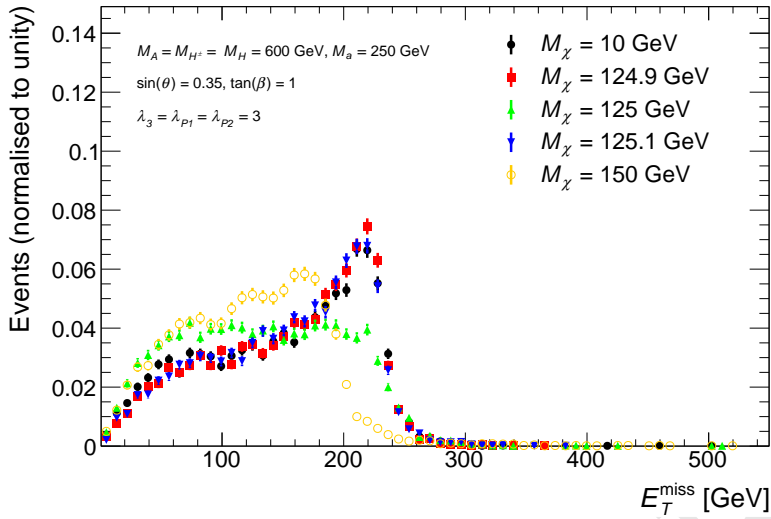


Figure 11: Missing transverse momentum distribution of $h(bb) + E_T^{\text{miss}}$ signal events at parton level for five representative models with different M_χ and fixed $M_A = M_H = M_{H^\pm} = 600$ GeV, $M_a = 250$ GeV, $\sin \theta = 0.35$, $\tan \beta = 1$ and $\lambda_{P1} = \lambda_{P2} = \lambda_3 = 3$. The shape of the E_T^{miss} distribution does not change for $M_\chi < M_a/2$, then changes significantly for $M_\chi \geq M_a/2$.

bins, their individual contributions from Equation 4.2 are summed over²:

$$\mathcal{S}_{\text{tot}} \equiv \sum_{i \in E_T^{\text{miss}} \text{ bins}} \mathcal{S}_i. \quad (4.3)$$

The resulting \mathcal{S}_{tot} is shown in Figure 14 for the example of the (M_A, M_a) scan.

The scan of the sensitivity in the sense of Equation 4.3 in the (M_a, M_A) plane is shown in Figure 14. The sensitivity decreases with increasing $M_A = M_H = M_{H^\pm}$ for $M_A \geq 1$ TeV because the fraction of resonant signal events drops. This drop is caused by increasingly large Γ_A , which allows for an increasing fraction of non-resonant signal events, driven by events with very off-shell A . Near the mass diagonal $M_a = M_A$, there is little to no sensitivity. This is because the Jacobian peak moves to low E_T^{miss} for a small mass splitting $|M_A - M_a|$ (Equation 4.1, Figure 6, and Figure 7). Beyond this, the coupling g_{Aah} is small when all Higgs bosons are nearly degenerate in mass, cf. Equation 4.12 in Ref. [?], resulting in a small total cross section and therefore further decrease in sensitivity. The sensitivity above the mass diagonal, $M_A > M_a$, is larger than below the mass diagonal. Two parameter choices cause this asymmetry:

1. $M_A = M_H = M_{H^\pm}$, i.e., the neutral and charged CP -even scalars have low masses below the diagonal, but high masses above it, introducing an asymmetry. Another

² This choice is made because the individual per-bin sensitivities follow a logarithmic metric, and because a model will typically populate several E_T^{miss} bins at a time. This implies that there could be models where $\mathcal{S}_i < 1$ in every bin, yet the sum from Equation 4.3 is > 1 . Therefore, for a rigorous exclusion of a model based on the limits with minimal model dependence, the preferred approach would be to consider only the most sensitive bin for the exclusion.

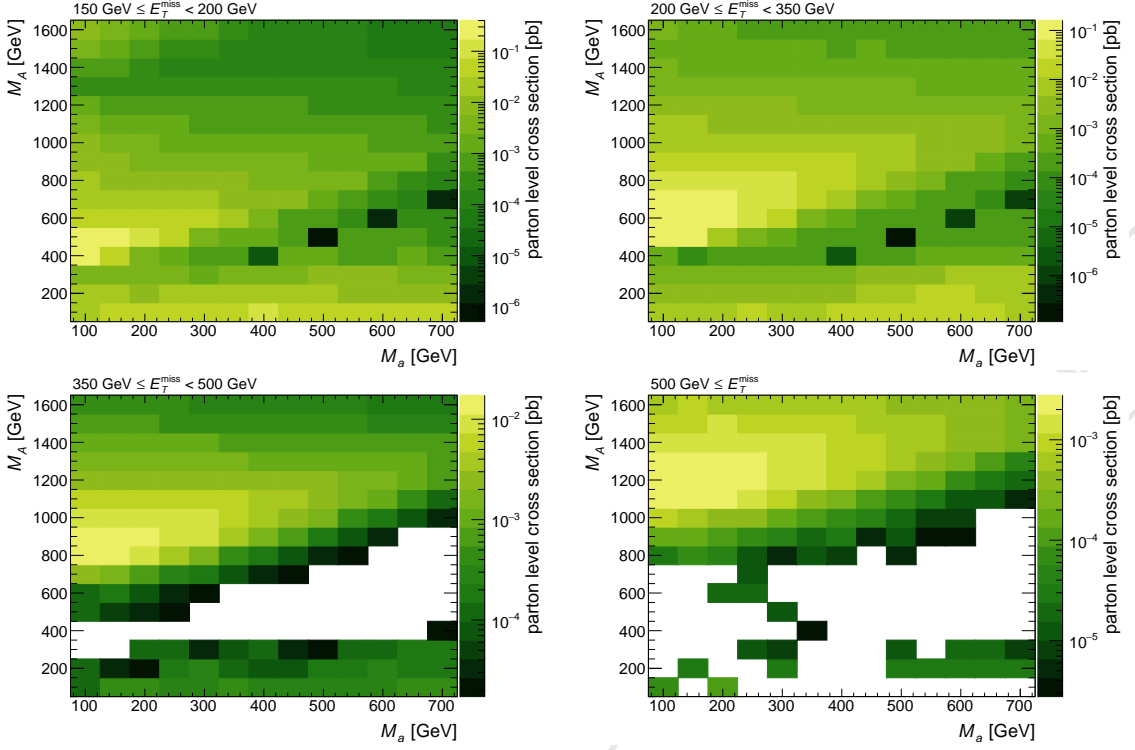


Figure 12: The production cross section of $h \rightarrow bb + E_T^{\text{miss}}$ signal events at parton level as a function of (M_A, M_a) in each of the four E_T^{miss} bins. The remaining parameters take the values $M_H = M_{H^\pm} = M_A$, $\sin \theta = 0.35$, $\tan \beta = 1$, $M_\chi = 10$ GeV and $\lambda_{P1} = \lambda_{P2} = \lambda_3 = 3$.

effect can be seen in Figure 8: values of $M_H = M_{H^\pm}$ below the mass of the higher-mass pseudoscalar (in this case A) give a reduced total cross section and a lower fraction of resonant signal events. Both effects reduce sensitivity;

2. $\sin \theta = 0.35 \neq 1/\sqrt{2}$, i.e. the mixing between the pseudoscalars A and a is asymmetric. A couples more strongly to SM particles than a , and vice versa for the couplings to the DM fermion χ . So the situation below the diagonal corresponds to the case of $\sin \theta = \sqrt{1 - 0.35^2} \approx 0.938$ and $M_A > M_a$. As can be seen in Figure 9, this $\sin \theta$ configuration has a higher fraction of non-resonant signal events with low E_T^{miss} , and correspondingly a lower sensitivity is found in Figure 15.

The scan of the sensitivity in the $(M_a, \tan \beta)$ plane is shown in Figure 16. At very low $\tan \beta$, the Yukawa coupling to top quarks is large, and most of the signal events come from non-resonant processes, as can be seen from Figure 10. The non-resonant processes are characterised by soft E_T^{miss} , which lowers the kinematic acceptance and reduces the sensitivity of the search. For higher $\tan \beta$, the fraction of resonant events increases due to the reduced top Yukawa coupling, resulting in an increase of sensitivity. However, reducing the top Yukawa coupling also reduces the total production cross section. This effect is sub-dominant below $\tan \beta \approx 1.2$, and the sensitivity increases with $\tan \beta$. But above $\tan \beta \approx 1.2$, the sensitivity loss due to reduced cross section outpaces the sensitivity gain

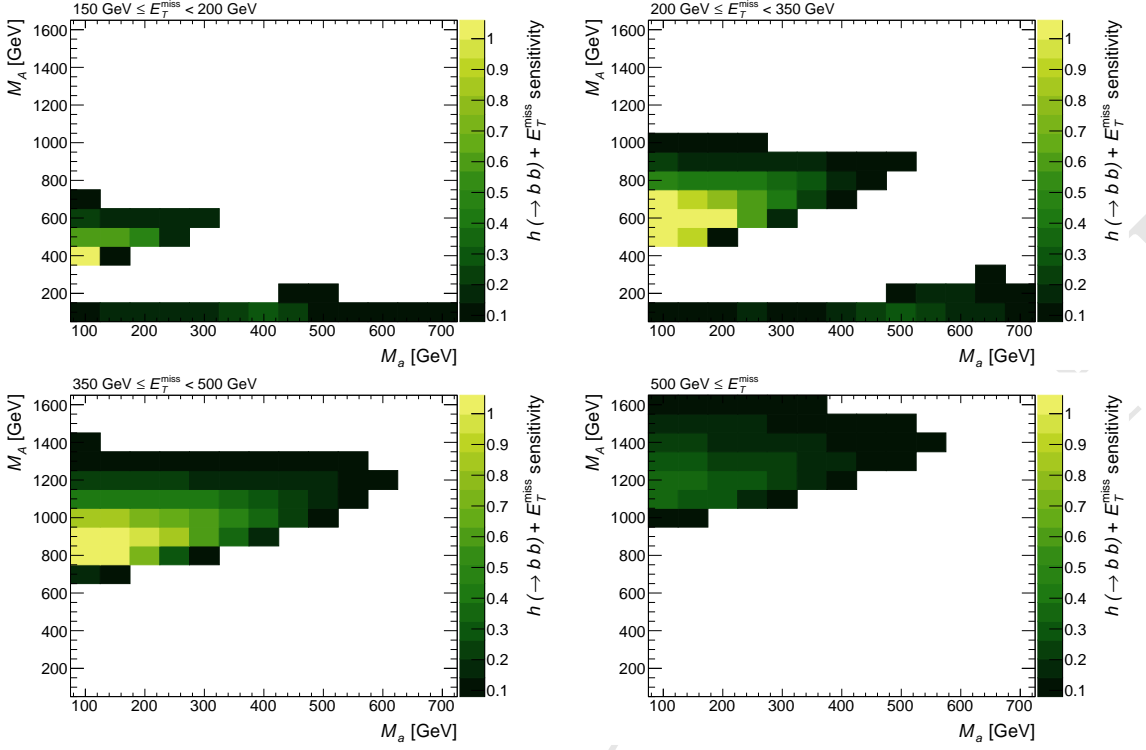


Figure 13: Estimated sensitivity to $h \rightarrow bb + E_T^{\text{miss}}$ events as a function of (M_A, M_a) in each of the four E_T^{miss} bins. The sensitivity, defined in Equation 4.3, is based on the limits with reduced model dependence from Ref. [?]. The remaining parameters take the values $M_H = M_{H^\pm} = M_A$, $\sin \theta = 0.35$, $\tan \beta = 1$, $M_\chi = 10$ GeV and $\lambda_{P1} = \lambda_{P2} = \lambda_3 = 3$.

due to a more resonant signal. Overall, the search gets less sensitive with increasing $\tan \beta$ above $\tan \beta \approx 1.2$. At very high $\tan \beta$ (≥ 10), this trend is reversed again because the $\tan \beta$ enhancement³ of the coupling to b -quarks compensates for the small b -quark mass. At this point bb initiated processes start to dominate the production cross section and drive the increase in sensitivity.

The sensitivity to models with varying $\sin \theta$ is shown in Figure 15. The sensitivity vanishes at $\sin \theta = 0$ and $\sin \theta = 1$, since those values correspond to no mixing between A and a , and thus no connection between the SM and the dark sector. For its intermediate values, the $\sin \theta$ parameter influences the couplings of the pseudoscalars to DM as well as to SM fermions, and also the coupling strength of trilinear scalar vertices such as g_{Aah} [?]. Increasing the couplings increases the total cross section. However, increasing some couplings can also increase Γ_A and thereby decrease the resonant fraction of signal events and the sensitivity. The upshot of this is that there can be more than one local maximum in the sensitivity curve, as shown the right panel of Figure 15. The precise dependence of the sensitivity on $\sin \theta$ depends on the precise interplay of the couplings. Because the couplings depend on all other model parameters including all the Higgs masses, tuning the $\sin \theta$ of a parameter scan to the sensitivity in a single point can lead to sub-optimal

³The 2HDM+a scenario assumes a Yukawa sector of type II.

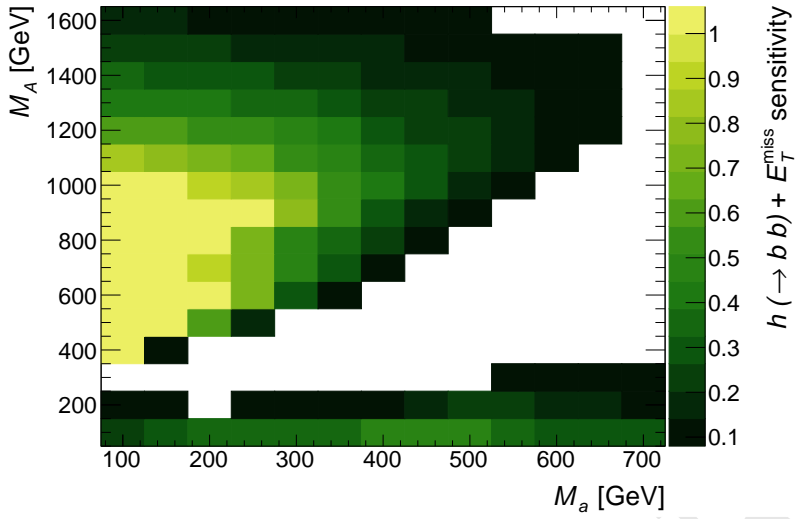


Figure 14: Sum over all E_T^{miss} -bins of the estimated sensitivity to $h \rightarrow bb + E_T^{\text{miss}}$ events as a function of (M_A, M_a) . The sensitivity, defined in Equation 4.3, is based on the limits with reduced model dependence from Ref. [?]. The remaining parameters take the values $M_H = M_{H^\pm} = M_A$, $\sin \theta = 0.35$, $\tan \beta = 1$, $M_\chi = 10$ GeV and $\lambda_{P1} = \lambda_{P2} = \lambda_3 = 3$.

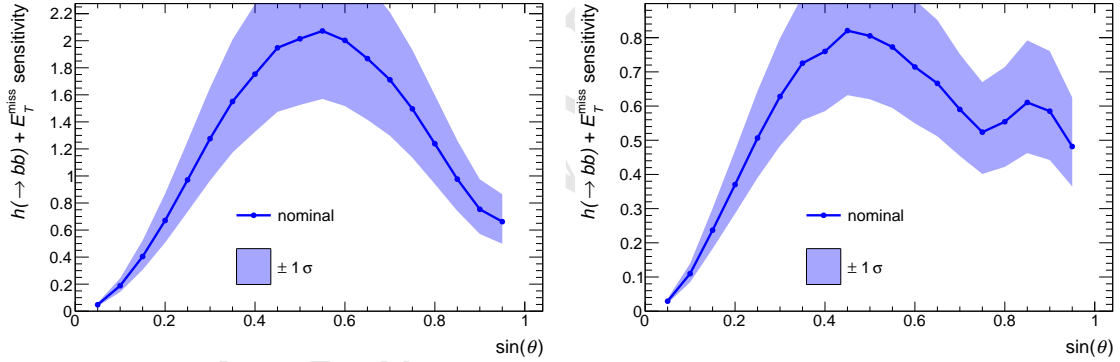


Figure 15: Sum over all E_T^{miss} -bins of the estimated signal sensitivity to $h \rightarrow bb + E_T^{\text{miss}}$ events as a function of the pseudoscalar mixing parameter $\sin \theta$, for $M_a = 200$ GeV and $M_H = M_{H^\pm} = M_A = 600$ GeV (left) as well as $M_a = 350$ GeV and $M_H = M_{H^\pm} = M_A = 1000$ GeV (right). The remaining parameters take the values $M_\chi = 10$ GeV, $\tan \beta = 1$, and $\lambda_{P1} = \lambda_{P2} = \lambda_3 = 3$. The sensitivity, defined in Equation 4.3, as well as the uncertainty on the sensitivity (shaded blue) are based on the limits with reduced model dependence from Ref. [?] and the uncertainties described therein.

sensitivity in other points.

The sensitivity to models with varying M_χ is shown in Figure 17. Below the threshold of $M_\chi < M_a/2$, the sensitivity is constant since the E_T^{miss} distribution and the total signal cross section remain invariant, as demonstrated in Figure 11. At threshold, the sensitivity is enhanced because the partial width for $a \rightarrow \chi\chi$ is enhanced, increasing the signal cross

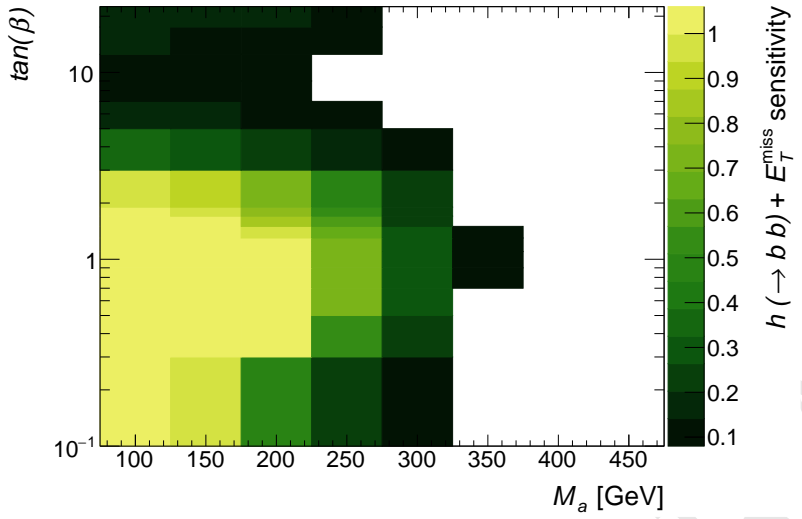


Figure 16: Sum over all E_T^{miss} -bins of the estimated signal sensitivity to $h \rightarrow bb + E_T^{\text{miss}}$ events as a function of $(M_a, \tan \beta)$. The sensitivity, defined in Equation 4.3, is based on the limits with reduced model dependence from Ref. [?]. The remaining parameters take the values $M_H = M_{H^\pm} = M_A = 600$ GeV, $\sin \theta = 0.35$, $M_\chi = 10$ GeV and $\lambda_{P1} = \lambda_{P2} = \lambda_3 = 3$.

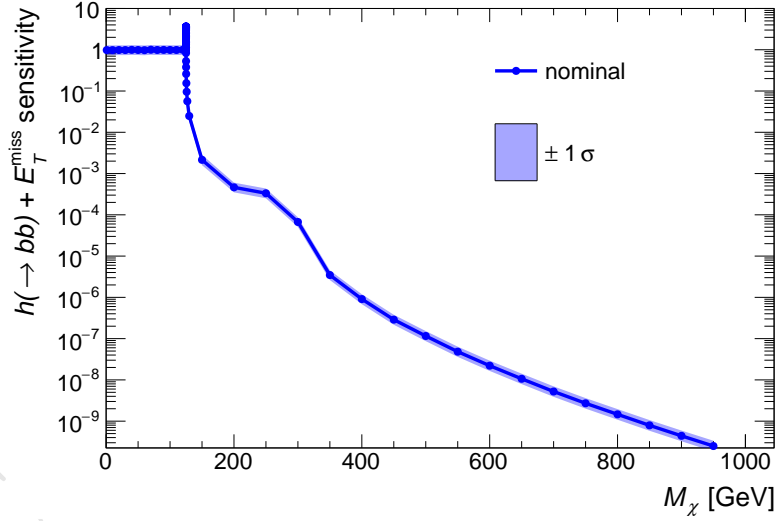


Figure 17: Sum over all E_T^{miss} -bins of the estimated signal sensitivity to $h \rightarrow bb + E_T^{\text{miss}}$ events as a function of the DM mass M_χ . The sensitivity, defined in Equation 4.3, as well as the uncertainty on the sensitivity (shaded blue) are based on the limits with reduced model dependence from Ref. [?] and the uncertainties described therein. The remaining parameters take the values $M_a = 250$ GeV, $M_H = M_{H^\pm} = M_A = 600$ GeV, $\sin \theta = 0.35$, $\tan \beta = 1$, and $\lambda_{P1} = \lambda_{P2} = \lambda_3 = 3$. The sensitivity is constant below $M_\chi < M_a/2$, and rapidly drops for $M_\chi > M_a/2$. The sensitivity is resonantly enhanced for $M_\chi = M_a/2$.

section. Above threshold, the sensitivity drops rapidly because $M_\chi > M_a/2$ requires an off-shell $a^* \rightarrow \chi\chi$ decay, which is strongly suppressed by the typically narrow width of a . The width of a is substantially reduced once $a \rightarrow \chi\chi$ is kinematically inaccessible, as $\Gamma_{a \rightarrow \chi\chi}$ is a large contribution to the total width of a for $M_\chi \leq M_a/2$ [?]. There is a slight increase in sensitivity for $M_\chi \approx M_a/2$ when the $A \rightarrow \chi\chi$ decay hits its kinematic threshold, yet the absolute sensitivity remains negligible.

4.1.3 Studies of the mono-Z (leptonic) signature

Mono-Z analyses use events with a Z boson recoiling symmetrically against E_T^{miss} to detect the production of invisible particles. In previous LHC analyses [? ?], the DM interpretations of the analysis results have focused on either invisible decays of the SM-like Higgs bosons or topologies where the Z boson is produced as initial-state radiation (ISR) off a quark. The ISR-based topologies generically favor radiation of a gluon or photon rather than a massive gauge boson, thus limiting the discovery sensitivity of a Z-based approach compared to monojet and mono-photon searches. In contrast, the model studied in this document generates the mono-Z signature dominantly via the all-bosonic H-a-Z vertex, which can lead to enhancements in the mono-Z sensitivity compared to jet and photon signatures. In this section, the behavior and experimental accessibility of the model in $Z+E_T^{\text{miss}}$ events is studied.

Technical setup Simulated event samples for the leptonic mono-Z signature are produced with Madgraph5_aMC@NLO version 2.4.3, interfaced with Pythia version 8.2.2.6 for parton showering. The NNPDF3.0 PDF set is used at LO precision with the value of the strong coupling constant set to $\alpha_S(M_Z) = 0.130$ (NNPDF30_lo_as_0130). A five flavor scheme with a massless b-quark is used. Only contributions from gluon-gluon initial states and $l^+ l^- \chi\bar{\chi}$ final states are considered, where $l = e$ or μ . The bb initiated ME contribution is negligible for the range of $\tan\beta$ values studied. To increase calculation efficiency diagrams with an intermediate s-channel SM Higgs boson are explicitly rejected (generate g g > xd xd l+ l- / h1).

Event selection Three consecutive stages of event selection are considered:

- Inclusive: Lepton p_T and η requirements corresponding to the typical experimental trigger acceptance are applied.
- Preselection: A dilepton candidate with an invariant mass in a window around the Z mass is required, and a minimum transverse momentum of the $\chi\bar{\chi}$ system is required.
- Final selection: Requirements on the main discriminating variables used in the relevant analyses are added: The angular separation in the transverse plane between the $\chi\bar{\chi}$ and $l^+ l^-$ systems $\Delta\Phi(l\bar{l}, E_T^{\text{miss}})$, the relative transverse momentum difference between them $|p_{T,l\bar{l}} - E_T^{\text{miss}}|/p_{T,l\bar{l}}$ and the angular separation between the leptons $\Delta R(l\bar{l})$. Additionally, the E_T^{miss} requirement is tightened.

The exact event selection criteria are listed in Tab. 3.

Table 3: Event selection requirements for the analysis of the Mono-Z signature with leptonic Z decays. The requirements are inspired to follow those used in typical experimental analyses.

Selection stage	Quantity	Requirement
Inclusive	lepton $ \eta $	< 2.5
	leading (trailing) lepton p_T	$> 25(20)$ GeV
Preselection	$ m_{ll} - m_{Z,\text{nominal}} $	< 15 GeV
	E_T^{miss}	> 40 GeV
	$\Delta\Phi(ll, E_T^{\text{miss}})$	> 2.7
	$ p_{T,ll} - E_T^{\text{miss}} /p_{T,ll}$	< 0.4
Final selection	$\Delta R(ll)$	< 1.8
	E_T^{miss}	> 80 GeV

Cross-sections, kinematic distributions, and acceptances The overall cross-sections in the $\tan\beta$ and mass scans are shown in Fig. 18. In the mass scan, maximal cross-sections are observed for the region of $M_a < M_A$ for values of $M_a \gtrsim 100$ GeV. Towards higher values of both M_a and M_A , the cross-sections fall off, reaching values smaller than 1 fb at $M_a \approx 450$ GeV or $M_A \approx 1.1$ TeV. In the $M_a \approx M_A$ -region, the cross-section is suppressed by destructive interference. For the region with inverted mass hierarchy $M_a > M_A$, cross-sections of the order of multiple fb are observed, as long as $|M_a - M_A|$ remains sufficiently large. In the $\tan\beta$ scan, cross-sections smoothly fall with increasing M_a as well as $\tan\beta$. Cross-sections are typically larger than 1 fb up to $\tan\beta \approx 5$. The M_a dependence is modulated by the value of $\tan\beta$: Crossing the M_a range from 100 to 400 GeV, cross-sections are reduced by a factor ≈ 7 for small $\tan\beta \approx 1$, but only a factor ≈ 2 for higher values of $\tan\beta \approx 5$. In the $\sin\theta$ scan shown in Figure 19, cross sections depends on whether or not the $a \rightarrow \bar{t}t$ decays are accessible. For $M_a < 350$ GeV they are not accessible and cross section strictly increases with $\sin\theta$. For $M_a > 350$ GeV, the $a \rightarrow \bar{t}t$ decays become possible causing the cross section to decrease for large values of $\sin\theta$.

To assess the kinematic behavior of the signal, distributions of kinematic variables most relevant to the Mono-Z signature are studied as a function of the model parameters. Inclusive distributions of the invariant masses of the dilepton and $\chi\chi$ systems are shown in Fig. 24. Independent of the parameters, the dilepton mass spectrum is centered at the Z peak, without any nonresonant contribution. The $M_{\chi\chi}$ distribution illustrates the signal contributions from different diagrams. For $M_A > M_a$, DM is dominantly produced from on-shell a boson production. In the inverted mass region $M_A < M_a$, the situation is reversed, and H diagrams dominate.

After applying the preselection requirements, scans of the model parameters are performed. For this paper a subset of models are studied where M_A is degenerate with M_H . Similar to mono-h, for mono-Z in the region $M_A > M_a$ a resonantly produced heavy scalar, H , decaying to aZ produces a characteristic Jacobian peak in the E_T^{miss} distribution. The location of the peak depends on M_H and M_a as given by equation 4.4, and the peak's width generally increases with values of M_a and M_A .

$$E_T^{\text{miss},\text{max}} \approx \frac{\sqrt{(M_H^2 - M_a^2 - M_Z^2)^2 - 4M_a^2 M_Z^2}}{2M_H}. \quad (4.4)$$

Figure 23 shows the Jacobian peaks for increasing values of M_H and fixed M_a . Significant portions of the spectrum are situated at relatively high boosts ($E_T^{\text{miss}} > 200 \text{ GeV}$), which is more easily accessible experimentally. This behavior is contrasted by the distributions in the inverted mass regions, which have nearly no distinct features and are mainly located at low mediator p_T . For $M_A \approx M_a + m_Z$, both the a and Z bosons are produced approximately at rest, leading to an event population with overall low boost. These qualitative trends are consistent with the distributions of the other main selection variables as shown in Fig. 25.

Scans of the $\tan \beta$ and $\sin \theta$ parameters show they have minimal effect on the kinematic distributions (Fig. 26). For small values of $\tan \beta$ there is a slight softening and broadening of the E_T^{miss} distribution caused by the increased contribution from non-resonant $z + a$ production.

For M_χ (Fig. 27, in the region where $M_\chi < \frac{M_a}{2}$, DM mass has no effect on cross section or the kinematic distributions. In the off-shell region where $M_\chi > \frac{M_a}{2}$ cross section steeply drops and the E_T^{miss} distribution becomes less structured.

Finally, the distributions of the E_T^{miss} and M_T variables after final selection are shown in Fig. 28. Traditionally, the Mono-Z search has relied on the E_T^{miss} distribution for signal extraction. While the presence of the Jacobian peak structure in the distribution facilitates signal-background separation, it may be beneficial to also consider the M_T distribution. Although only transverse information is available, the resonant structure of the signal is significantly enhanced in the M_T variable, which may enhance the sensitivity of a specialized search strategy.

Acceptances for the mass and $\tan \beta$ scans are shown in Figures 20 and 21. In the mass scan, for points where the Jacobian peak is below the analysis's E_T^{miss} cut, from $M_a = 100$ $M_A = 200$ to $M_a = 300$ $M_A = 400$, acceptance drops sharply approaching zero. Above this region, acceptance levels are grouped into bands for fixed values of $M_A - M_a$. With increasing $M_A - M_a$ acceptances increases, gradually plateauing to a maximum value of 50%. In the inverted mass region, acceptances are generally lower than the rest of the mass scan, but for light values of M_a can reach values as large as 30%. In the $\tan \beta$ scan, acceptances are largely independent of $\tan \beta$ and constant for equal values of M_a . For small values of $\tan \beta$ and $M_a < 350 \text{ GeV}$ there is slight drop in the acceptance caused by the softer E_T^{miss} distribution from non-resonant decays.

Expected significance The expected sensitivity of the Mono-Z(ll) channel to 2HDM+a models is approximated using generator level signal samples and background estimates from recent $Z(\ell\ell) + E_T^{\text{miss}}$ searches using 36.1 fb^{-1} of 13 TeV data [?]. For signal events a reconstruction efficiency of 75% is assumed, and to be consistent with the background estimates, the same selection cuts as [?] are used. Signal and background are binned in E_T^{miss} and a conservative background systematic of 20% is assumed for $E_T^{\text{miss}} < 120 \text{ GeV}$ and 10% above.

Total significance is defined as the per bin significances summed in quadrature.

$$\mathcal{S} = \sqrt{\sum_{bin} (Z'_{bin})^2} \quad (4.5)$$

Following the Asimov approximation, the significance for individual bins is calculated as a Poisson ratio of likelihoods modified to incorporate systematic uncertainties on the background [?]:

$$Z'_{bin} = \sqrt{2 \cdot \left((s+b) \ln\left[\frac{(s+b)(b+\sigma_b^2)}{b^2 + (s+b)\sigma_b^2}\right] - \frac{b^2}{\sigma_b^2} \ln\left[1 + \frac{\sigma_b^2 s}{b(b+\sigma_b^2)}\right] \right)} \quad (4.6)$$

This metric has the advantage that it accounts for background systematics and is still valid for s not $\ll b$. Expected significances are shown in Figure 29, with regions the ATLAS and CMS experiments should be sensitive to, greater than 2, highlighted.

Conclusions The Mono-Z(ll) provides experimental coverage of the pseudoscalar 2HDM model for a broad part of the parameter space. The light pseudoscalar a can be probed up to mass values of ≈ 350 GeV, depending on the choice of parameters. The Mono-Z channel is sensitive mostly in the region of $\tan \beta < 4$.

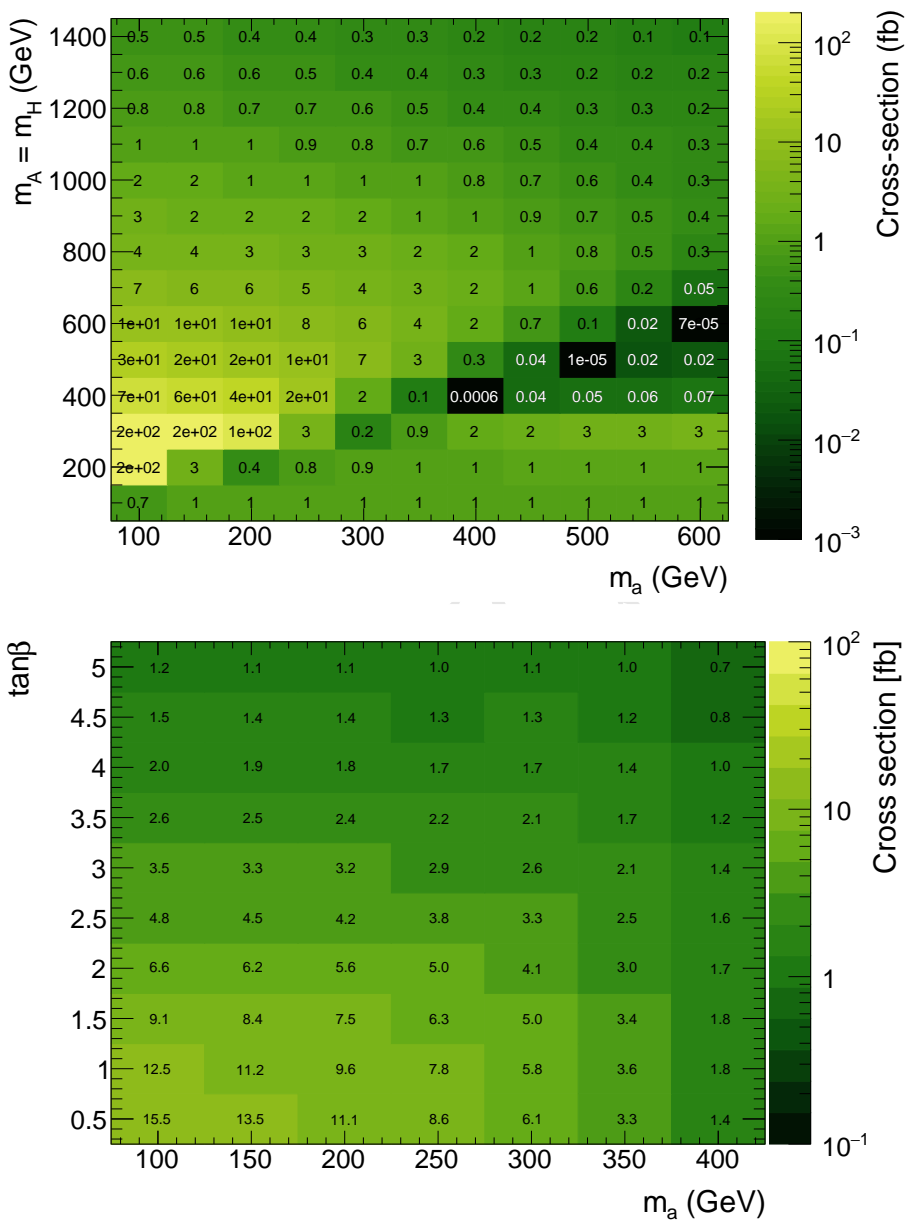


Figure 18: Inclusive cross-sections for $pp \rightarrow l^+l^-\chi\bar{\chi}$ in the M_a - M_A (top) and M_a - $\tan\beta$ scans (bottom).

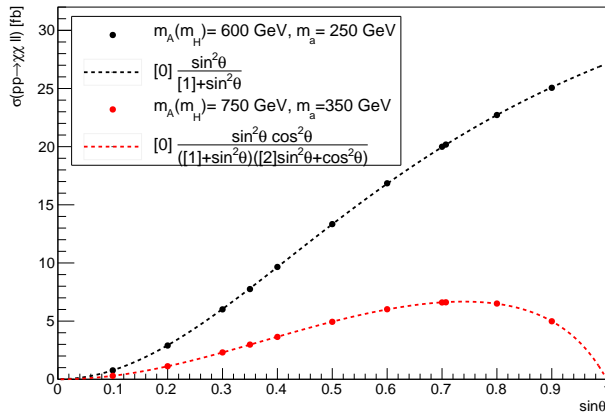


Figure 19: For two different mass points, this figure shows the cross section $pp \rightarrow \chi\chi\ell\ell$ as a function of $\sin \theta$. For $M_a < 350$ GeV, a decays solely to dark matter particles. As a consequence, the mixing angle only impacts the heavy scalar's branching fraction to aZ and cross section strictly increases with $\sin \theta$. For M_a above 350 GeV, $t\bar{t}$ decays become accessible, introducing additional $\sin \theta$ and $\cos \theta$ dependences for the branching fraction of $a \rightarrow \chi\chi$. For M_a above 350 GeV for large values of $\sin \theta$, there is a turnover point where the reduced $a \rightarrow \chi\chi$ branching fraction outweighs the increased $H \rightarrow aZ$ branching and the net cross section decreases.

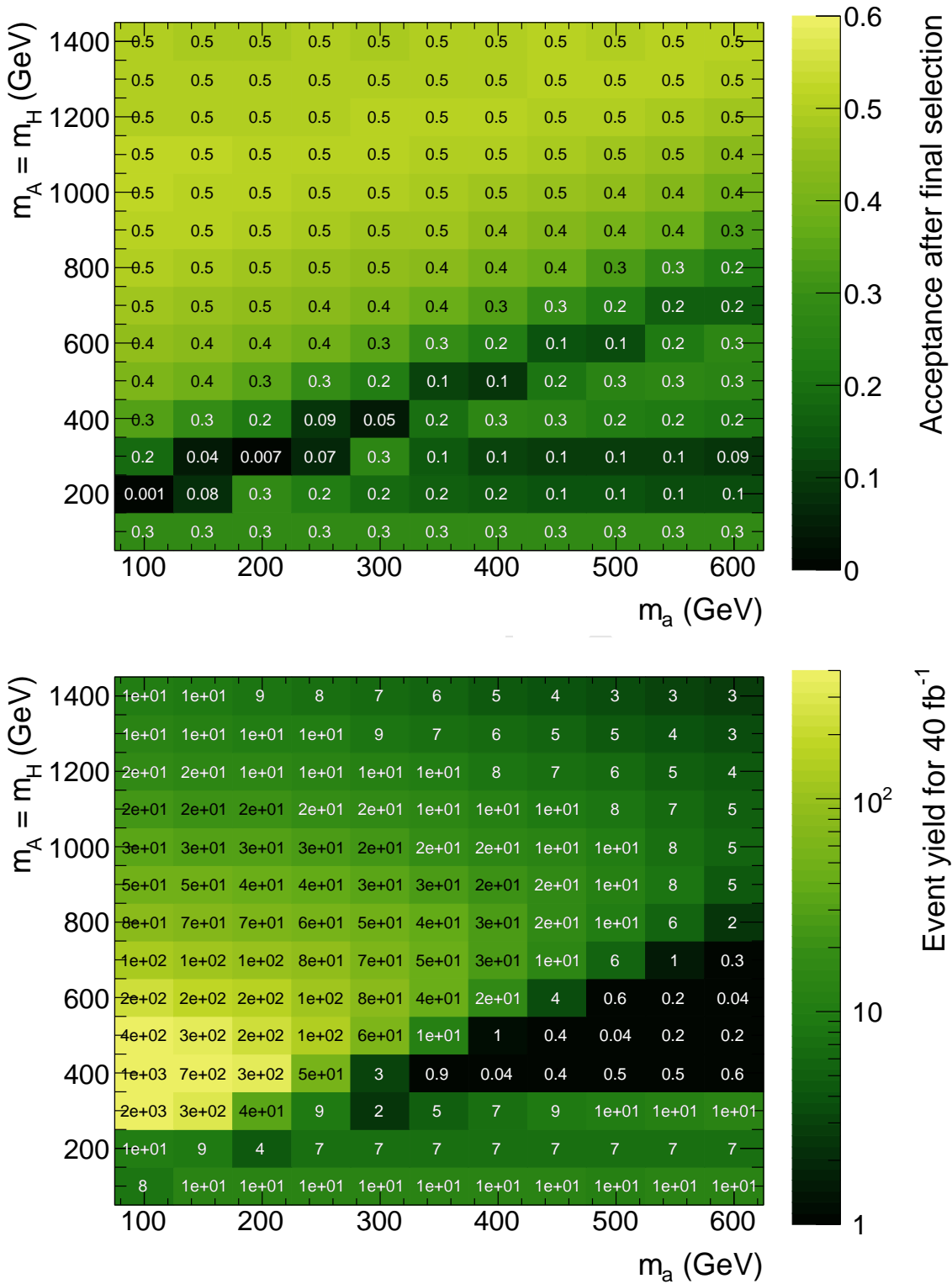


Figure 20: Acceptance and event yields in the M_a - M_A plane after applying the final selection. Event yields assume an integrated luminosity of 40 fb^{-1} . The acceptance is maximal for $M_A > M_a$, where it reaches 50 %. In the inverted mass region $M_A < M_a$, lower values of 10-30% are observed. In the intermediate region around $M_A \approx M_a + M_Z$, the acceptance is strongly suppressed as the a and Z bosons are produced approximately at rest.

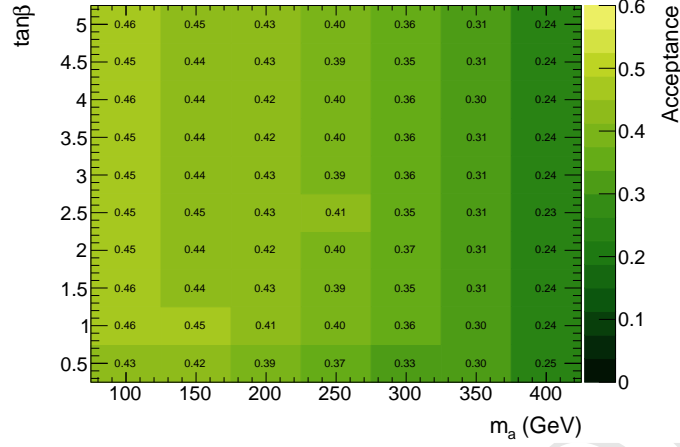


Figure 21: Acceptances across the M_a - $\tan\beta$ scan. Acceptance is flat over $\tan\beta$ for constant values of M_a .

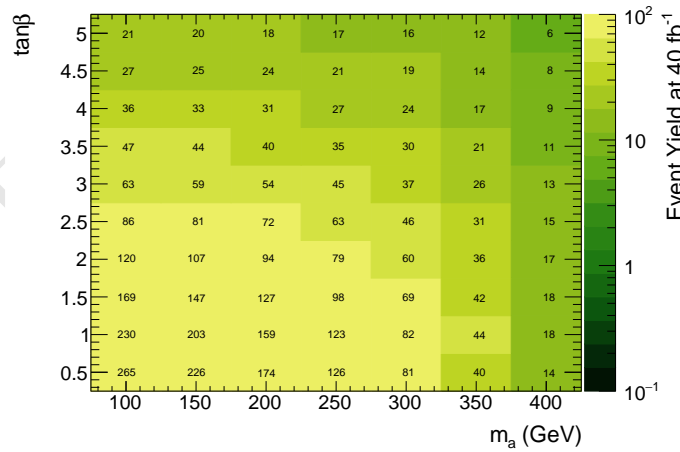


Figure 22: Event yield in the M_a - $\tan\beta$ grid, for an integrated luminosity of 40 fb^{-1} . The number of expected events diminishes with increasing $\tan\beta$ and M_a . M_A fixed to 600 GeV and $\sin\Theta$ to 0.35

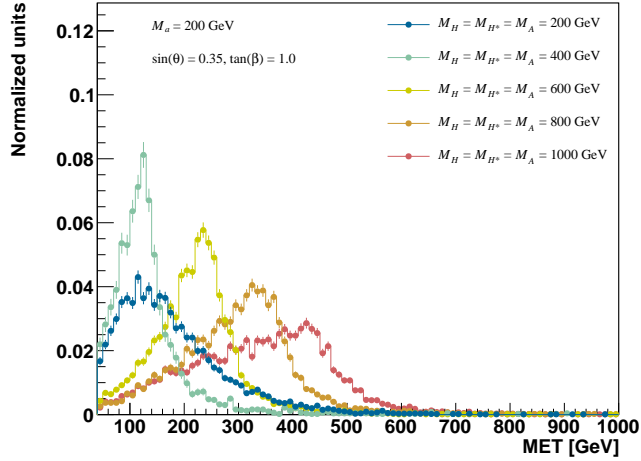


Figure 23: The position of the Jacobian peak in the E_T^{miss} distribution depends on the values of M_H , M_a , and M_Z . This figure shows a scan of M_H values for fixed M_a and $M_A = M_H$. Increasing the difference between M_H and M_a shifts the location of the peak towards high energies, whereas for small mass splittings the E_T^{miss} distribution is soft and most events will fail to pass the E_T^{miss} selection criteria.

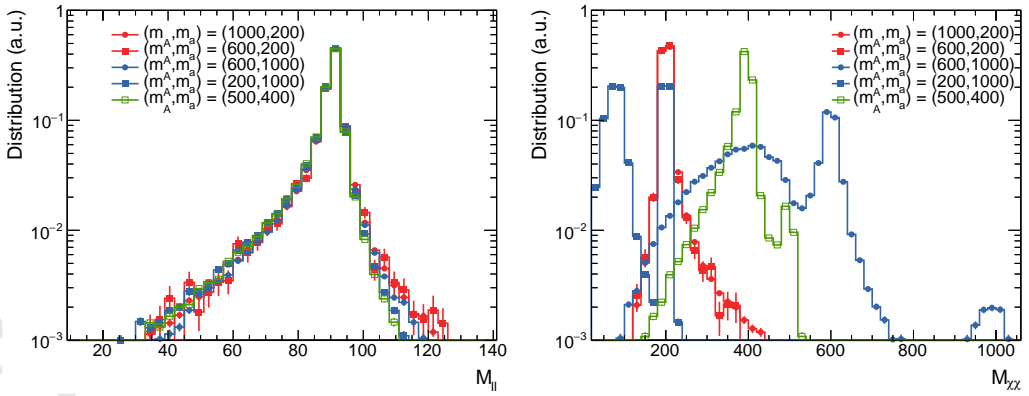


Figure 24: Distributions of the invariant mass of the dilepton (left) and $\chi\bar{\chi}$ systems (right) with no selection applied in addition to the generation cuts. The M_{ll} distribution is centered around the Z boson mass independent of the chosen parameter point, indicating that there is no contribution from γ^* exchange. The $M_{\chi\bar{\chi}}$ distribution

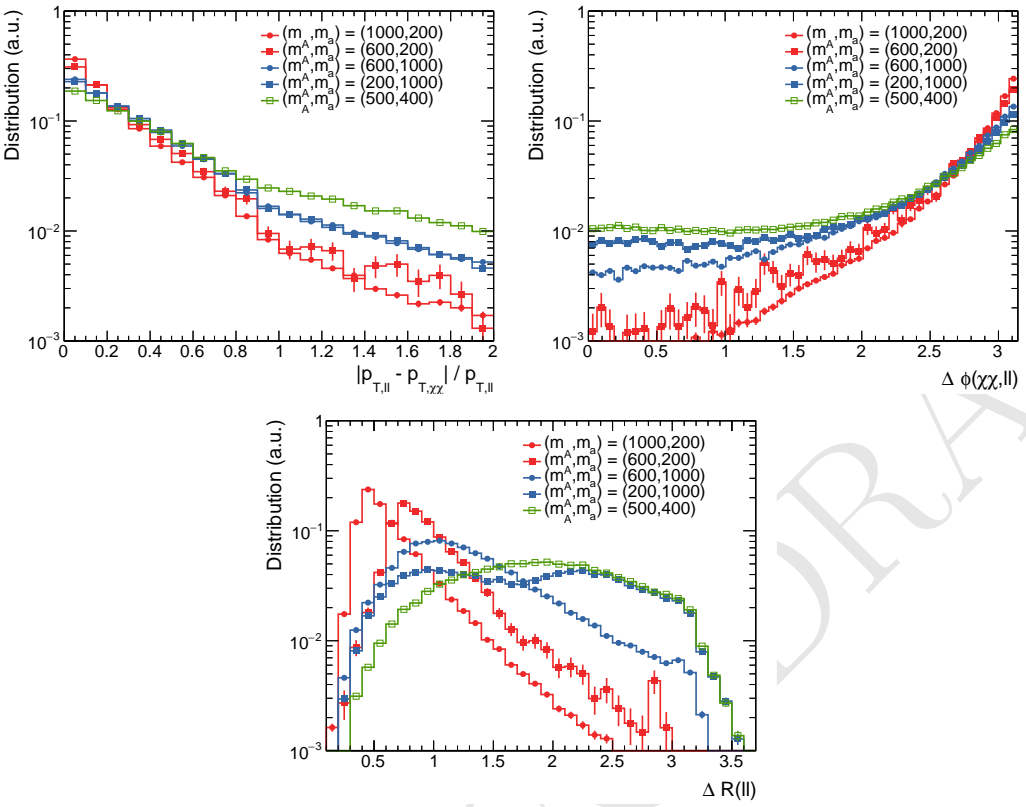


Figure 25: Distributions of the main selection variables after preselection: p_T balance (top panel), $\Delta\Phi$ (middle) and ΔR (bottom). The shown parameter points illustrate the different qualitative behavior in the three different mass regions.

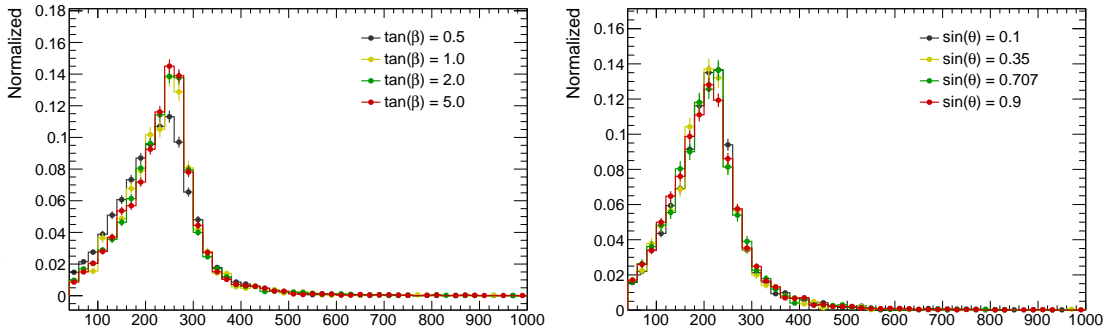


Figure 26: E_T^{miss} distribution after preselection for scans of $\tan\beta$ for fixed $M_A = 600$ GeV and $M_a = 150$ GeV (left) and for $\sin\theta$ for fixed $M_A = 600$ GeV and $M_a = 250$ GeV (right). These parameter have little impact on the event's kinematic distributions, except for small values of $\tan\beta$ where there is a slight softening and broadening of the E_T^{miss} distribution caused by the increased contribution from the top box feynman diagram.

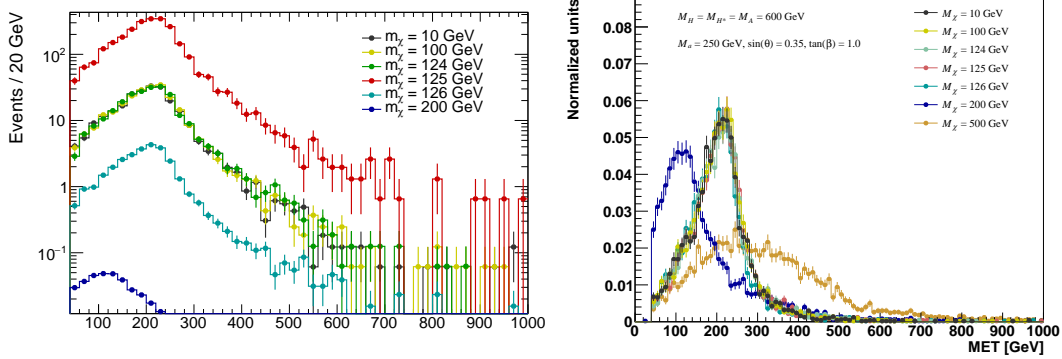


Figure 27: E_T^{miss} distributions following preselection are shown (left) scaled to 40 fb^{-1} and (right) normalized to unity are shown for different values of M_χ with fixed $M_A = 600 \text{ GeV}$ and $M_a = 250 \text{ GeV}$. In the $M_\chi < \frac{M_a}{2}$ region, M_χ has no effect on event yield or E_T^{miss} distribution, at $M_\chi = \frac{M_a}{2}$ a resonant enhancement to the cross section occurs, and in the off-shell region where $M_\chi > \frac{M_a}{2}$ cross section steeply drops. The E_T^{miss} shape remains the same up to, and even slightly above, $M_\chi = \frac{M_a}{2}$, but further off shell the E_T^{miss} distribution becomes increasingly disperse. For $M_\chi = 200 \text{ GeV}$, DM can still decay on-shell through the A . For $M_\chi = 500 \text{ GeV}$ both pseudoscalars are off-shell leading to an event yield too low to fit on the figure on the left and a E_T^{miss} distribution without structure.

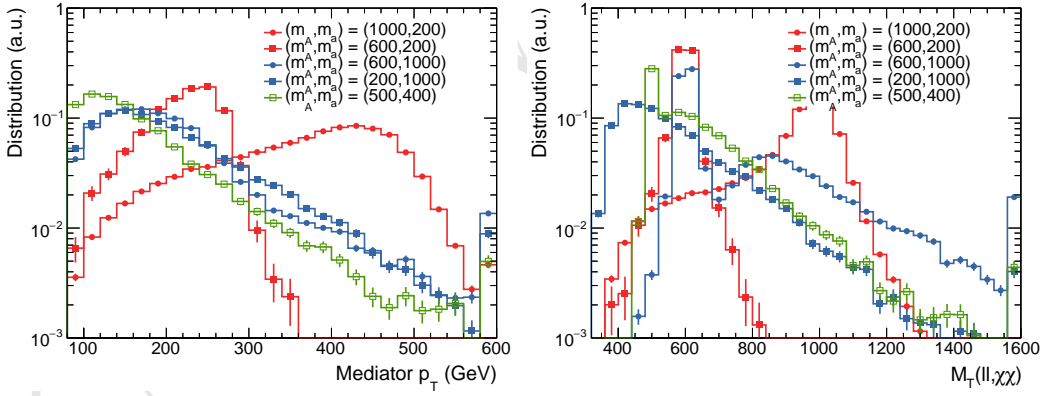


Figure 28: E_T^{miss} and MT distributions in the signal region. The E_T^{miss} distribution shows a Jacobian structure in the $M_A > M_a$ regime, the location of which strongly depends on M_A . In the region of inverted mass hierarchy $M_A < M_a$, the spectrum is less structured and does not fall off as steeply towards higher values. For a small mass splitting of $M_a - M_A \approx M_Z$, the spectrum is shifted to much lower values of E_T^{miss} . The MT distribution allows to access the resonant nature of the process. Clear mass peaks are present for the normal mass hierarchy. In the inverted region, the MT distribution is more sensitive to the mass difference $M_a - M_A$ than the E_T^{miss} distribution, allowing to differentiate between signal hypotheses that give near-identical E_T^{miss} distributions.

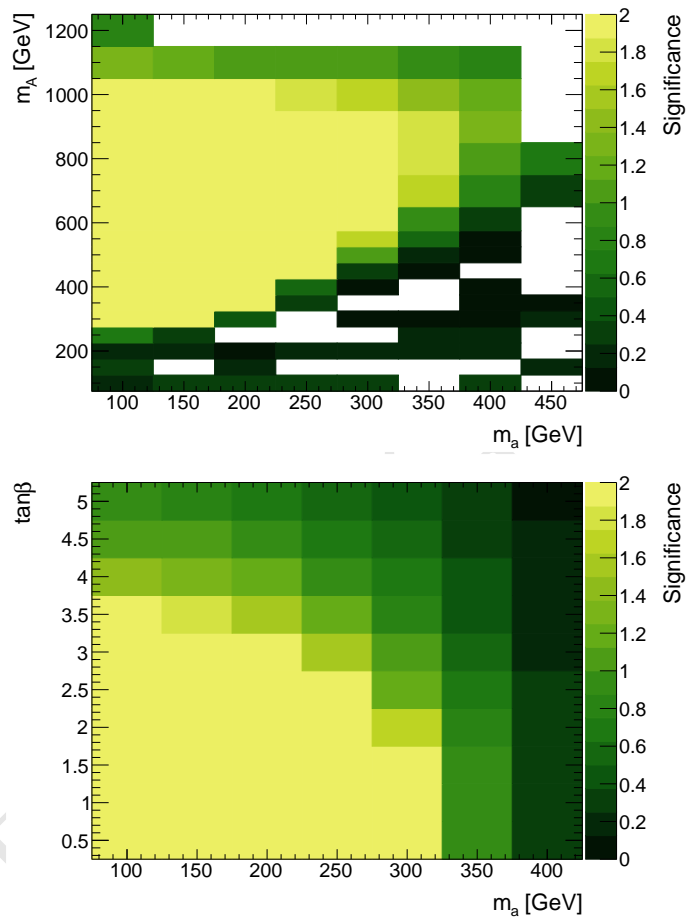


Figure 29: Expected significances are calculated using published background estimates and assuming a reconstruction efficiency of 75%. The ATLAS and CMS experiments are expected to be sensitive to regions with significances greater than 2.

4.2 Studies of the mono-Z (hadronic) signature

The hadronic signature in “mono- Z ” events ($Z \rightarrow q\bar{q}$ events in association with large missing transverse momentum) is considered to be complement to the mono- Z leptonic signature described previously. Potentially the hadronic signature will allow us to probe, compared to the leptonic one, the model parameters involving higher-mass CP-even Higgs boson due to increased branching fraction for the Z decay, while it generally suffers more from larger background in the low mass region. The mono- Z hadronic signature is therefore expected to provide additional sensitivity to the model, possibly extending the reach to a higher mass region.

Technical setup : Simulation of mono- Z hadronic events is performed using a setup similar to that used for the leptonic events. The Madgraph5_aMC@NLO version 2.4.3, interfaced with Pythia version 8.212 for parton showering and the LO NNPDF3.0 with $\alpha_S(M_Z) = 0.130$ for PDF in the matrix element calculations, is used for the event generation. Only gluon-gluon initial states are considered for the production of mono- Z events. In contrast to the leptonic case, the Z -boson is explicitly required in the intermediate state ($g\ g > \text{xd xd} \sim z$) to ensure that non- Z hadronic events are suppressed in the produced sample. The MadSpin is used for the Z decay to maintain a proper spin correlation between the Z decay quarks.

Event selection : For mono- $Z(\rightarrow q\bar{q})$ events intermediated by the exchange of a high-mass CP-even H boson, the Z -boson will be produced with a large transverse momentum and the hadronic decay products of such Z -boson could be merged into a single jet. Such “boosted” event topology is investigated by exploiting the reconstruction technique with a large-radius jet (denoted by J), in addition to more conventional “resolved” event topology where the Z decay products are reconstructed as two separate small-radius jets (denoted by j). The jet reconstruction and the following analysis are all performed at particle level after showering and hadronization implemented in Pythia 8.212 described above.

Two consecutive stages of event selection are considered for the boosted and resolved event topologies:

- Inclusive: minimal kinematic requirements are applied to a pair of small-radius jets (a single large-radius jet) for the resolved (boosted) event topology. The resolved and boosted selection cuts are applied separately, i.e., not sequentially.
- Final selection: cuts are applied to the variables used to define the signal selections. The invariant mass of the pair of small-radius jets or the single large-radius jet is required to be within a window around the Z mass. In addition, selection is applied to the azimuthal angular difference between the $\chi\bar{\chi}$ and the hadronic Z -boson system, $\Delta\Phi(jj \text{ or } J, E_T^{\text{miss}})$, and the magnitude of E_T^{miss} . These final selection cuts are applied sequentially to mimic a realistic analysis; in this study the boosted selection cuts are applied first and then the resolved selection cuts are applied to those events that fail the boosted ones.

The event selection criteria used in the following analysis are listed in Table 4.

Table 4: Event selections used in the analysis for the mono- Z hadronic signature with $Z \rightarrow q\bar{q}$ decays. The requirements are inspired from those used in a typical experimental analysis. The j (J) stands for the small-radius (large-radius) jet in the resolved (boosted) analysis.

Selection stage	Quantity	Requirement
Inclusive resolved and boosted selections	Jet radius	= 0.4 (1.0)
	Jet $ \eta $	< 2.5 (2.0)
	Jet p_T	> 25 GeV (200)
	Number of jets	≥ 2 (1)
Final resolved and boosted selections	$ m_{jj \text{ or } J} - m_Z $	< 15 GeV
	$\Delta\Phi(jj \text{ or } J, E_T^{\text{miss}})$	> 2
	E_T^{miss}	> 100 (250) GeV

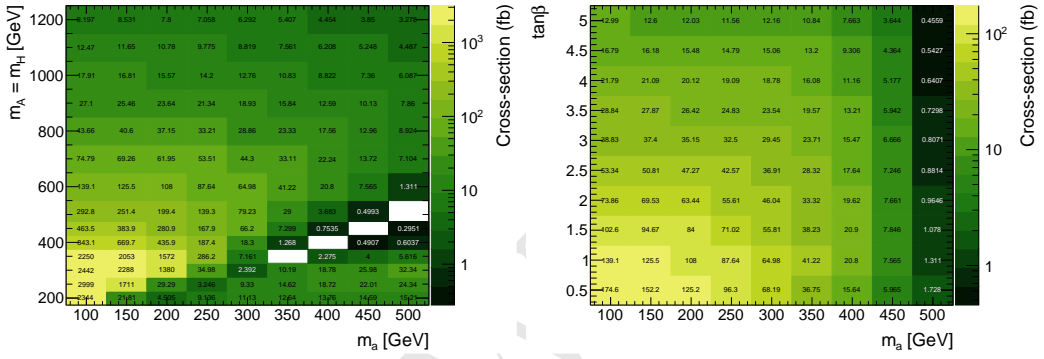


Figure 30: Inclusive cross-sections for the mono- Z hadronic events $pp \rightarrow Z(\rightarrow q\bar{q})\chi\bar{\chi}$ in the M_a vs M_A (left) and M_a vs $\tan\beta$ (right) grids. The $Z \rightarrow q\bar{q}$ branching fraction is not included in the cross-section.

Results : Figure 30 shows the production cross-section for mono- Z events in the M_a (M_A) range between 100 and 500 GeV (200 and 1200 GeV). Shown on the left (right) is the cross-section in the M_a vs M_A (M_a vs $\tan\beta$) grid. Note that the $Z \rightarrow q\bar{q}$ branching fraction is not included in the cross-section. The production cross-section tends to vanish in the region where the M_a gets close to M_A , as shown by the empty points in the grid.

The signal acceptance for the four sets of event selections given in Table 4 is summarized in Fig. 31 in the M_a vs M_A grid. Note again that the resolved and boosted selection criteria are applied separately for the inclusive case, while for the final selections the boosted criteria are applied first and then the resolved ones to those failing the boosted criteria. For the inclusive case, the mass dependence on the acceptance is weak for the resolved criteria while it is rather significant for the boosted criteria as the Z -boson is less boosted with decreasing M_A and hence less likely that the Z -decay products are merged into a single jet. The final boosted selections have acceptance larger than $\sim 20\%$ (40%) at $M_A > 800$ (1000) GeV and $M_a < 400$ GeV. The final resolved selections can recover 10–20% of signal events which fail the boosted criteria in the same mass regions. At $M_A < 600$ GeV

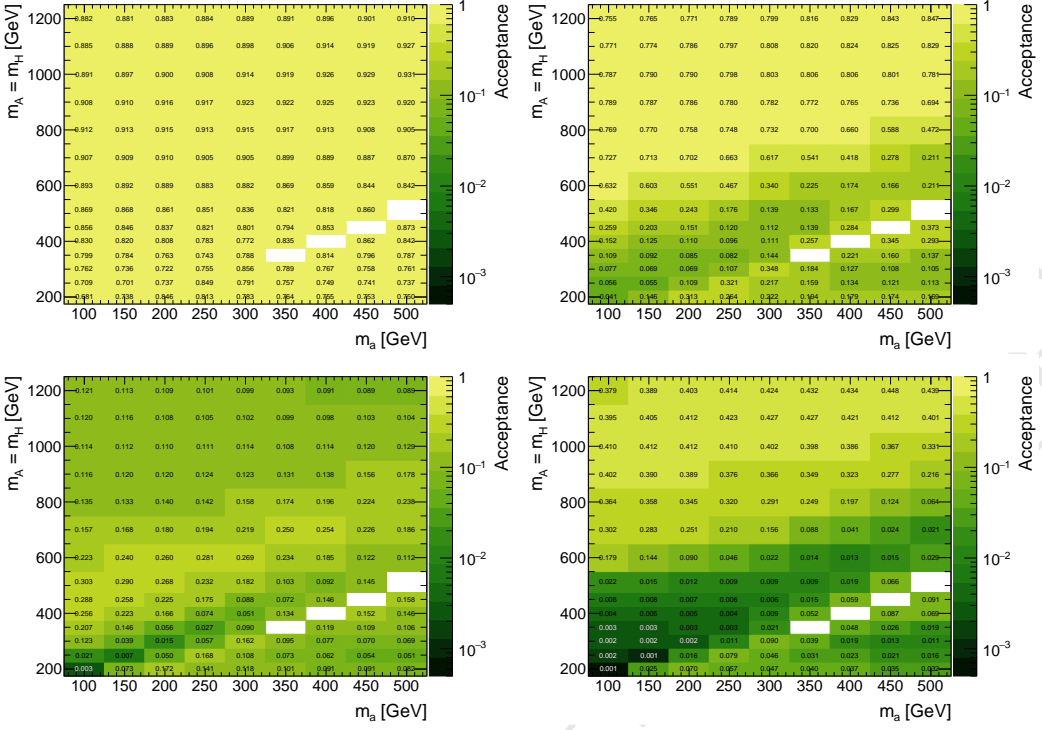


Figure 31: Acceptance for the inclusive (top) and final (bottom) selections for the mono- Z hadronic events $pp \rightarrow Z(\rightarrow q\bar{q})\chi\bar{\chi}$ in the M_a vs M_A grid. Shown on the left (right) is the acceptance for the resolved (boosted) analysis selections.

the signal acceptance is dominated by the resolved selection criteria.

The signal acceptance in the M_a vs $\tan\beta$ space is shown in Fig. 32. The conventions used in Fig. 32 are the same as those in Fig. 31. The signal acceptance is rather independent of $\tan\beta$ except at low $\tan\beta$ region; the acceptance tends to be slightly lower at $\tan\beta < 1$ than at > 1 for $M_a < \sim 250$ GeV while it's opposite for $M_a > \sim 250$ GeV. The acceptance decreases with increasing M_a because the E_T^{miss} spectrum becomes softer with M_a , as shown in Fig. 34.

Figure 33 shows the kinematic distributions of mono- Z events after applying the inclusive selections, separately for the resolved and boosted topologies. The M_a is fixed to 250 GeV and the M_A is chosen to be 300, 600, 900 and 1200 GeV in the figure. When the M_A gets closer to M_a , the Z -boson is less boosted, causing the large-radius jet mass to be more populated at mass below ~ 30 GeV. When the $|M_A - M_a|$ becomes smaller than the Z -boson mass, the non-resonant production dominates as clearly seen in the E_T^{miss} spectrum for the resolved case. Figure 34 shows the same set of distributions when the M_A is fixed to 600 GeV and the M_a varies from 150 to 250, 350 and 450 GeV. The trend seen in Fig. 33 is also visible here when the M_a gets closer to M_A .

The sensitivity of the resolved, boosted and the combined analysis selections to the mono- Z hadronic signature is examined. The main background for this signature is $Z \rightarrow \nu\nu$ events in association with jets. The sample of $Z(\rightarrow \nu\nu) + \text{jets}$ events is produced using

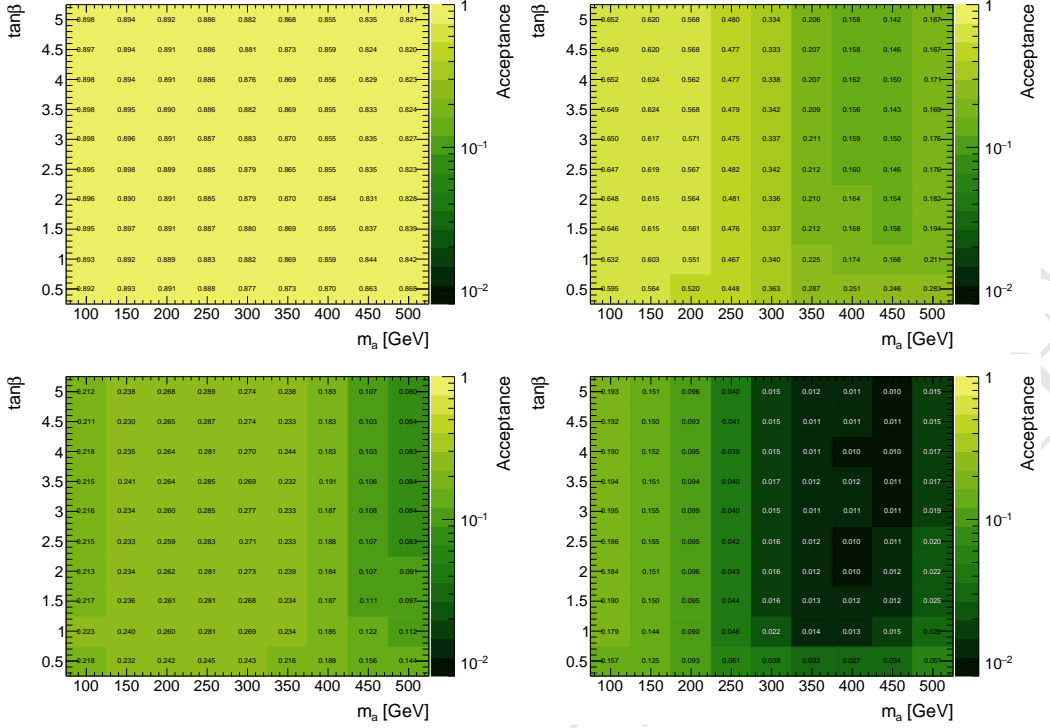


Figure 32: Acceptance for the inclusive (top) and final (bottom) selections for the mono- Z hadronic events $pp \rightarrow Z(\rightarrow q\bar{q})\chi\bar{\chi}$ in the M_a vs $\tan\beta$ grid. Shown on the left (right) is the acceptance for the resolved (boosted) analysis selections. The M_A is fixed to 600 GeV.

Sherpa 2.2.1 and the matrix elements are calculated up to 2 partons at next-to-leading order and up to 4 partons at leading order. The $Z(\rightarrow \nu\nu)+\text{jets}$ events are analyzed at particle level with the same criteria used for the signal. The number of $Z \rightarrow \nu\nu$ events after applying the cuts is increased by a factor 2 to account for the contribution from other backgrounds. This factor is chosen from the ATLAS dark matter search in the mono- Z hadronic signature using 3.2 fb^{-1} of 13 TeV data, published in Ref. ???. The sensitivity is defined in this study as

$$\text{Significance} = \sqrt{\sum_{\text{bin}} Z_{\text{bin}}^2} \quad (4.7)$$

where the per-bin significance, Z_{bin} , is obtained, using asymptotic calculation of the Poisson likelihood ratio statistic, to be

$$Z_{\text{bin}} = \left[2 \left((s+b) \ln \left[\frac{(s+b)(b+\sigma_b^2)}{b^2 + (s+b)\sigma_b^2} \right] - \frac{b^2}{\sigma_b^2} \ln \left[1 + \frac{\sigma_b^2 s}{b(b+\sigma_b^2)} \right] \right) \right]^{1/2} \quad (4.8)$$

with the assumption of 10% background uncertainty in each E_T^{miss} bin. The sum in Eq.(4.7) is taken over all E_T^{miss} bins after applying the final selections. The results are shown in Fig. 35 for the resolved only, boosted only and the combined resolved+boosted analysis selections, corresponding to the integrated luminosity of 40 fb^{-1} at $\sqrt{s} = 13 \text{ TeV}$. The significance depends strongly on the assumption of background uncertainty since a large

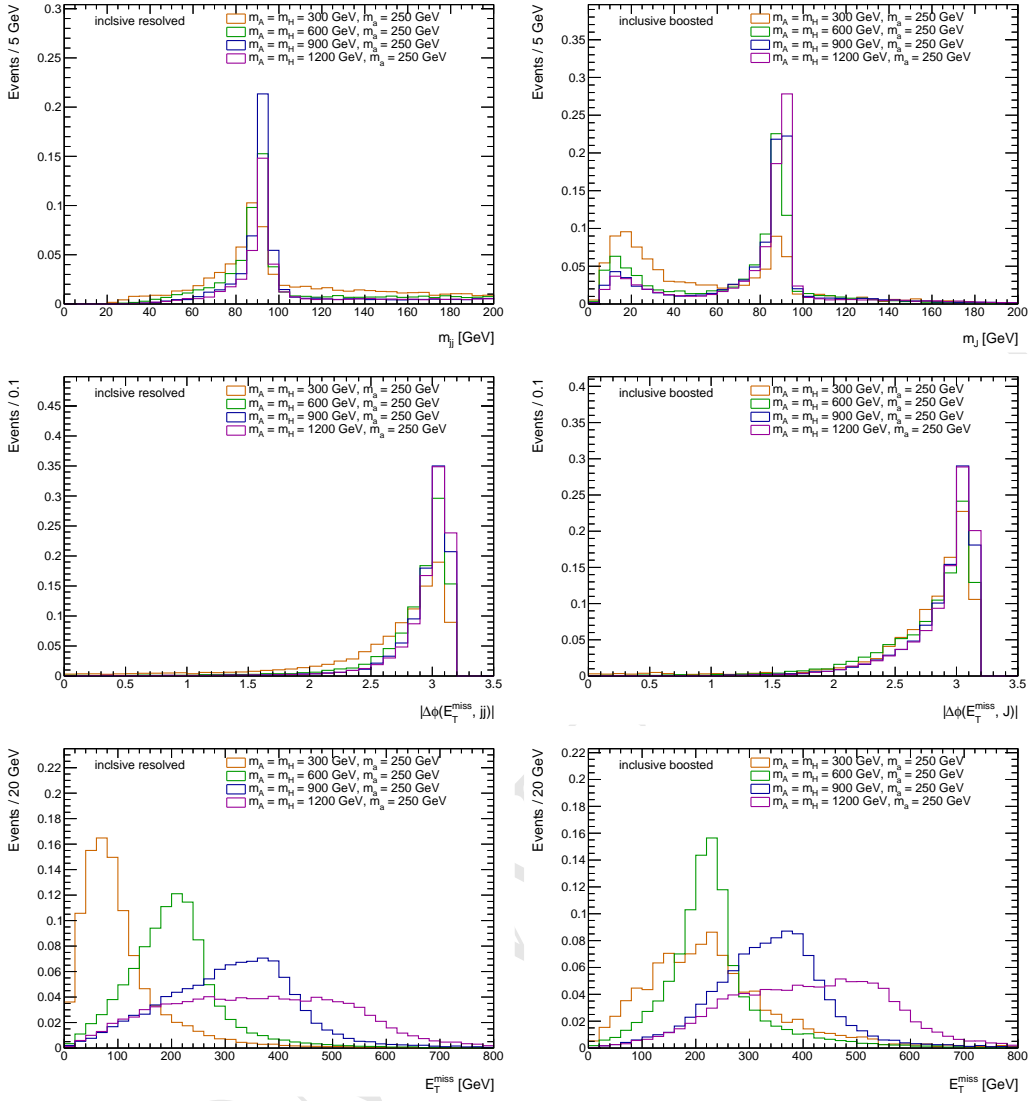


Figure 33: Dijet mass (top), $\Delta\Phi(jj, E_T^{\text{miss}})$ (middle) and E_T^{miss} (bottom) distributions after applying the inclusive selections in the resolved analysis are shown on the left side. Large-radius jet mass (top), $\Delta\Phi(J, E_T^{\text{miss}})$ (middle) and E_T^{miss} (bottom) distributions after applying the inclusive selections in the boosted analysis are shown on the right side. The signal masses are chosen to be $M_A = 300, 600, 900$ and 1200 GeV with the fixed $M_a = 250$ GeV.

number of background events remain in this simple analysis with a minimum set of selection criteria. More realistic analysis performed in LHC experiments is expected to improve the sensitivity.

4.2.1 Studies of DM+heavy flavor signature

Heavy flavour final state have sizeable contributions to the production of the CP-even and CP-odd scalar mass eigenstates, due to the Yukawa structure of the couplings in the matter

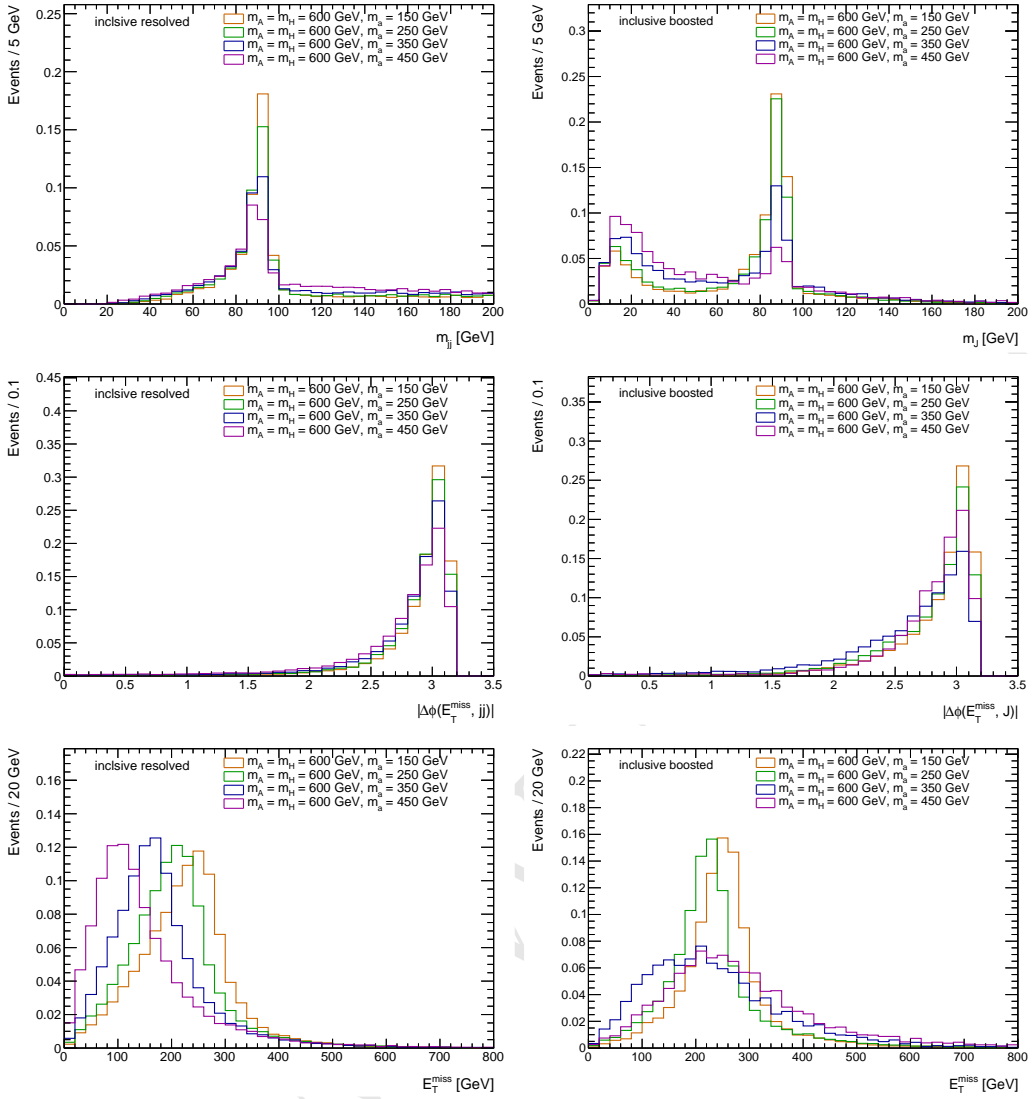


Figure 34: Dijet mass (top), $\Delta\Phi(jj, E_T^{\text{miss}})$ (middle) and E_T^{miss} (bottom) distributions after applying the inclusive selections in the resolved analysis are shown on the left side. Large-radius jet mass (top), $\Delta\Phi(J, E_T^{\text{miss}})$ (middle) and E_T^{miss} (bottom) distributions after applying the inclusive selections in the boosted analysis are shown on the right side. The signal masses are chosen to be $M_a = 150, 250, 350$ and 450 GeV with the fixed $M_A = 600 \text{ GeV}$.

sector. In the following sections, the most important signatures involving either visible or invisible decays of the heavy Higgses are reviewed.

4.2.2 Scanning the parameter space

Scan of $\tan\beta$ and $\sin\theta$: In the limit of small $\tan\beta$ values, the couplings of h_3 (A) and h_4 (a) to down-type quarks are heavily suppressed irrespectively of the Yukawa assignment. At LO, $t\bar{t} + \chi\bar{\chi}$ associated production is mediated through either CP-odd weak eigenstate,

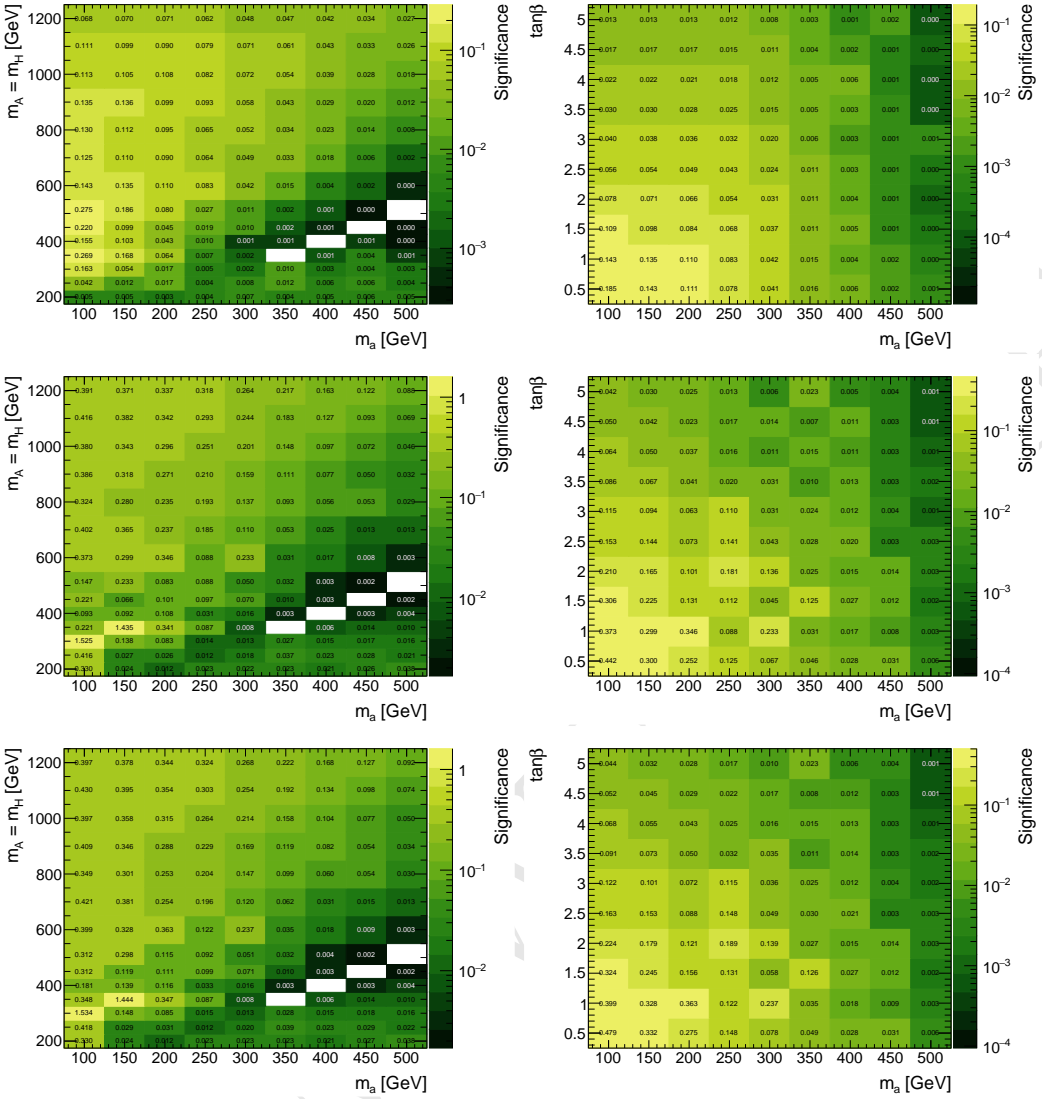


Figure 35: Significance (as defined in the text) for the mono- Z hadronic events $pp \rightarrow Z(\rightarrow q\bar{q})\chi\bar{\chi}$ in the M_a vs M_A (left) and M_a vs $\tan\beta$ (right) grids. Shown at the top, middle and bottom are the resolved only, boosted only and the combined resolved+boosted analysis, respectively.

A or a , though it is shown in Fig. 36 that $a \rightarrow \chi\bar{\chi}$ is the dominant production mode. Although the relative mediator contribution is dependent on $\tan\beta$, observables such as E_T^{miss} and top quark p_T do not have a kinematic dependence on $\tan\beta$ as demonstrated in Fig. 37.

Mixing of the CP-odd weak eigenstates is achieved through the mixing angle, θ . As shown in Fig. 38, the A and a mass peaks are quite narrow for values where $\sin\theta$ approaches 1, and $a \rightarrow \chi\bar{\chi}$ is the dominant $\chi\bar{\chi}$ production mode. However, no kinematic dependence on $\sin\theta$ is observed in the E_T^{miss} and top quark p_T as shown in Fig. 39.

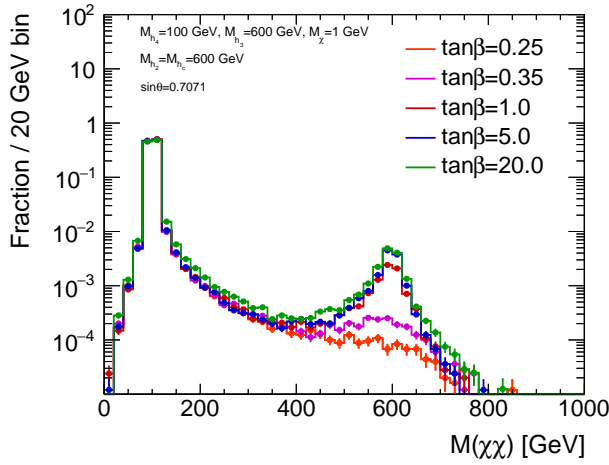


Figure 36: The mass distribution of the $\chi\bar{\chi}$ system for various values of $\tan\beta$, with $M_a = 100$ GeV, $M_A = 600$ GeV, $M_H = M_{H^\pm} = 600$ GeV, and $\sin\theta = 0.7071$.

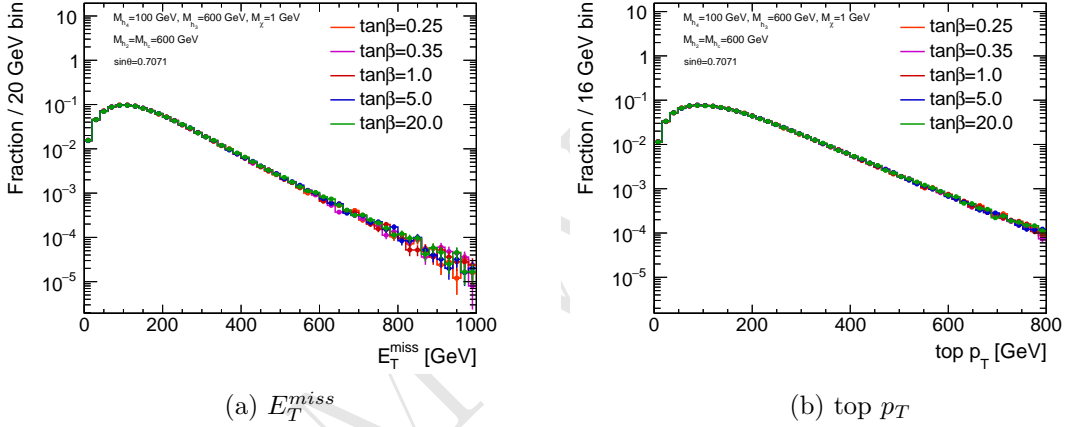


Figure 37: The E_T^{miss} and top p_T distribution for inclusive $t\bar{t} + \chi\bar{\chi}$ production for various values of $\tan\beta$, with $M_a = 100$ GeV, $M_A = 600$ GeV, $M_H = M_{H^\pm} = 600$ GeV, and $\sin\theta = 0.7071$.

Scan of M_a and M_A : While the relevant kinematic distributions display no dependence on the aforementioned mixing angles, the same does not hold true for the masses, M_a and M_A . As shown in Fig. 40, the E_T^{miss} , and leading and trailing top quark p_T distributions broaden with increasing M_a . Similarly, for values of $M_A < M_a$, as M_A increases, the kinematic distributions mentioned above also broaden, as shown in Fig. 41.

4.2.3 Comparison with DMsimp Pseudoscalar Model

To date, simplified models of DM (DMsimp) are used to interpret Run II CMS and ATLAS HF+DM searches. A comparison of the pertinent kinematic distributions between the pseudoscalar simplified model and the 2HDM+a model for the same value of M_a are shown

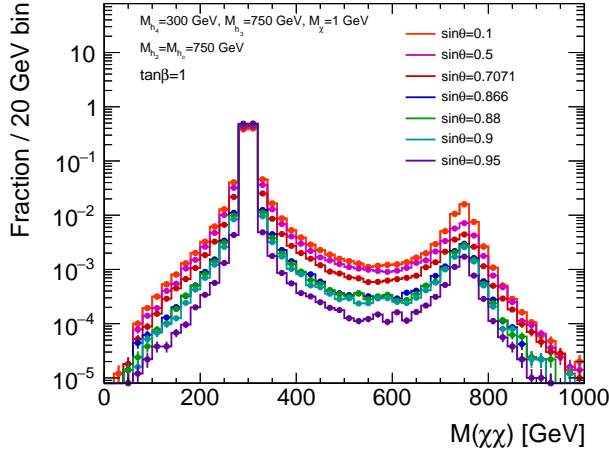


Figure 38: The mass distribution of the $\chi\bar{\chi}$ system for various values of $\sin \theta$, with $M_a = 300$ GeV, $M_A = 750$ GeV, $M_H = M_{H^\pm} = 750$ GeV, and $\tan \beta = 1$.

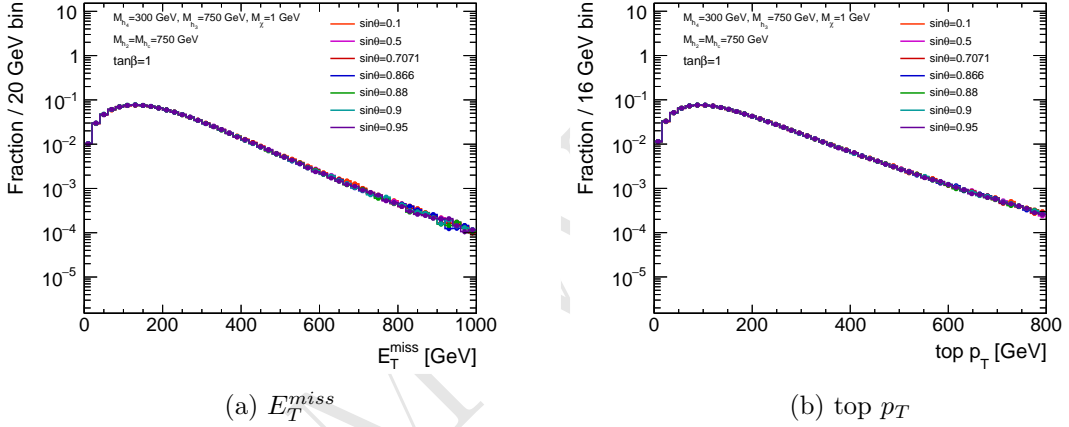


Figure 39: The E_T^{miss} and top p_T distribution for inclusive $t\bar{t} + \chi\bar{\chi}$ production for various values of $\sin \theta$, with $M_a = 300$ GeV, $M_A = 750$ GeV, $M_H = M_{H^\pm} = 750$ GeV, and $\tan \beta = 1$.

in Fig. ???. The kinematics of the pseudoscalar **DMsimp** model with $M_a = 100$ GeV map directly onto those of the 2HDM+a model with $M_a = 100$ GeV, $M_A = 600$ GeV, $M_H = M_{H^\pm} = 600$ GeV, $\sin \theta = 0.7071$, and $\tan \beta = 1$. From the mass distribution of the $\chi\bar{\chi}$ shown in Fig. 43, it is evident that the 2HDM+a model contains contributions from both the light and heavy pseudoscalar mediator as in the **DMsimp** model.

In Fig. 44, relevant kinematic distributions, commonly employed in HF+DM searches, are mapped from the **DMsimp** pseudoscalar models to the 2HDM+a model, with the mediator masses corresponding to the additional light pseudoscalar in the latter model. The dashed distributions represent the **DMsimp** model, while the solid are the 2HDM+a model distributions. The $t\bar{t} + \chi\bar{\chi}$ process was generated at LO precision using both models. As can be seen, the kinematics do not change appreciably between the models generated at

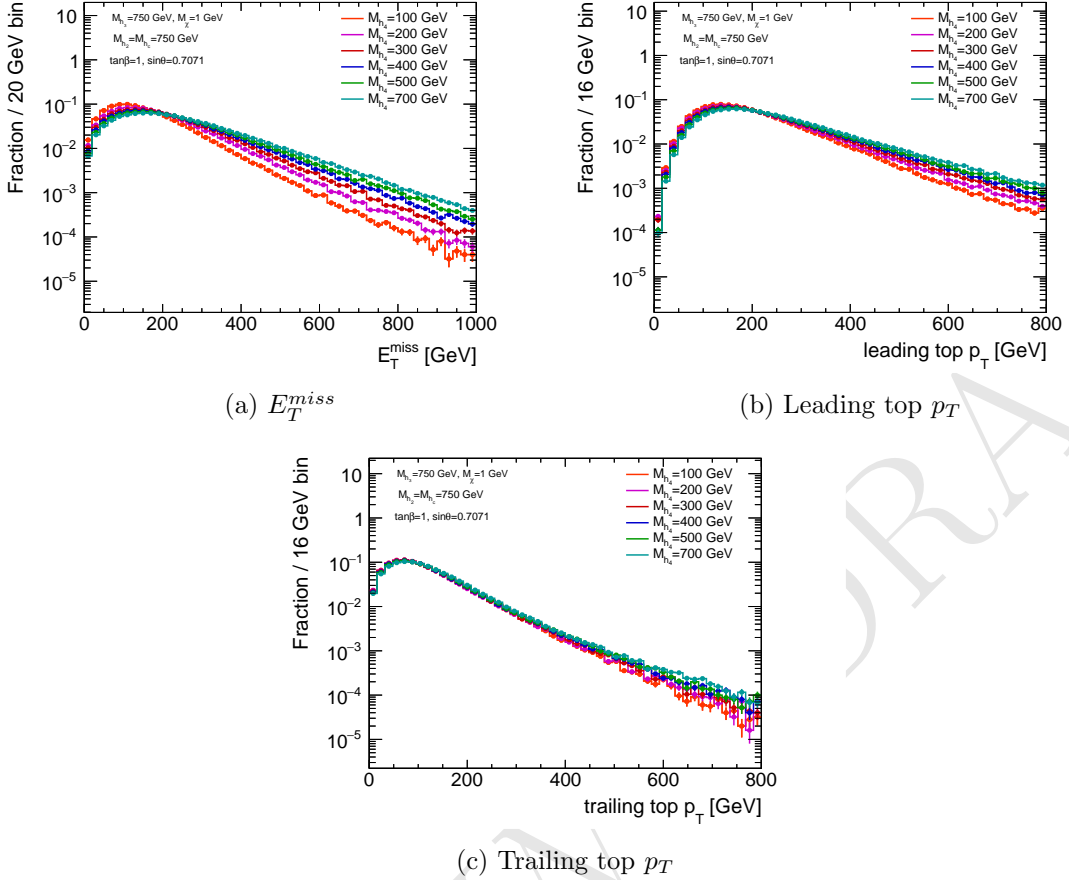


Figure 40: The E_T^{miss} , leading and trailing top p_T distributions for inclusive $t\bar{t} + \chi\bar{\chi}$ production for various values of M_a , with $M_A = 750$ GeV, $M_H = M_{H^\pm} = 750$ GeV, $\tan\beta = 1$, and $\sin\theta = 0.7071$.

the same value of M_a . A discussion on cross-section rescaling procedures can be found in the following section.

4.2.4 Recasting existing $tt + E_T^{miss}$ and $bb + E_T^{miss}$ signatures

These two signatures are dominantly produced in diagrams involving the invisible decays of the two CP-odd scalars. Their relevance is therefore determined by the two pseudoscalar masses, $m(A)$ and $m(a)$ and it is a function of $\sin\theta$ and $\tan\beta$. For both bb and tt associated productions, we find that the highest sensitivity of this signatures is obtained for high values of $\sin\theta$.

The 2HDM+a model is equivalent to a single pseudoscalar simplified model (DMF) when A is much heavier than a , and therefore the former does not contribute to the considered final state. However, when the two mediators are closer in mass, the $pp \rightarrow ttA$ contribution becomes more relevant as it is possible to observe in Figure 45, where the two models are compared assuming $m(A) = 750$ GeV and two different values for $m(a)$. An excellent agreement was observed between *DMSIMP* and *2HDMp* on parton-

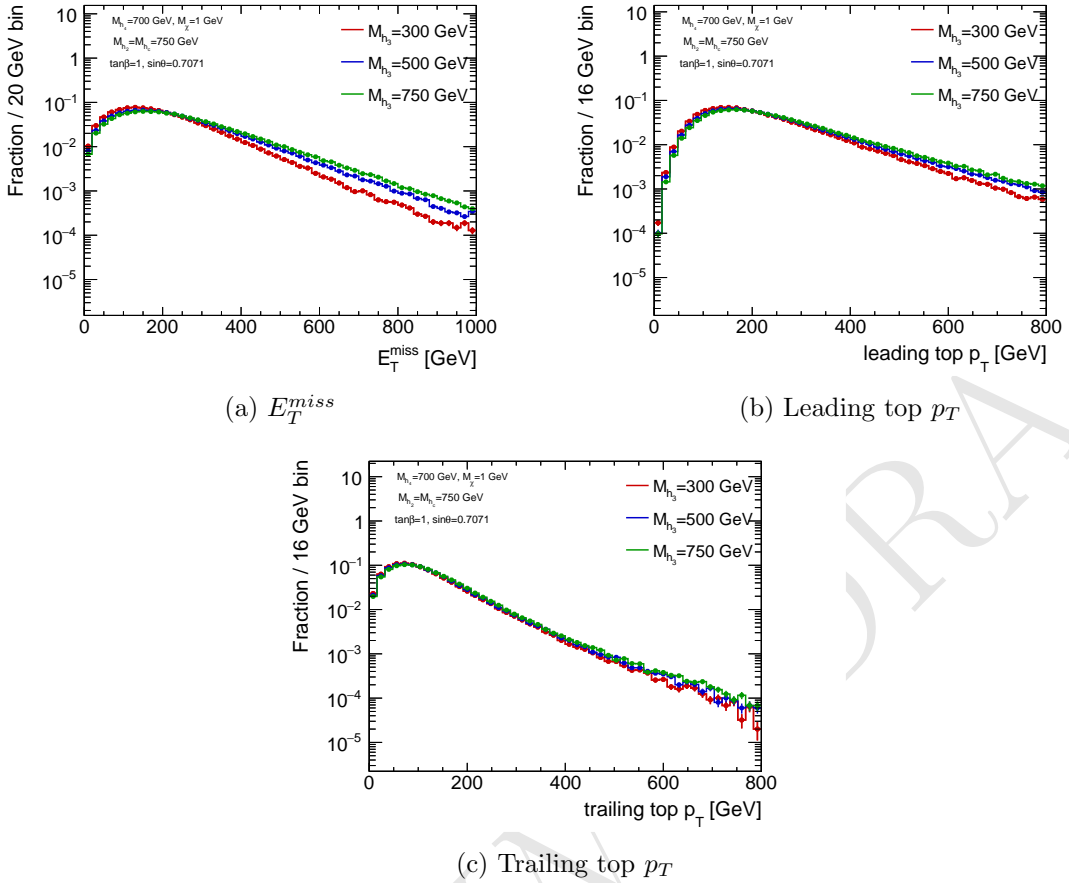


Figure 41: The E_T^{miss} , leading and trailing top p_T distributions for inclusive $t\bar{t} + \chi\bar{\chi}$ production for various values of M_A , with $M_a = 700 \text{ GeV}$, $M_H = M_{H^\pm} = 750 \text{ GeV}$, $\tan\beta = 1$, and $\sin\theta = 0.7071$.

level variables sensitive to the helicity structure of the interaction between top and the mediator[?], if the invariant mass of the two DM particles in the 2HDM is required to be smaller than $200(300)$ GeV for $m(a) = 150(300)$ GeV respectively, giving confidence that, once the contribution from A production is separated, it is possible to fully map the $2HDM + a$ kinematics into the DMF simplified model.

This remapping is achieved by taking for each set of the parameters the average of the selection acceptances for $m(A)$ and $M(A)$ as calculated with *DMSIMP* weighted by the respective cross-section for A (σ_A) and a (σ_a) production, in formulas

$$Acc_{2HDM}(m(A), M(a)) = \frac{\sigma_a \times Acc_{DMSIMP}(m(a)) + \sigma_A \times Acc_{DMSIMP}(m(A))}{\sigma_a + \sigma_A} \quad (4.9)$$

The acceptance in this case is a parton level implementation of the two-lepton analysis described in [arXiv:1710.11412]. The acceptance estimated in this way is shown as red triangles in Figure 46, and an excellent agreement can be seen with the acceptances evaluated directly on the 2HDM samples. The acceptance estimated in this way is shown as red tri-

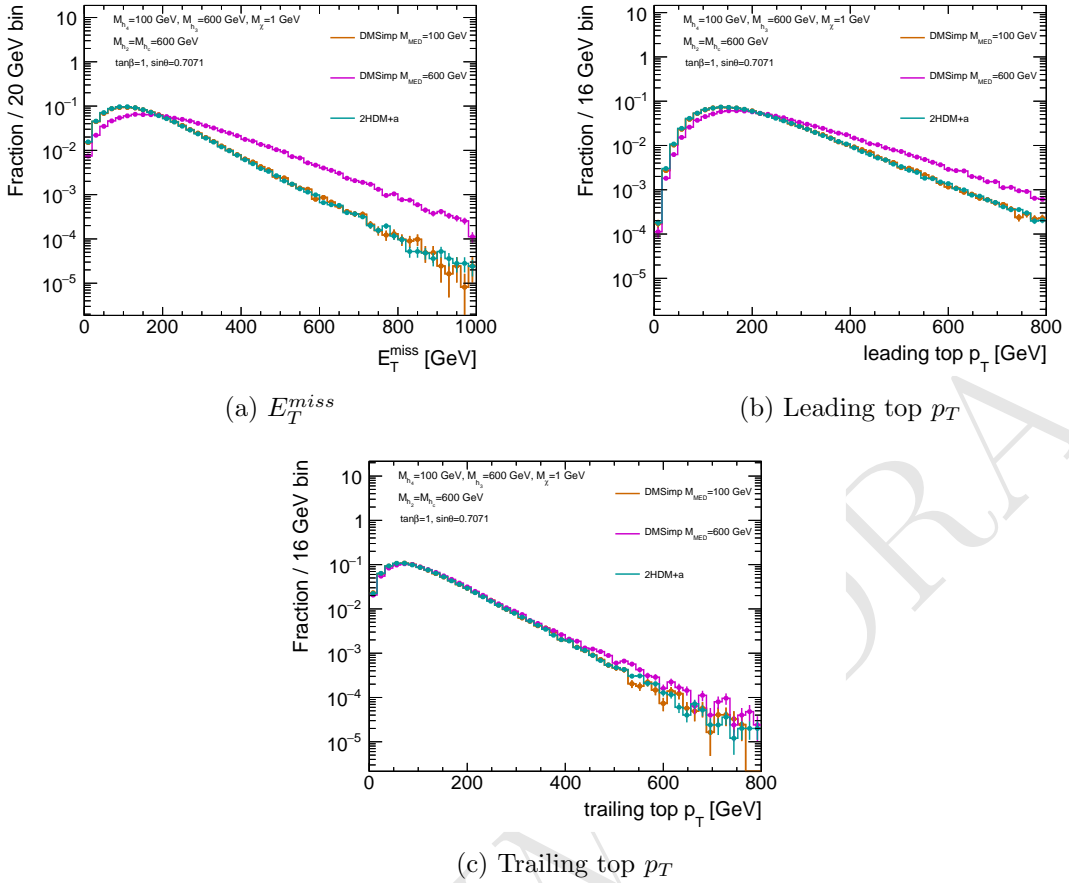


Figure 42: The E_T^{miss} , leading and trailing top p_T distributions for inclusive $t\bar{t} + \chi\bar{\chi}$ production for various values of M_A , with $M_a = 700$ GeV, $M_H = M_{H^\pm} = 750$ GeV, $\tan\beta = 1$, and $\sin\theta = 0.7071$.

angles in Figure 46, and an excellent agreement can be seen with the acceptances evaluated directly on the 2HDM samples. Further validation were performed also on the acceptances calculated for zero and one lepton final states [1710.11412, 1711.11520], both as a function of $\sin\theta$ and $\tan\beta$ and can be observed in Fig 47. Finally, the formula was successfully tested also the situation in which $|m(A) - m(a)| \sim 50$ GeV, implying the possibility of a large interference between the production of the two bosons.

4.2.5 Flavour scheme recommendations and studies

The relevant kinematic distributions for $t\bar{t} + \chi\bar{\chi}$ associated production in the context of this model are shown to be independent from the choice of PDF flavour scheme. In Figures 48–50, the E_T^{miss} , which is taken to be the p_T of the $\chi\bar{\chi}$ system, and the p_T distribution of the top quarks is presented using the 4 and 5-flavour scheme. The 4-flavour LHAPDF ID is 263400 and corresponds to `NNPDF30_lo_as_0130_nf_4`, and the 5-flavour LHAPDF ID is 263000 and corresponds to `NNPDF30_lo_as_0130`. As demonstrated for various configurations of the 2HDM+a model parameters, the kinematics are not affected by the flavour

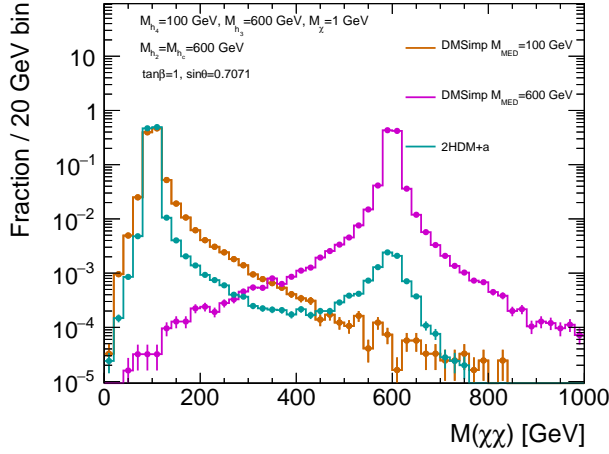


Figure 43: The mass distribution of the $\chi\bar{\chi}$ system for DMsimp pseudoscalar models with $M_a = 100$ GeV and $M_a = 600$ GeV, compared with 2HDM+a with $M_a = 100$ GeV, $M_A = 600$ GeV, $M_H = M_{H^\pm} = 600$ GeV, $\sin \theta = 0.7071$ and $\tan \beta = 1$.

scheme choice of PDF. Furthermore, the difference in cross-section between the 4-flavour and 5-flavour generated LO $t\bar{t} + \chi\bar{\chi}$ process is at the 2 – 3% level, as noted in Tab. 5.

Despite the lack of kinematic dependence on flavour scheme, it is recommended to use the 5-flavour PDF.[Add support/discussion and references](#)

M_{h_2}, M_{h_c} [GeV]	M_{h_3} [GeV]	M_{h_4} [GeV]	$\sin \theta$	$\tan \beta$	4F σ (pb)	5F σ (pb)
750	500	100	0.7071	1	0.0988596	0.0964933
750	750	200	0.7071	1	0.0445115	0.043149
750	300	200	0.25	1	0.0310152	0.0300196

Table 5: Configurations of the 2HDM+a model used to generate the $t\bar{t} + \chi\bar{\chi}$ process at LO and the corresponding cross-sections from the 4-flavour (4F) and 5-flavour (5F) PDF.

Motivations for an high $\tan\beta$ scan for $bb+E_T^{\text{miss}}$ The projection of sensitivity in $\tan\beta$ for benchmark #2, based on the CMS results for $bb+MET$ [arXiv:1706.02581] are shown in Figure 51. The reach for an upper bound on $\tan(\beta)$ with $bb+MET$ shows good potential, for $\tan\beta$ values above 10.

Say something about high width for H?

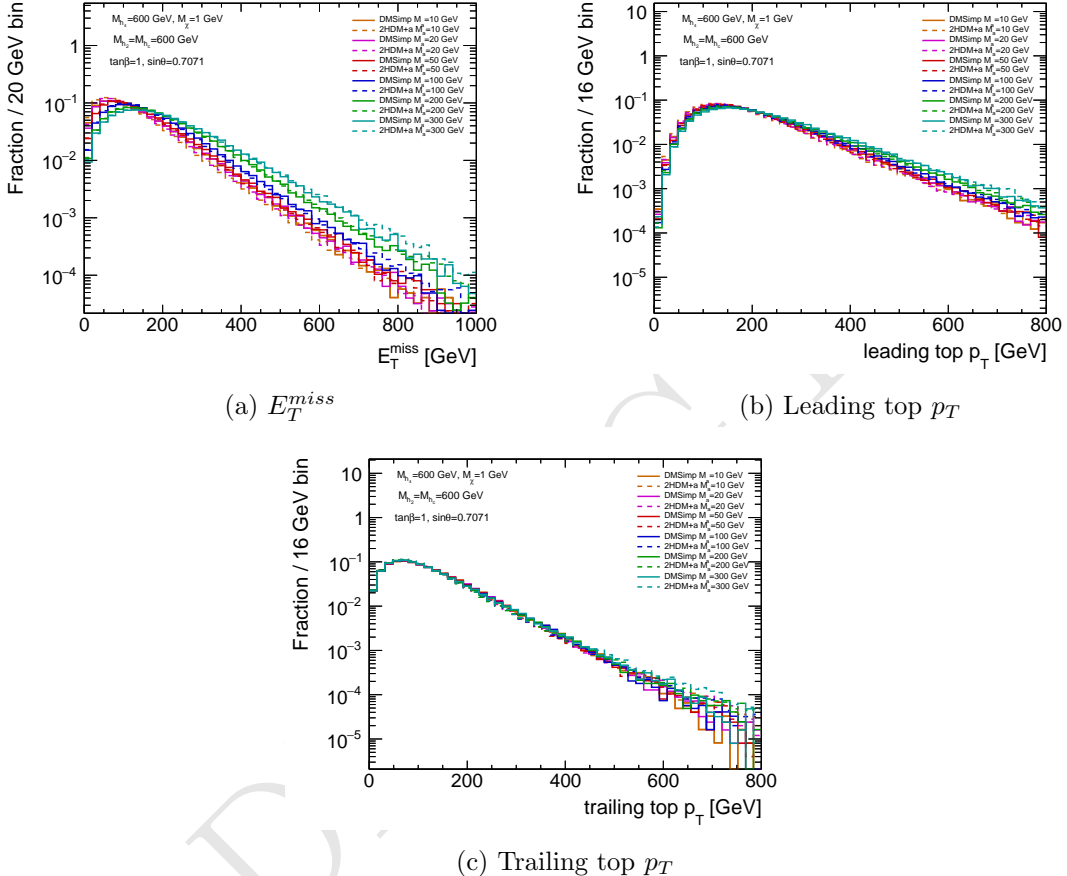


Figure 44: The E_T^{miss} , leading and trailing top p_T distributions for inclusive $t\bar{t} + \chi\bar{\chi}$ production generated from the **DMsimp** (solid) and the **2HDM+a** (dashed) models with various values of M_a . The **2HDM+a** models are generated with the following model parameters: $M_A = 600 \text{ GeV}$, $M_H = M_{H^\pm} = 600 \text{ GeV}$, $\tan\beta = 1$, and $\sin\theta = 0.7071$.

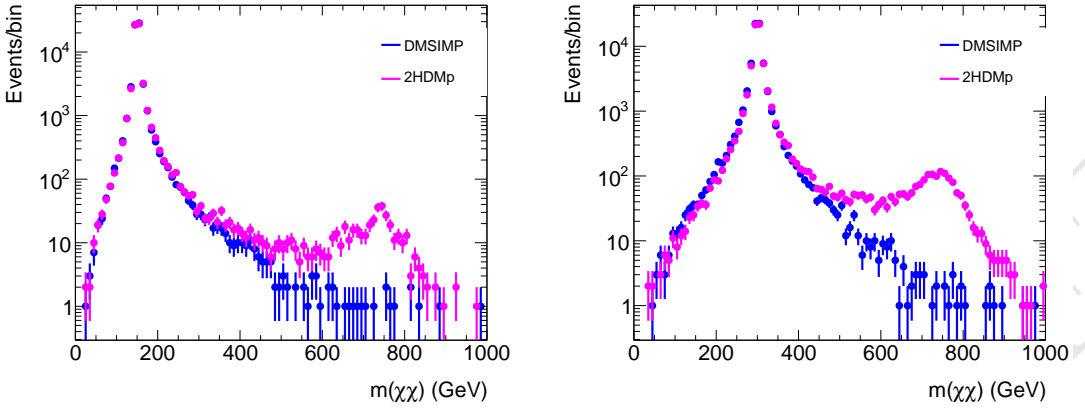


Figure 45: Comparison of $m(\chi\chi)$, the invariant mass of the two DM particles for the *DMSIMP* (blue) and the *2HDMp* model (magenta). The plot on the left (right) shows the comparison for $m(a) = 150(300)$ GeV respectively.

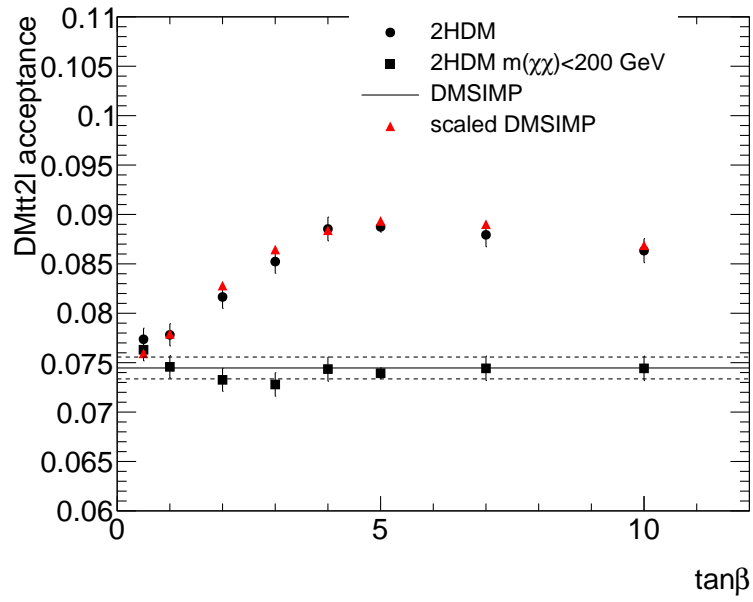


Figure 46: Acceptance of the two-lepton analysis as a function of $\tan \beta$ for the *2HDMp* model (round markers), for the *2HDMp* model considering only events with $m(\chi\chi) < 200$ GeV (square markers), and for the *DMSIMP* model (full line) for a mediator mass of 150 GeV. The two dashed lines indicate the statistical error of the *DMSIMP*. The value of $m(A)$ is fixed at 600 GeV, and $\sin \theta = 0.35$. The acceptance calculated from the *DMSIMP* acceptance rescaled following the prescription 4.9 (red triangles) is also shown.

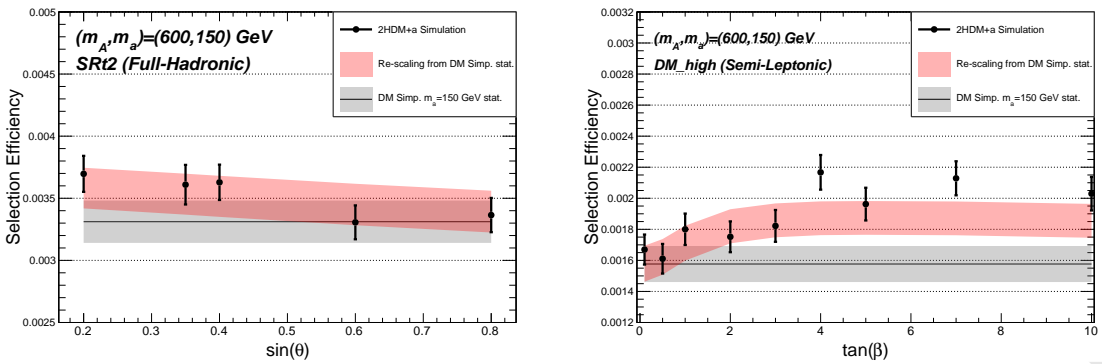


Figure 47: Validation of the re-scaling formula on zero and one lepton final states as a function of $\tan\beta$ and $\sin\theta$ parameters

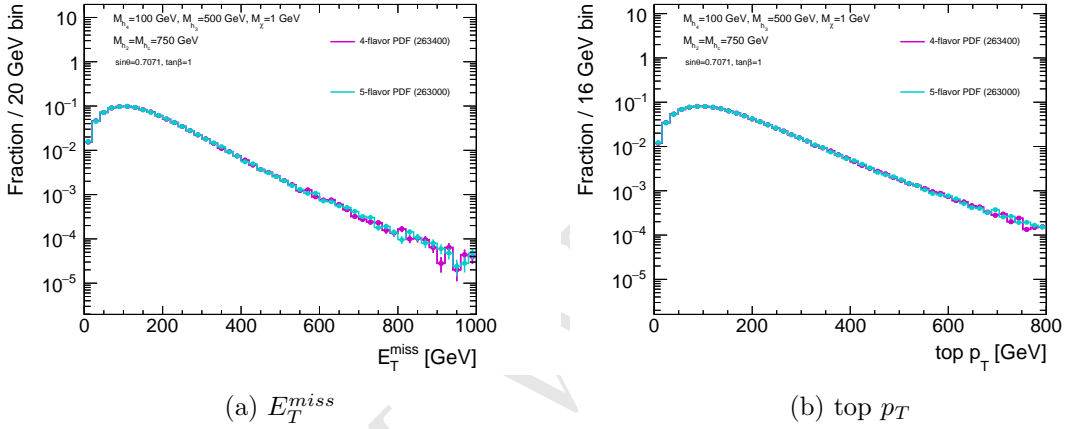


Figure 48: E_T^{miss} and top p_T distributions for $M_{h_4} = 100$ GeV, $M_{h_3} = 500$ GeV, $M_{DM} = 1$ GeV, $\sin\theta = 0.7071$, and $\tan\beta = 1$.

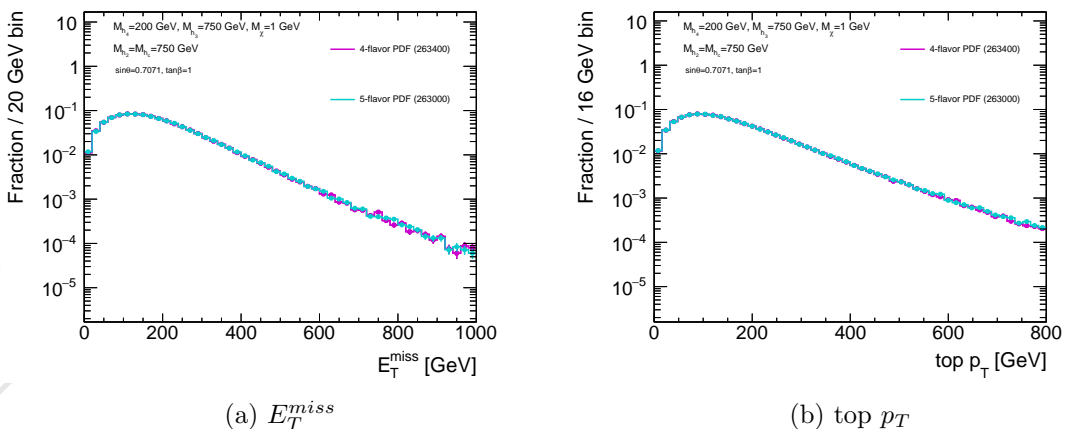


Figure 49: E_T^{miss} and top p_T distributions for $M_{h_4} = 200$ GeV, $M_{h_3} = 750$ GeV, $M_{DM} = 1$ GeV, $\sin\theta = 0.7071$, and $\tan\beta = 1$.

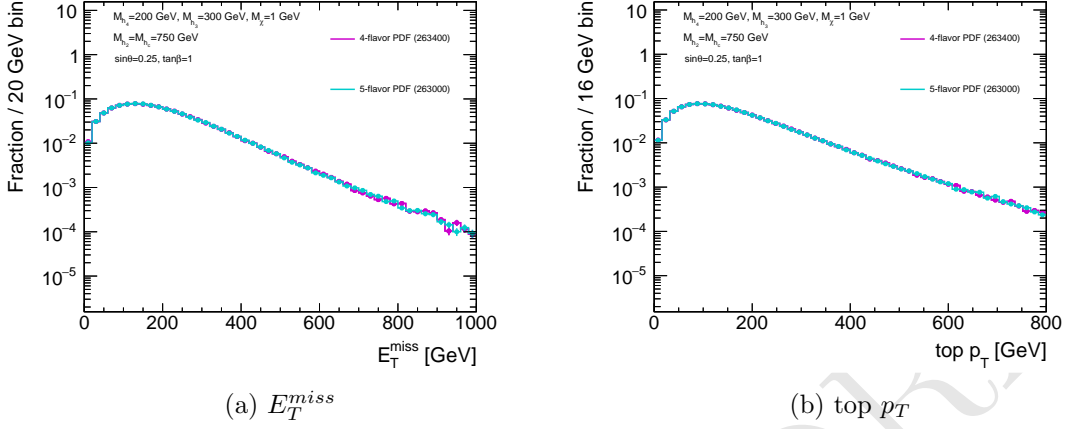


Figure 50: E_T^{miss} and top p_T distributions for $M_{h_4} = 200$ GeV, $M_{h_3} = 300$ GeV, $M_{DM} = 1$ GeV, $\sin\theta = 0.25$, and $\tan\beta = 1$.

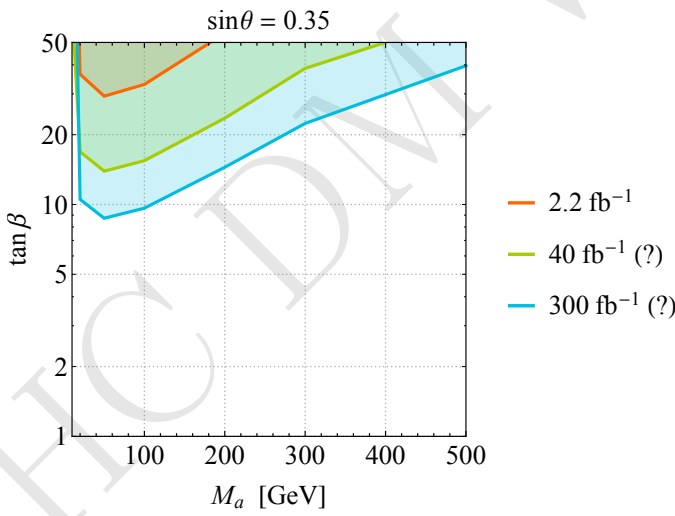


Figure 51: Sensitivity projection for benchmark #2 based on the CMS results for bb+MET [arXiv:1706.02581].

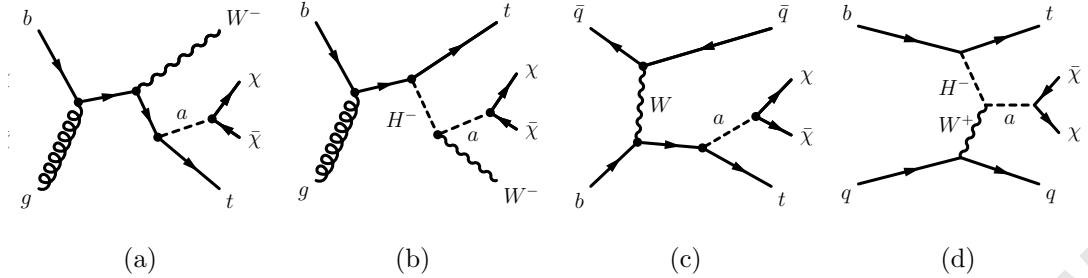


Figure 52: Representative diagrams for tW and t -channel production of DM in association with a single top quark.

4.2.6 Motivation for a dedicated $tW + E_T^{\text{miss}}$ search

The sensitivity of the LHC experiments to the associated production of dark matter with a single top has been recently studied [?] in the framework of an extension of the standard model featuring two Higgs doublets and an additional pseudoscalar mediator. This study extends the work of previous literature [?], which demonstrated using a simplified model that the consideration of final states involving a single top quark and DM (DMt) increases the coverage of existing analyses targeting the $DMt\bar{t}$ process.

Like single top production within the SM, the DMt signature in the model receives three different types of contributions at leading order (LO) in QCD. These are t -channel production, s -channel production and associated production together with a W boson (tW) (Fig. 52). When the decay $H^\pm \rightarrow W^\pm a$ is possible, the H^\pm is produced on-shell, and the cross-section of $pp \rightarrow tW\chi\chi$, assuming H^\pm masses of a few hundred GeV, is around one order of magnitude larger than the one for the same process in the simplified model. Moreover the production and cascade decay of a resonance yields kinematic signatures which can be exploited to separate the signal from the SM background.

Dedicated selections considering one and two lepton final states are developed to assess the coverage in parameter space for this signature at a centre-of-mass energy of 14 TeV assuming an integrated luminosity of 300 fb^{-1} in Ref. [?]. Background and signal Monte Carlo simulated samples are employed for the estimate of the results. The effect of the detector on the kinematic quantities utilised in the analysis is simulated by applying a Gaussian smearing to the momenta of the different reconstructed objects and reconstruction and tagging efficiency factors. Figure 53 shows the sensitivity reach for two of the parameter scans proposed in this whitepaper. On the top panel the exclusion reach for the $m(a), \tan\beta$ plane is presented, assuming $\sin\theta = 0.35$ and $m(A) = m(H^\pm) = m(H) = 500 \text{ GeV}$. It is possible to observe that for this scenario the sensitivity reach is comparable to the one from the mono-h signature as presented in Ref. [?]. On the bottom panel of Figure 53 the signature's sensitivity to benchmark #4 is evaluated for the first time.

4.2.7 Uncovered signatures with $tth + E_T^{\text{miss}}$

As discussed in Section ??, the production of the heavy mediator A gives a sizeable contribution to the $tt + E_T^{\text{miss}}$ production cross section in the $2HDM + a$ model. This is also

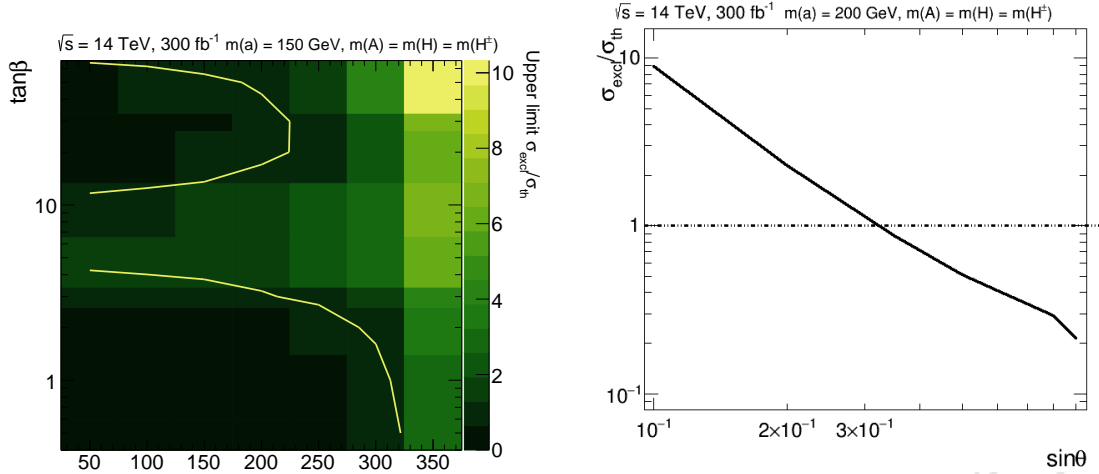


Figure 53: Exclusion reach for benchmark #2 (top) and benchmark #4 (bottom), assuming $\sin\theta = 0.35$ and $m(A) = m(H^\pm) = m(H) = 500 \text{ GeV}$.

true for the heavy H . When the decay of these mediators into the lightest pseudoscalar a is allowed, this decay process dominates over the direct decay into $\chi\chi$. In symmetry with what happens for the mono-h signature discussed in [?], for certain region of parameter space the signatures $pp \rightarrow t\bar{t}A \rightarrow t\bar{t}ah$ and $pp \rightarrow t\bar{t}H \rightarrow t\bar{t}aZ$ become sizeable. For the former case, it can be estimated from Fig. 12(b) of Ref. [?] that for relatively small $m(A)$ the $pp \rightarrow t\bar{t}ah$ cross section can be up to 30% that of the $pp \rightarrow t\bar{t}\chi\chi$ process. The interplay between the parameters of the model, and especially between the heavy higgs masses for these types of final state render the phenomenology interesting and variegated, as can be seen for example in the branching ratio study of Fig. 54, although further studies are needed to fully understand the interplay and the complementarity between these $tth + E_T^{\text{miss}}$ channels and the traditional heavy flavour dark matter searches.

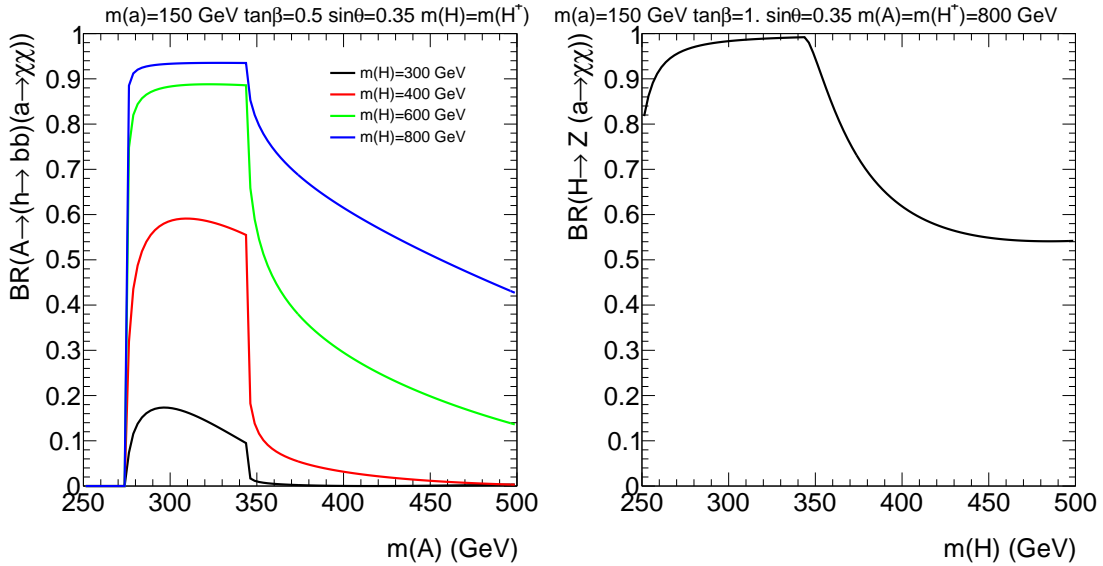


Figure 54: Example of the dependence of the A and H branching ratio into ah as a function of some parameters of the 2HDM model.

4.2.8 Top pair resonant searches

Heavy (pseudo)scalar bosons with $M_{A/H} \geq 2M_t$ and $\tan\beta \sim \mathcal{O}(1)$ decaying dominantly into top-quark pairs can be searched for by studying the resulting $\bar{t}t$ invariant mass spectra. However, interference effects between the signal processes and the SM $\bar{t}t$ production distort the signal shape from a single peak to a peak-dip structure [?]. The first search in this challenging decay channel was conducted recently, probing scalar and pseudoscalar masses between 500 and 650GeV in a minimal 2HDM [?]. A similar kinematic range could be probed if the result were re-interpreted in the context of the 2HDM+a. Interference between a loop-induced and a tree-level process cannot currently be simulated in MADGRAPH 5. To amend this problem, the same "Higgs_Effective_Couplings_FormFactor" approach [?] as adopted in [?] is implemented in the UFO, replacing the loop production by an effective vertex. The predictions of the modified UFO for the case, in which the pseudoscalar mediator does not mix with the heavy pseudoscalar A ($\sin\theta = 0$), i.e. effectively decouples from the 2HDM Higgs sector, are compared to those for the minimal 2HDM. Excellent agreement is found in the invariant mass distributions of A/H decaying into a top pair are shown in Fig. 55. As examples of how the sensitivity changes as a function of the parameters of the 2HDM+a, the $M_{\bar{t}t}$ distributions of pseudoscalars decaying into $\bar{t}t$ are presented in Fig 56. Larger values of $\tan\beta$ or $\sin\theta$ are expected to yield lower sensitivities to $A \rightarrow \bar{t}t$ significantly while M_a almost only affects the contribution from $a \rightarrow \bar{t}t$, which becomes sizeable if M_a is close to $2M_t$.

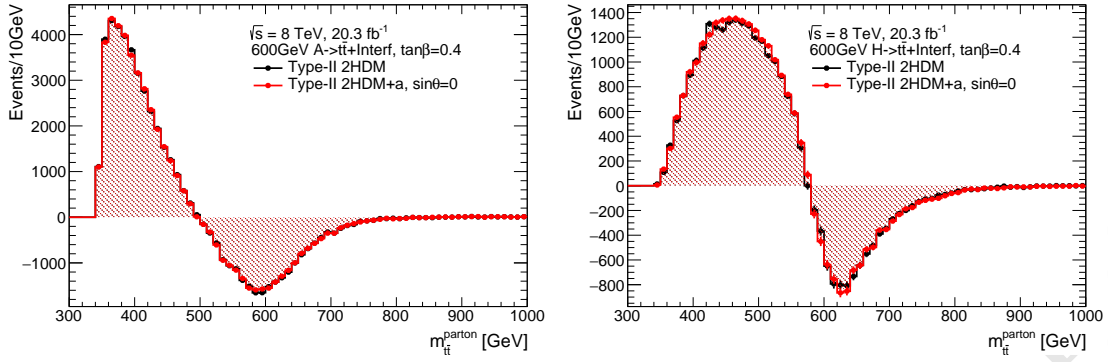
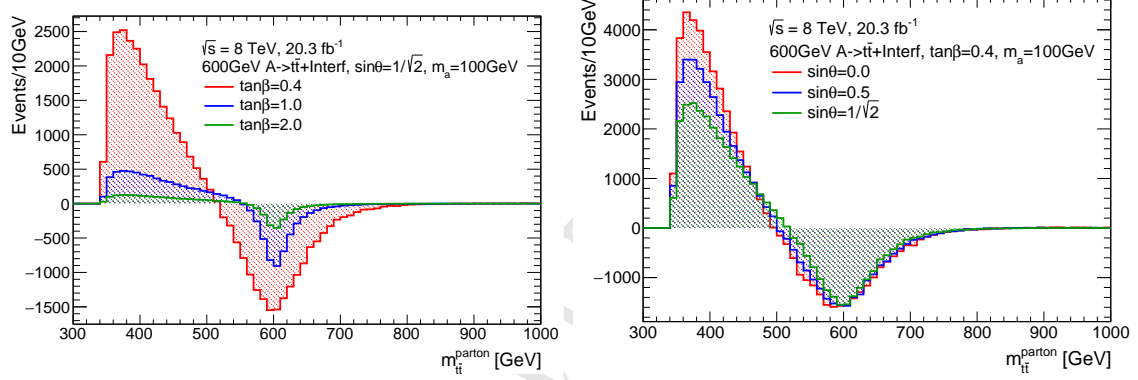
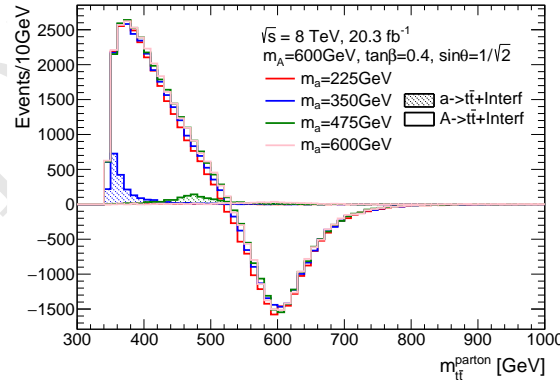


Figure 55: $M_{\tilde{t}\tilde{t}}$ distribution of the heavy (pseudo)scalar boson decaying into $\tilde{t}\tilde{t}$ with $M_A = M_H = 600\text{GeV}$, $\tan \beta = 0.4$, $\sin \theta = 1/\sqrt{2}$ and $M_a = 100\text{GeV}$ in comparison with the one from the generic 2HDM.



(a) $\tan \beta$ dependency with fixed $\sin \theta = 1/\sqrt{2}$ and $M_a = 100\text{GeV}$

$M_a = 100\text{GeV}$



(c) M_a dependency with fixed $\tan \beta = 0.4$ and $\sin \theta = 1/\sqrt{2}$

Figure 56: parameter dependency of signal $M_{\tilde{t}\tilde{t}}$ distribution mediated by pseudoscalars. The value of M_A is fixed at 600GeV .

4.2.9 Four tops final states

The topology involving four top-quarks in the final state is a rare, yet increasingly important signature, which will gain sensitivity and attention with the enlargement of the dataset delivered by the LHC. In the attempt to perform a first characterisation of this topology, we have studied the predicted cross-section for the four top final state of this model for two sets of parameter choices.

In Figure 57a we present the four top cross section for the parameter choices of benchmark #2, for an intermediate choice of mass of the light pseudoscalar ($m(a) = 400$ GeV), as a function of $\tan\beta$. The total four-top production cross section, which accounts for both SM and new physics (NP) contributions and is indicated as $|SM + NP|^2$ in the legend, is compared with the production cross section contributions separately due to SM and NP terms. This is achieved technically by setting a requirement on the number of QCD and QED vertices in madgraph, as indicated in Table 6. Furthermore, the different contributions from on-shell production of each CP-odd and CP-even mediators associated with a top pair and decaying into a top pair is indicated. The dominant contribution is driven by the on-shell production of A and H for all choices of $\tan\beta$ in this benchmark. In the lower panel of Figure 57a, the effect of the interference term between the 2HDM+a and the SM is assessed, and is found to have an impact almost always smaller than 5% on the inclusive cross-section. **Checking whether true for some fiducial cuts, would be important to add statement or clarify that is is not fully conclusive as it is only inclusive.**

In Figure 57b we present instead the cross-section study for the parameter choices of benchmark #3b, for $\sin\theta = \frac{1}{\sqrt{2}}$ and as a function of the light pseudoscalar mass. Very interestingly, for this parameter choices the cross-section is quite independent of $m(a)$. As it can be observed from the on-shell contribution breakdown, at the low-end of the mass spectrum the $\bar{t}t + a$ production dominates, with a peak at 400 GeV due to the competition between $a \rightarrow \chi\chi$ and $a \rightarrow \bar{t}t$ and the natural decreasing of the cross section with the increase of $m(a)$. The contribution of $\bar{t}t + H$ and $\bar{t}t + A$ processes compensates the latter effect in the higher end of the mass-spectrum, with the turn on starting around 800 GeV due to the competition between $A/H \rightarrow \bar{t}t$ and cascade decays of the heavy higgses into the light pseudoscalar mediator ($A \rightarrow ah/H \rightarrow aZ$). The little bump at 1 TeV is due to interference effects between the three higgs mediators, which are all set to the same mass for this parameter choice. The inclusive production cross-section of the 2HDM+a model is also compared with the one obtained by the DMSimp pseudoscalar implementation. Furthermore, as for the previous benchmark, the impact of the SM interference term on the inclusive cross-section is found to be very small (< 2%), except for $m(a)$ values close to the top threshold.

Finally, in Figure 58 we compare for a small $\tan\beta$ value, the cross section of four-top production from NP processes (see Tab. 6) of benchmarks #3a and #3b. This cross-section increases for benchmark #3b for increasing $\sin\theta$, as the production mechanism is dominated by $\bar{t}t + a(\bar{t}t)$. A different and more flat trend is instead observed for benchmark #3a, for which the $\sin\theta$ dependence is more complex and driven by the branching ratios

MADGRAPH rule	Legend symbol	Details
<code>p p > t t~ t t~ / a z h1 QED<=2</code>	$ SM + NP ^2$	Four-top production including both SM and NP contributions and their interference.
<code>p p > t t~ t t~ / a z h1 QCD<=2</code>	$ NP ^2$	Four-top production from NP processes, including interference terms among A, H, a .
<code>p p > t t~ t t~ / a z h1 QED<=0</code>	$ SM ^2$	Four-top SM production.

Table 6: Description of the specific MADGRAPH settings used to derive the different curves of Figs 57a and 57b.

of A and H in a top pair, as the $a \rightarrow \bar{t}t$ threshold is closed in this case.

4.2.10 2HDM+scalar sensitivity studies

The sensitivity of the $t\bar{t} + E_T^{\text{miss}}$ all-hadronic signature ?? to the Type-II model with two Higgs doublets plus a scalar portal to dark matter S_1 described in ?? has been investigated. The signature has been chosen as is the one providing the best sensitivity across the majority of the mass range for S_1 which is most difficult to address.

The choice of the parameters for this model largely reflects that of the $2HDM + p$ model. In particular, the masses of the heavier scalar S_2 and the masses of the charged Higgs and the CP-odd scalar have been set to 600 GeV. The value of the mixing angle has been set to $\cos \theta = 0.35$. The mass of the light scalar S_1 is scanned between 200 and 340 GeV, and $\tan \beta$ is scanned between 0.2 and 1. Across the whole $\tan \beta$ and mass range considered the widths of both the light and the heavy scalars do not exceed 15% of the mass of the corresponding particle.

The procedure to extract the results follows closely the procedure described in Sec. 4.2.4, but with the light and heavy pseudo-scalars a and A replaced by the light and heavy scalars S_1 and S_2 , respectively. The formula to rescale the results of the acceptance is therefore turned into:

$$Acc_{2HDM}(m(S_1), M(S_2)) = \frac{\sigma_{S_1} \times Acc_{DMSIMP}(m(S_1)) + \sigma_{S_2} \times Acc_{DMSIMP}(m(S_2))}{\sigma_{S_1} + \sigma_{S_2}} \quad (4.10)$$

The validity of this re-scaling has been validated by comparing the acceptance to the simplified models to the acceptance to the $2HDM + S_1$ models, before and after applying the rescaling of Eq. 4.10. The results are shown if Fig. 59 across the whole mass range for the light scalar S_1 considered, for the minimum and maximum values of $\tan \beta$ taken into account. It has to be noted that the acceptance to simplified models and $2HDM + S_1$ is very similar even before applying the rescaling of Eq. 4.10. This is due to the fact that the ratio between the cross-section of S_2 and the cross-section of S_1 becomes appreciable (i.e.

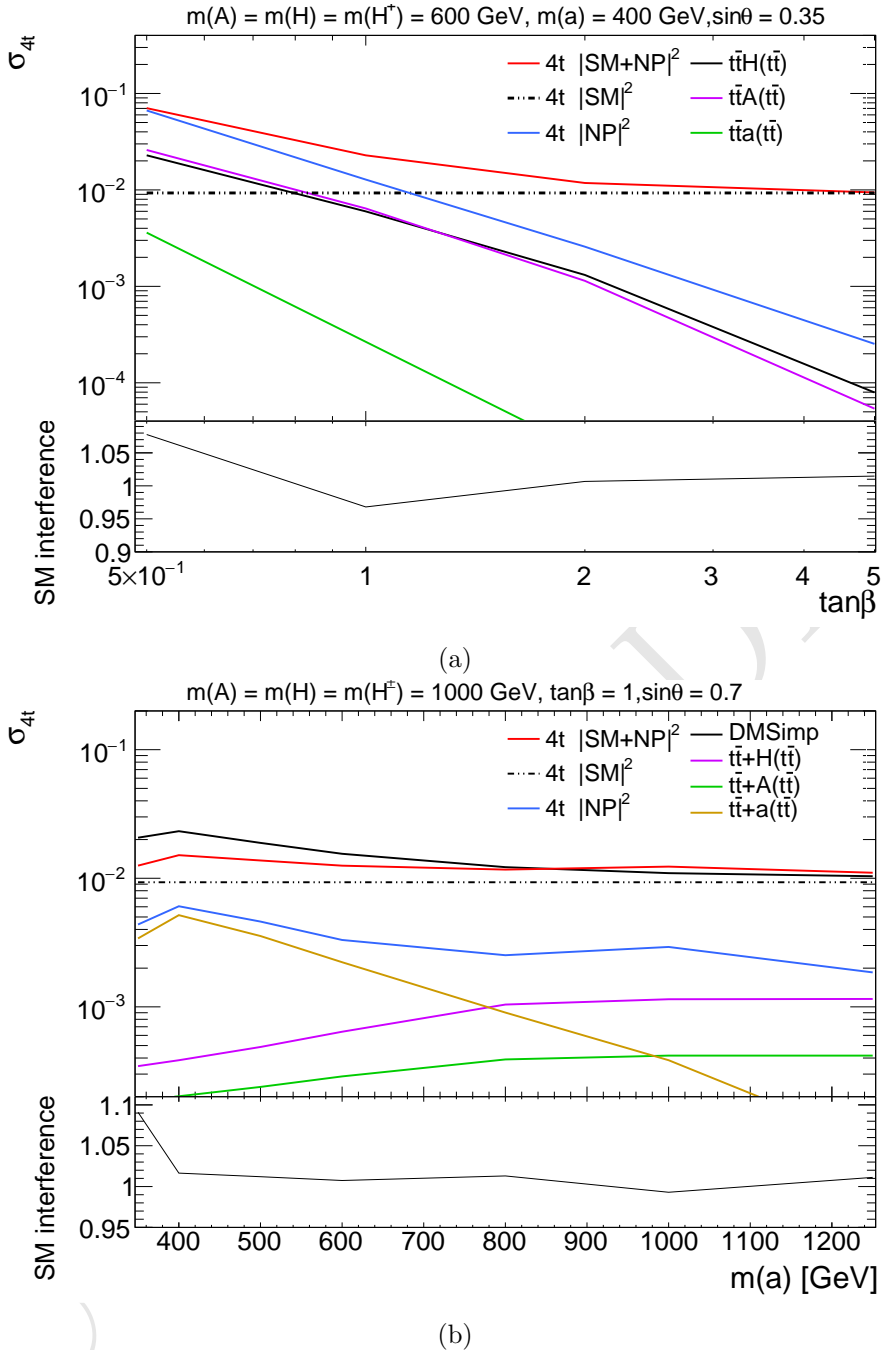


Figure 57: Four-top cross section study for a subset of the parameter space of benchmark #2 (top) and #3 (bottom). The different Standard Model (SM) and New Physics (NP) contributions with and without interference and the breakdown in terms of on-shell mediator production is presented, following the notation of Table 6.

above sub-percent level) only for models with $m(S_1) > 300 \text{ GeV}$ and $\tan\beta > 0.4$.

Fig. 60 shows the results of the recasting of the simplified model results in the context

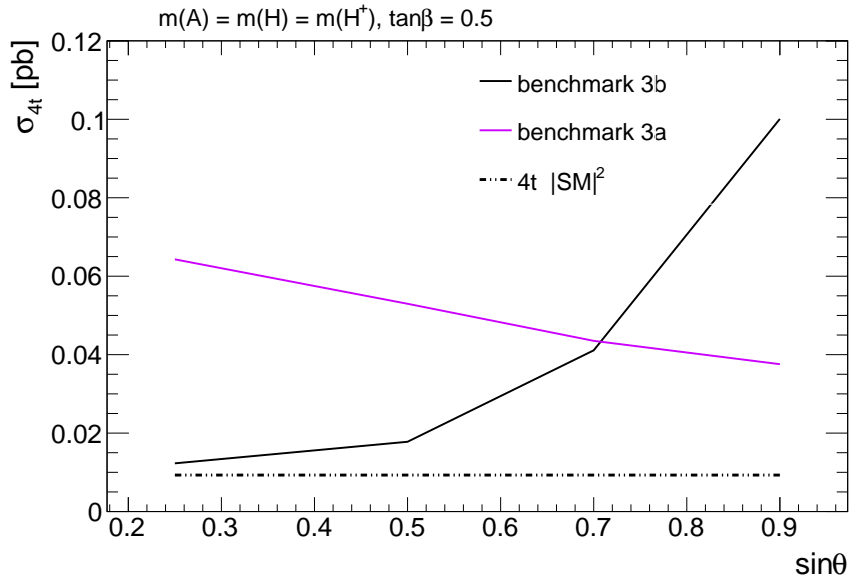


Figure 58: Four-top cross section comparison for benchmarks #3a and #3b. Only NP contribution is presented, following the notation of Table 6.

of the $2HDM + S_1$ model. For the choice of parameters made, models with scalar mediator between 100 and 360 GeV can be excluded for $\tan\beta = 0.2$, while for $\tan\beta = 1$ masses between 100 and 120 GeV are excluded.

4.2.11 Other signatures

4.2.12 Monojet

The search for events with at least one jet and large missing transverse momentum in the final states can be also interpreted in the context of the 2HDM+a model. In this scenario the light pseudo-scalar mediator which decays in DM particles can be radiated from heavy quark loops providing such a signature. This channel is able to probe a phase space with low $\tan(\beta)$ and high $\sin\theta$ in which the cross-sections of this kind of processes are enhanced.

4.2.13 Resonant Production at Collider (Comparison)

The cross section for a resonant production process, with final state X , where a spin-0 resonance S is produced and then decays, can be written as

$$\sigma(pp \rightarrow S \rightarrow X) = \frac{\Gamma(S \rightarrow X)}{M\Gamma_S} \sum_i C_i \Gamma(S \rightarrow i) = \frac{1}{Ms} \sum_i C_i \Gamma(S \rightarrow i) BR(S \rightarrow X) \quad (4.11)$$

where i are the possible initial states, C_i are weight factors that account for the protons PDFs and colour factors, and s is the center of mass energy squared $s = (13TeV)^2$.

The values of the C_i are as follows

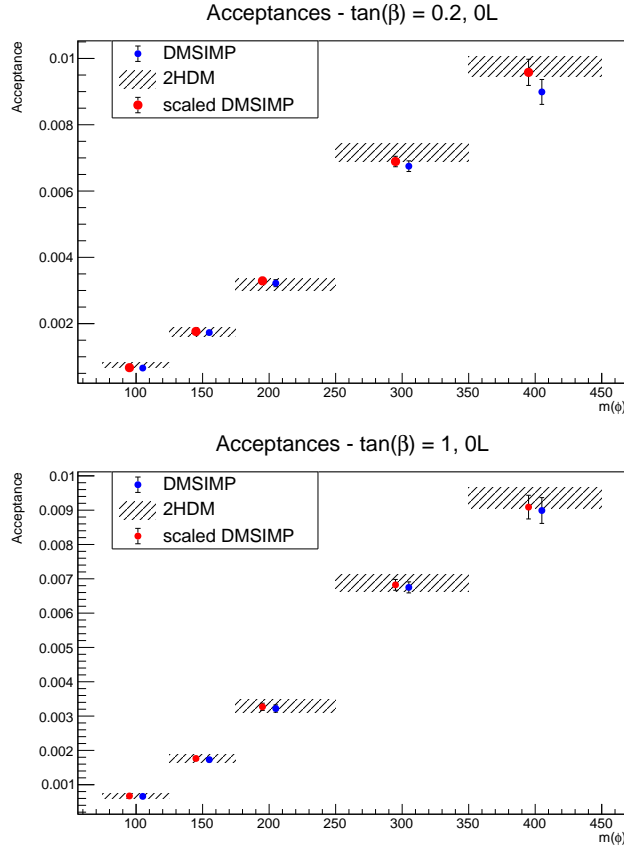


Figure 59: Validation of the re-scaling formula as a function of $m(S_1)$ for the minimum and maximum values of $\tan \beta$ considered.

$$C_{gg} = \frac{\pi^2}{8} \int_{M^2/s}^1 \frac{dx}{x} g(x) g\left(\frac{M^2}{sx}\right) \quad (4.12)$$

$$C_{q\bar{q}} = \frac{4\pi^2}{9} \int_{M^2/s}^1 \frac{dx}{x} \left(q(x) \bar{q}\left(\frac{M^2}{sx}\right) + q\left(\frac{M^2}{sx}\right) \bar{q}(x) \right) \quad (4.13)$$

Assuming gluon fusion production to be the dominant one, the ratio of the cross sections for the scalar and pseudoscalar model for mono-higgs and mono-Z will be

$$\frac{\sigma_S(pp \rightarrow S_2 \rightarrow \bar{\chi}\chi h)}{\sigma_P(pp \rightarrow A \rightarrow \bar{\chi}\chi h)} = \frac{\Gamma(S_2 \rightarrow gg)}{\Gamma(A \rightarrow gg)} \frac{BR(S_2 \rightarrow S_1 h)}{BR(A \rightarrow ah)} \frac{BR(S_1 \rightarrow \bar{\chi}\chi)}{BR(a \rightarrow \bar{\chi}\chi)} \quad (4.14)$$

$$\frac{\sigma_S(pp \rightarrow A \rightarrow \bar{\chi}\chi Z)}{\sigma_P(pp \rightarrow H \rightarrow \bar{\chi}\chi Z)} = \frac{\Gamma(A \rightarrow gg)}{\Gamma(H \rightarrow gg)} \frac{BR(A \rightarrow S_1 Z)}{BR(H \rightarrow aZ)} \frac{BR(S_1 \rightarrow \bar{\chi}\chi)}{BR(a \rightarrow \bar{\chi}\chi)} \quad (4.15)$$

The ideal situation to detect a mono-higgs/Z signal is to have such BR close to 1: if this is the case, the ratio of the signals becomes just the ratio of the widths

$$\frac{\sigma_S(pp \rightarrow S_2 \rightarrow \bar{\chi}\chi h)}{\sigma_P(pp \rightarrow A \rightarrow \bar{\chi}\chi h)} \sim \frac{\Gamma(S_2 \rightarrow gg)}{\Gamma(A \rightarrow gg)} \quad (4.16)$$

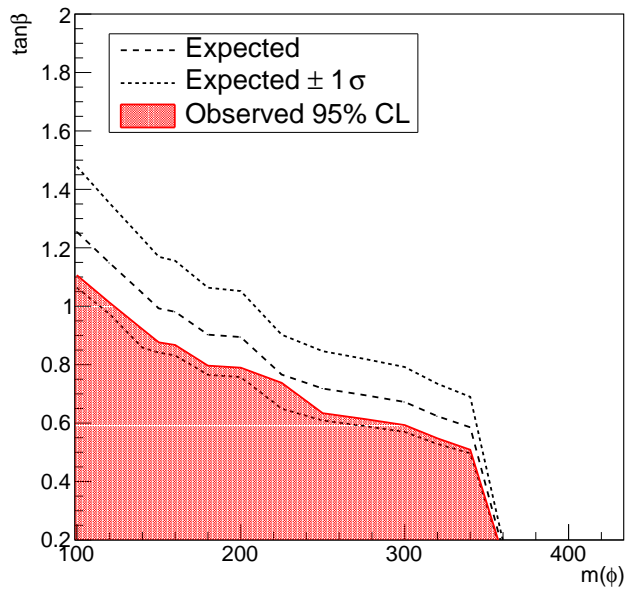


Figure 60: Expected and observed exclusion limits at 95% C.L. obtained as a result of the recasting of the all-hadronic channel in the context of the $2HDM + S_1$ model.

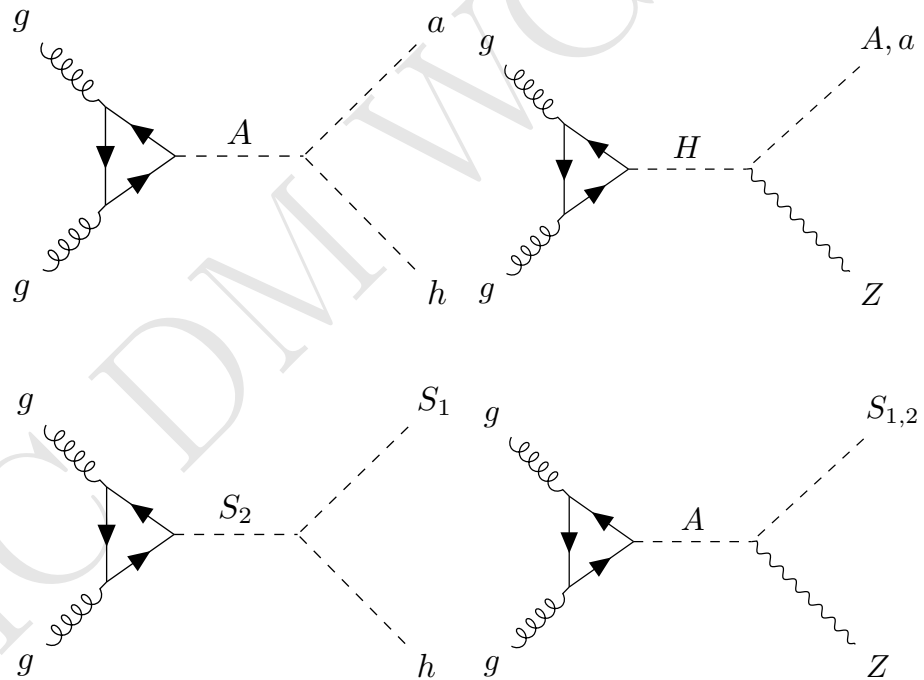


Figure 61: Feynman diagrams for resonant production signals signatures leading to mono-Z or mono-h.

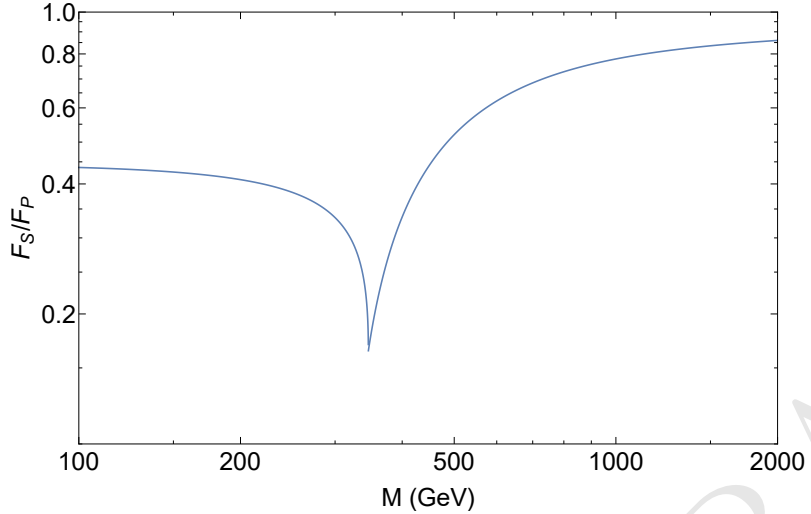


Figure 62: Ratio F_S/F_P as a function of the mass $M = M_A = M_{S_2}$.

$$\frac{\sigma_S(pp \rightarrow A \rightarrow \bar{\chi}\chi Z)}{\sigma_P(pp \rightarrow H \rightarrow \bar{\chi}\chi Z)} \sim \frac{\Gamma(A \rightarrow gg)}{\Gamma(H \rightarrow gg)} \quad (4.17)$$

the width for a scalar or pseudoscalar particle to gluons are:

$$\Gamma(S \rightarrow gg) = \frac{g_S^2 \alpha_s^2 M}{16\pi^3} F_S \left(\frac{4m_t^2}{M^2} \right) \quad (4.18)$$

$$\Gamma(P \rightarrow gg) = \frac{g_P^2 \alpha_s^2 M}{16\pi^3} F_P \left(\frac{4m_t^2}{M^2} \right) \quad (4.19)$$

where

$$F_S(x) = x |1 + (1-x) \arctan^2 \frac{1}{\sqrt{x-1}}|^2 \quad (4.20)$$

$$F_P(x) = x |\arctan^2 \frac{1}{\sqrt{x-1}}|^2 \quad (4.21)$$

and $g_S = -y_t \sin \theta \epsilon_u$ for $S = S_2$, $g_P = y_t \epsilon_u$ for A in the scalar model, and $g_S = y_t \epsilon_u$ for $S = H$, $g_P = y_t \cos \theta \epsilon_u$ for A in the PS model. Note that the definition of the mixing angle is reversed in the scalar model comparing to the PS. So assuming equivalent mixing angle configurations, Eq. 4.16 and 4.17 reduce to

$$\frac{\sigma_S(pp \rightarrow S_2 \rightarrow \bar{\chi}\chi h)}{\sigma_P(pp \rightarrow A \rightarrow \bar{\chi}\chi h)} \sim \frac{F_S(\frac{4m_t^2}{M^2})}{F_P(\frac{4m_t^2}{M^2})} < 1 \quad (4.22)$$

$$\frac{\sigma_S(pp \rightarrow A \rightarrow \bar{\chi}\chi Z)}{\sigma_P(pp \rightarrow H \rightarrow \bar{\chi}\chi Z)} \sim \frac{F_P(\frac{4m_t^2}{M^2})}{F_S(\frac{4m_t^2}{M^2})} > 1 \quad (4.23)$$

The ratio F_S/F_P is shown in Fig. 62 as a function of the mass $M = M_A = M_{S_2}$.

4.2.14 Final proposal for parameter scan

- a two-dimensional scan in the light pseudoscalar mass (ma) - heavy pseudoscalar mass (mA) plane where $ma = mA$, fixing tanBeta to 1.0, sinTheta to 0.35 and the Dark Matter mass (mDM) to 10 GeV.
- a one-dimensional scan in DM mass from 1 GeV to 500 GeV for a point in the middle of the sensitivity range for the mono-V analyses at mA=600, ma=250 GeV, so the connection between this model and cosmology is clear as the measured relic density starts being satisfied at values of DM mass around 100 GeV

In order to explore changes in complementarity with different analyses and kinematics, this should be complemented by:

- a two-dimensional scan in the ma tanBeta plane, for comparison with the ttbar+MET / bbar+MET analyses. In this case, the charged Higgs mass ($mH^{+/-}$), the heavy pseudoscalar mass (mA) and the heavy Higgs mass (mH) should be fixed to 600 GeV. This scan includes points: 50, 45, 40, 35, 30, 25, 20, 15, 10, 5 for M(a) masses between 10 and 350 GeV. The high-tanBeta points would be of primary interest to the HF + DM searches. Uli's studies have shown that one can simply reweight the existing tt+DM/bb+DM models from DMF to the new 2HDM+PS cross sections; full simulation of the newly proposed 2HDM+PS points is not required.
- two one-dimensional scans in $\sin\theta$ for the comparison of mono-Higgs and bbar+MET analysis (it is expected that the bbar+MET analysis will only have to rescale previous models/cross-sections) [2]: - $mH = mA = mH = 600\text{GeV}$, $ma = 200\text{GeV}$, $\tan\text{Beta}=1$ - $mH = mA = mH = 1000\text{GeV}$, $ma = 350\text{GeV}$, $\tan\text{Beta}=1$

The PDF recommended is five-flavor. ATLAS will use the NNPDF3.0 PDF set. Some text by Fabio Maltoni and Ulrich Haisch can be found in the texinputs_app folder.

5 Connection with cosmology

5.1 Pseudoscalar

An important requirement for models of dark matter is their consistency with existing astrophysical observations, namely the observed dark matter relic density. The relic density is driven by the annihilation cross-section of dark matter into SM particles. For a given model of dark matter-SM interactions, the annihilation cross-section is fully defined and a calculation of the resulting relic density can be performed.

5.2 Technical setup

The MADDM [? ?] plugin for MG5.aMC@NLO is used to calculate the present-day relic density for this model. By modeling the thermal evolution of the cross-section during the expansion of the early universe, the time of freeze-out is determined. All tree-level annihilation processes are taken into account, and the Yukawa couplings of all fermions are

taken to be non-zero. The Feynman diagrams of annihilation processes taken into account in this calculation are shown in Fig. 63. Generally, the annihilation proceeds via single or double s-channel exchange of the pseudoscalars a and A , with subsequent decays. Since MADDM uses only tree-level diagrams, contributions from off-shell pseudoscalars can only be taken into account for the case of single s-channel mediation with direct decay of the pseudoscalar to SM fermions. If the pseudoscalar instead decays to other bosons or if the annihilation proceeds through double s-channel diagrams, the outgoing bosons are taken to be on-shell and their decays are not simulated.

In all scans presented here, the common parameter choices $\sin(\theta) = 0.35$, $m_h = 125\text{GeV}$, $g_\chi = 1$, $\lambda_i = 3$ are used.

5.3 Results

The relic density is shown for a scan in the M_a - M_χ plane in Fig. 64. For small values of M_χ below the mass of the top quark, DM is mostly overabundant. In this regime, annihilation to quarks is suppressed by the small Yukawa couplings of the light fermions. The observed relic density can only be achieved for $M_\chi \approx M_a/2$, where annihilation is resonantly enhanced, or for $M_\chi \approx (M_a + M_h)/2$, close to the threshold for the $\chi\chi \rightarrow ha$ process. Above the top threshold, annihilation into fermions becomes very efficient and DM is underabundant. As M_χ increases further, annihilation via single s-channel diagrams is increasingly suppressed and the relic density rises again. The observed density is reproduced again for $M_\chi \approx 1\text{TeV}$ at low M_a . For values of M_a beyond the LHC reach of a few TeV, the allowed parameter region at the top threshold $M_\chi \approx m_{\text{top}}$ stays independent of the value of M_a , indicating that a DM candidate that is mass degenerate with the top quark cannot be excluded by LHC searches alone.

The dependence of the relic density on the choice of M_χ is further explored by performing a one-dimensional scan, as shown in Fig. 65. The relic density shows clear structures corresponding to the previously discussed regions of resonant enhancement, as well as kinematic boundaries. Overall, the behavior is dominated by the low- M_χ suppression of the annihilation cross-section, the resonant enhancement at $M_\chi = M_a/2$ and the kinematic top thresholds. Other effects, such as resonant enhancement of $\chi\chi \rightarrow A$ annihilation are present, but only have small effects.

5.4 Scalar

The 2HDM+S scenario has multiple DM annihilation channels. There are tree-level annihilations to fermion-antifermion pairs, scalars (the SM Higgs, the two neutral scalars, the pseudoscalar, and the charged scalars) and/or the electroweak gauge bosons, namely: $\bar{\chi}\chi \rightarrow \bar{f}f$, S_1S_1 , S_2S_2 , S_1S_2 , H^+H^- , H^+W^- , AA , AZ , S_1h , and S_2h – these are shown in Fig. 66. This is to be compared with a single mediator model in which only the $\bar{f}f$ and SS channels are present. Note that since all diagrams involve χ -scalar vertices (including those with gauge boson final states) they are all p -wave processes. As such, while we will easily be able to find parameters that accommodate the observed relic density, there will be no constraints arising from indirect detection because the p -wave annihilation processes are highly velocity suppressed in the late universe.

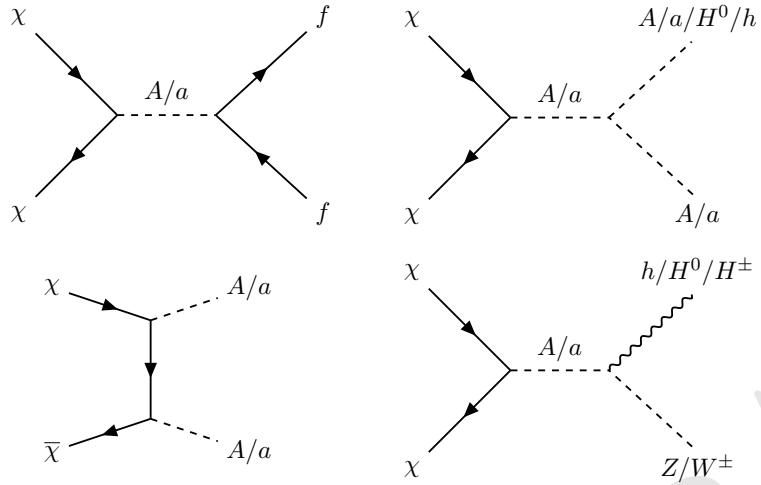


Figure 63: Annihilation diagrams taken into account in the relic density calculation.

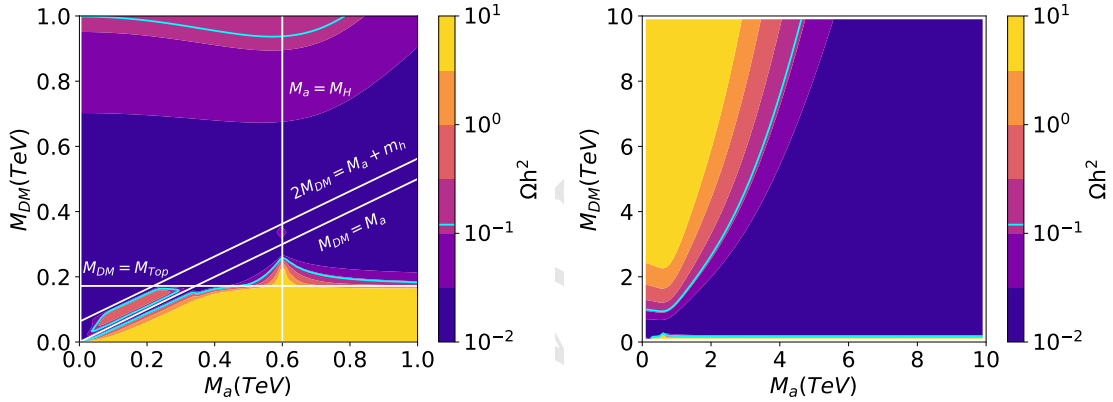


Figure 64: Predicted relic density for a two-dimensional scan of M_χ and M_a . The other parameters of the model remain fixed with $m_H = m_A = m_{H^\pm} = 600$ GeV and $\tan \beta = 1$, as well as the default choices described in the text. The color scale indicates the relic density, the cyan solid line shows the observed value of $\Omega h^2 = 0.12$. The color scale is truncated at its ends, i.e. values larger than the maximum or smaller than the minimum are shown in the same color as the maximum/minimum. While the left focuses on the mass region relevant to collider searches, the right panel shows the development of the relic density for a larger mass region.

If the DM particle is relatively light, such that annihilation to the scalars and electroweak bosons is kinematically forbidden ($m_\chi \lesssim 80$ GeV), the only annihilation channels that remain open are the fermionic ones. This case is heavily constrained, as the dominant annihilation channel is then $b\bar{b}$, which is suppressed by the bottom Yukawa coupling and thus usually requires resonant enhancement to accommodate the correct relic density.

If, instead, the DM particle is heavy enough to annihilate to the Higgs, electroweak gauge bosons and/or the new scalars, then these final states will likely dominate due

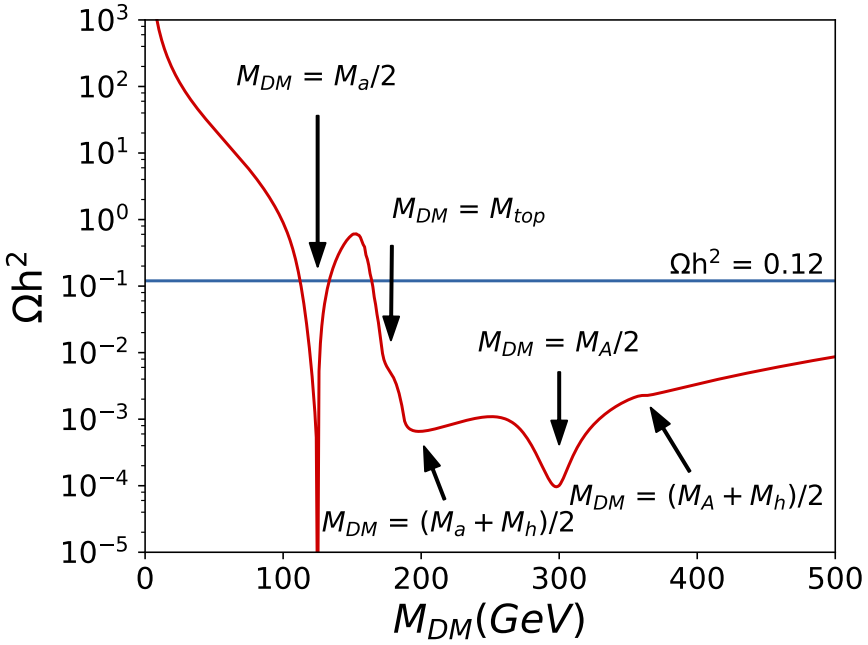


Figure 65: Relic density for a one-dimensional scan of M_χ . The other parameters of the model remain fixed with $m_H = m_A = m_{H^\pm} = 600$ GeV, $M_a = 250$ GeV and $\tan \beta = 1$, as well as the default choices described in the text. Various kinematic thresholds and regions of resonant enhancement are visible. Consistency with the observed value of $\Omega h^2 = 0.12$ is mainly controlled by the resonant enhancement of $\chi\chi \rightarrow a$, as well as the onset of $\chi\chi \rightarrow t\bar{t}$.

to the Yukawa suppression of annihilations to fermions (top excluded). Because all of these annihilations are governed by scalar and electroweak couplings – and exist due to gauge invariance, independent of the Yukawa couplings of the second doublet – they are also present, for example, in the limit where the second doublet is inert. This ability to produce the correct relic abundance independent of Yukawa structure means that DM can be adequately produced while avoiding any Yukawa dependent constraints (e.g. DD, neutral meson mixing, $b \rightarrow s\gamma$, $\mu \rightarrow e\gamma$, etc.).

We implemented the model in FeynRules⁴ [? ?] and output the model with the CALCHEP interface [?]. We then used `micrOMEGAs` [?] to perform the relic density calculation, where we included 3 body final states with off-shell gauge bosons. We also double checked the results by calculating the annihilation cross sections, which are reported in [?]. In the case where the parameter values are away from resonances and annihilation thresholds, one can use the wave expansion of the cross sections. The p-wave coefficients of this expansion are also reported in [?].

Sommerfeld enhancement can significantly increase the DM annihilation cross section [? ? ?], provided at least one of the scalars is both sufficiently light compared to the DM, and strongly coupled to the DM particle. In practice, for the parameter range we

⁴The FeynRules model file used is publicly available in the FeynRules model database.

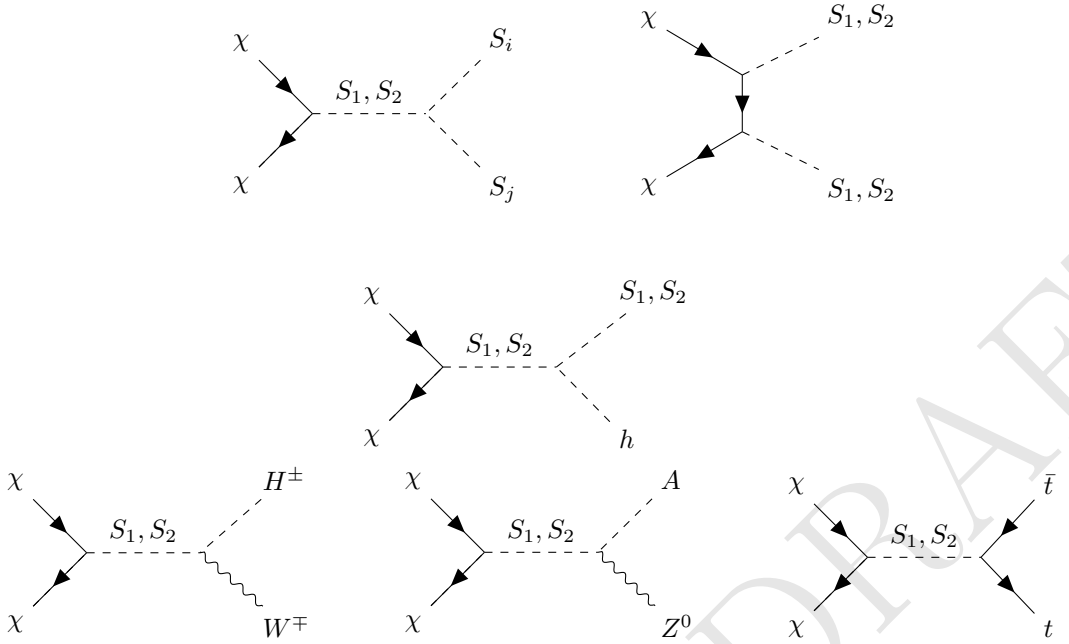


Figure 66: Dominant DM annihilation channels, where (S_i, S_j) is one of these scalar final states: (S_1, S_1) , (S_1, S_2) , (S_2, S_2) , (H^+, H^-) , (A, A) .

consider, this leads to $\mathcal{O}(1)$ corrections to the cross section; a discussion is provided in [?].

The independent parameters present in the model are

$$m_\chi, \quad M_{S_1}, \quad M_{S_2}, \quad y_\chi, \quad \hat{\lambda}_4, \quad \hat{\lambda}_5, \quad \hat{\lambda}_{hHS}, \quad \hat{\lambda}_{HHS}, \quad \epsilon_u \quad \text{and} \quad \epsilon_d. \quad (5.1)$$

This set of parameters, through the minima condition and the diagonalization relations, together with the additional constraint $m_\chi = y_\chi v_s$, determine all other parameters of the model⁵. The scan is performed in the following range:

$$70\text{GeV} < m_\chi < 1\text{TeV}, \quad (5.2)$$

$$70\text{GeV} < M_{S_1} < M_{S_2} < 2\text{TeV}, \quad (5.3)$$

$$0 < y_\chi < 2, \quad (5.4)$$

$$|\hat{\lambda}_{hHS}| < 2, \quad (5.5)$$

$$|\hat{\lambda}_{HHS}| < 4, \quad (5.6)$$

$$0 < \epsilon_u < 1, \quad (5.7)$$

while for $\hat{\lambda}_4$ and $\hat{\lambda}_5$ we scan over the region shown in [?]. These ranges for the couplings were chosen so that most of the points will satisfy unitarity and perturbativity bounds, which was checked via the scalar scattering matrices as in [?]. To achieve the right relic density, we will see that it will be in general necessary to have $m_\chi \gtrsim M_{S_1}$, and the

⁵The phase of the DM Yukawa can always be reabsorbed, so one can chose y_χ and v_s to be both real and positive.

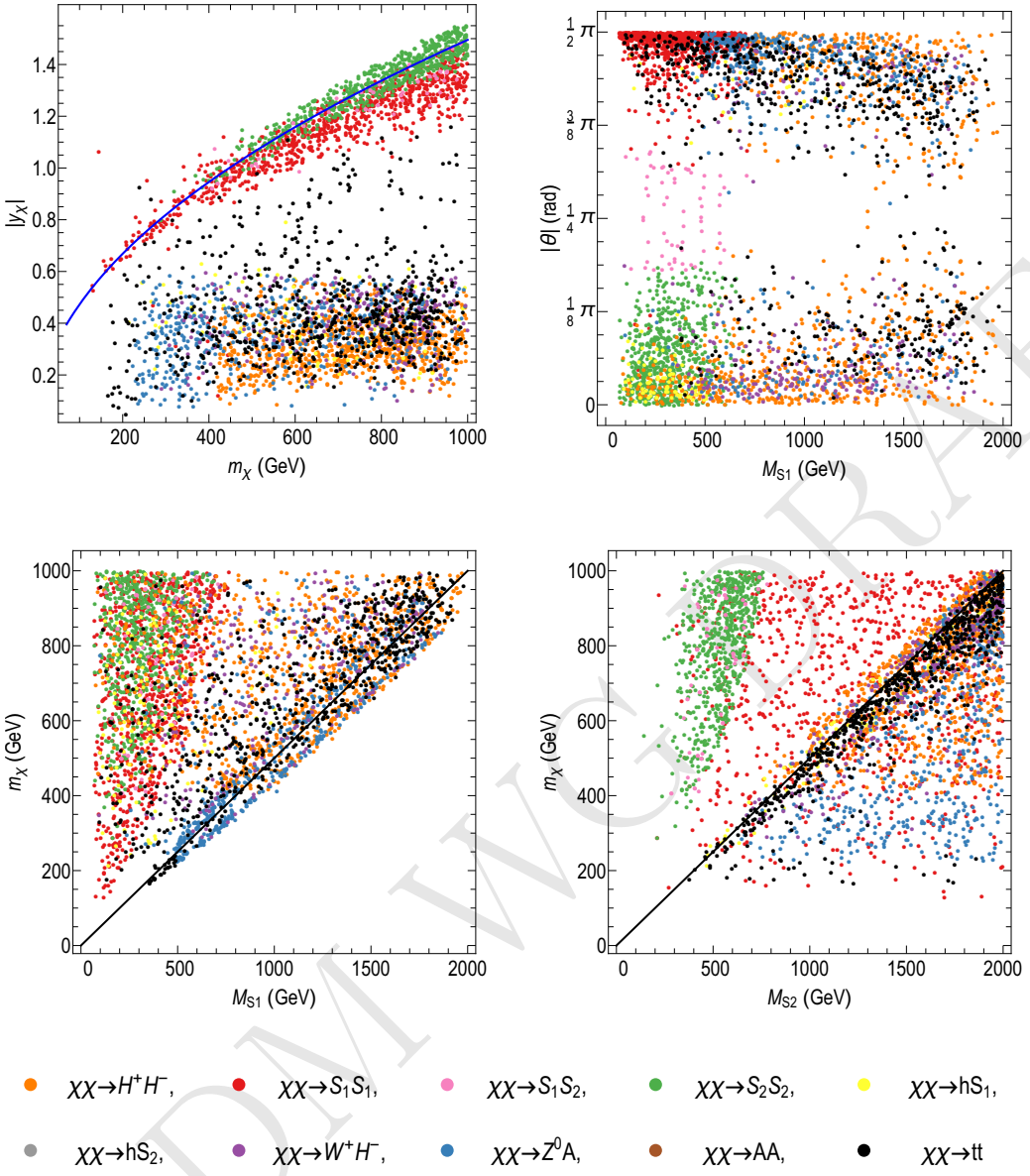


Figure 67: Points of our scan of parameter space that produce the correct relic density. The colours represent the dominant annihilation channel, as shown above. 15000 points are taken that survive the constraints, and of them only 25% of the H^+H^- channel and 10% of the S_1S_1 channel are shown for clarity. The black line in the lower panels indicate $m_\chi = 2M_{S_1, S_2}$, which is the resonance condition for the s-channel annihilation processes. The blue line in the top left panel represents the scaling expected for a cross section of $\langle\sigma v\rangle \sim y_\chi^4 v^2 / 16\pi^4 m_\chi^2$ which, in this model, applies to a pure $\bar{\chi}\chi \rightarrow S_iS_i$ scenario.

inequality is strictly required for DM masses below the top mass, as otherwise all considered annihilation channels are closed. In this low DM mass region, however, one needs to take into account Higgs invisible constraints [? ?]: 2-body decays forbid the region $2m_\chi < m_h$

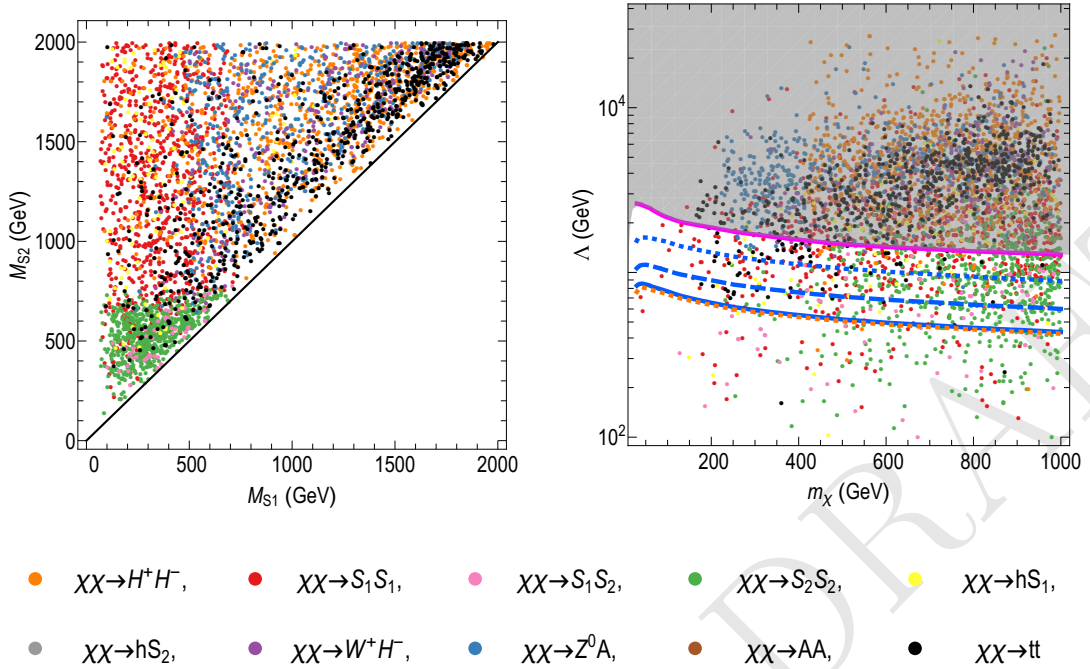


Figure 68: Points of our scan of parameter space that produce the correct relic density. The colours represent the dominant annihilation channel, as shown above. 15000 points are taken that survive the constraints, and of them only 25% of the H^+H^- channel and 10% of the S_1S_1 channel are shown for clarity. Λ is the effective cut-off scale for the DD effective operator; the dotted orange line represents the constraint from the LUX 2016 results [?], the solid blue represents the XENON1T experiment [?], the dashed blue the projection for the XENON1T experiment with $2t \cdot y$ of data taking, the dotted blue the projection for the XENONnT experiment with $20t \cdot y$ of data taking [?], and the magenta is the DD sensitivity at the “neutrino floor”[?].

and $2M_{S_1} < m_h$, while considering 3-body decays as well further pushes up the lower bound on M_{S_1} to nearly 100GeV. The Higgs invisible decays constraints can only be avoided in the $\theta \rightarrow \pi/2$ limit, but in such case the model approaches a decoupled dark sector which is phenomenologically uninteresting⁶. Taking into account these considerations, we have chosen in our scan a conservative lower bound for the DM mass and for the lightest scalar of 70GeV. Points are selected if they have a relic density between $0.1 < \Omega h^2 < 0.14$ and satisfy all bounds from flavour, unitarity, perturbativity, tree level vacuum stability, and DD constraints.

The relic density is insensitive to the value of ϵ_d , while the DD results depend on the relationship ϵ_d and ϵ_u . We set $\epsilon_d = \epsilon_u$ for the scans presented in Fig. 67 and Fig. 68 (with

⁶Relic density requirement can be satisfied in the limit of a decoupled dark sector, in which dark matter annihilates to light dark scalars. However, there would be no signals in collider or direct detection experiments. Moreover, indirect detection is prevented by the p-wave nature of annihilation to scalars, even if small couplings to the SM are included.

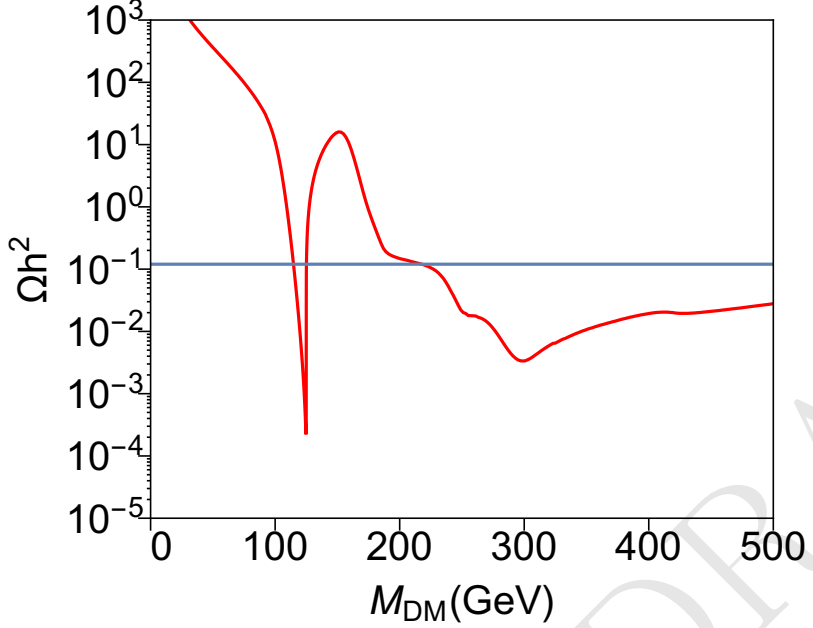


Figure 69: One-dimensional scan of the parameter space. We fix all other parameters, see the text for more details.

the exception of the right panel of Fig. 68, which enforces no DD constraint and hence has no ϵ_d dependence).

We have chosen to define S_1 to be the lighter of the 2 scalars, and allow θ to range from 0 to $\pi/2$. As one can always switch the two scalars by sending $\theta \rightarrow \pi/2 - \theta$, an equivalent choice would be to take $0 < \theta < \pi/4$ without requiring any mass ordering.

In Fig. 69 we show the value of the relic density obtained through thermal freezeout in a one-dimensional scan, where we kept fixed all parameters except the DM mass. We fix $M_{S_1} = 250\text{GeV}$, $M_{S_2} = M_A = M_{H^+} = 600\text{GeV}$, $\cos \theta = 0.35$ (equivalent to $\sin \theta = 0.35$ for the PS model), $y_\chi = 1$,

These choices of parameters, along with alignment conditions and $m_\chi = v_s y_\chi$, then fix

$$v_s = \frac{m_\chi}{y_\chi} = m_\chi, \quad (5.8)$$

$$\lambda_1 = \frac{m_h^2}{v^2} \sim 0.258, \quad (5.9)$$

$$\lambda_s = \frac{1}{4v_s^2} (M_a^2 + M_A^2 + (M_A^2 - M_a^2) \cos(2\theta)) \sim \frac{222.4^2 \text{GeV}^2}{m_\chi^2}, \quad (5.10)$$

$$\lambda_{12s} = \frac{(M_{S_1}^2 - M_{S_2}^2) \sin(2\theta)}{2vv_s} \sim -\frac{396.5 \text{GeV}}{m_\chi}, \quad (5.11)$$

$$\lambda_4 = \frac{1}{2v^2} (2M_A^2 - 4M_{H^+}^2 + M_{S_1}^2 + M_{S_2}^2 + (M_{S_1}^2 - M_{S_2}^2) \cos(2\theta)) \sim -0.60, \quad (5.12)$$

$$\lambda_5 = -\frac{1}{2v^2} (2M_A^2 - M_{S_1}^2 - M_{S_2}^2 + (M_{S_2}^2 - M_{S_1}^2) \cos(2\theta)) \sim -0.60, \quad (5.13)$$

$$\lambda_3 = \lambda_1 - \lambda_4 - \lambda_5 \sim 1.46. \quad (5.14)$$

6 Comparisons with non-collider experiments

6.1 Direct detection

6.2 Direct Detection

The DD constraints for the scalar and pseudoscalar mediator scenario are very different. While the scalar features an unsuppressed SI scattering cross section, the pseudoscalar cross section is highly suppressed at tree level such that the dominant contribution arises from loop graphs.

6.2.1 Scalar

We will generate DD constraints using the 2016 LUX [?] and XENON1T [?] data, via an effective operator approach using tools from [?]. The scattering of DM with nuclei will be dominated by the tree-level exchange of S_1 and S_2 , resulting in a spin-independent scattering cross section. The only relevant nucleon operator is

$$O_1^N = \bar{\chi}\chi\bar{N}N, \quad (6.1)$$

and, by integrating out the mediators, we obtain a coefficient of [?]

$$c_N = m_N \frac{y_\chi \cos \theta \sin \theta}{v} \left(\frac{1}{M_{S_1}^2} - \frac{1}{M_{S_2}^2} \right) \left(f_{T_u}^N \epsilon_u + \epsilon_d \sum_{q=d,s} f_{T_q}^N + \frac{2}{9} f_{T_g} \frac{2\epsilon_u + \epsilon_d}{3} \right). \quad (6.2)$$

As there are contributions from exchange of the two scalars, with a relative negative sign, there is the possibility for destructive interference when the masses of S_1 and S_2 are comparable. In addition, depending on the choice of Yukawa structure, it is possible to have destructive interference between the up-type quarks and the down-type quarks in the nucleon. For the Type I and Type II Yukawa structure, the coefficients become

$$c_N^{\text{type I}} = m_N \frac{y_\chi \cos \theta \sin \theta}{v \tan \beta} \left(\frac{1}{M_{S_1}^2} - \frac{1}{M_{S_2}^2} \right) \left(\sum_{q=u,d,s} f_{T_q}^N + \frac{2}{9} f_{T_g} \right), \quad (6.3)$$

$$c_N^{\text{type II}} = m_N \frac{y_\chi \cos \theta \sin \theta}{v} \left(\frac{1}{M_{S_1}^2} - \frac{1}{M_{S_2}^2} \right) \left(f_{T_u}^N \cot \beta - \tan \beta \sum_{q=d,s} f_{T_q}^N + \frac{2}{9} f_{T_g} \frac{2 \cot \beta - \tan \beta}{3} \right). \quad (6.4)$$

For the Type II scenario, we see that the presence of destructive u - d interference is clearly visible in the right-hand bracket of 6.4. There is no such interference for Type I. If we adopt the values of f_{T_i} obtained by [?], we find that a ratio of $\epsilon_u \sim -1.6\epsilon_d$ (corresponding to $\tan \beta = \sqrt{|\frac{\epsilon_d}{\epsilon_u}|} \sim 0.8$ in a Type II scenario) will result in exact cancellation of the DD signal.

In Figure 70 we show the current DD exclusion from LUX [?] and XENON1T[?] together with the projections for XENON1T, XENONnT projections [?]. We also show the sensitivity for a cross section equivalent to the “neutrino floor” [?]. We find

that DD excludes significant parameter space, unless the scalar masses are approximately degenerate. This can be seen in all 4 panels of Figure 70 where we see a narrow allowed region near $M_{S_1} \sim M_{S_2}$, between excluded regions at higher and lower M_{S_1} values. The excluded region in the upper LH plot (Type I) is somewhat larger than in the lower LH plot (Type II) lower due to the additional interference effect for the latter. Increasing $\tan\beta$ weakens the constraints for Type I because $|\epsilon_d| = |\epsilon_u| = 1/\tan\beta$ (upper right) and strengthens them for Type II because $|\epsilon_d| = |1/\epsilon_u| = \tan\beta$ (lower right).

6.3 Pseudoscalar

At tree level, the spin-independent scattering cross section is absent. The spin-independent cross section is non-zero, but highly suppressed due to a dependence on q_{tr}^4 . At loop level, however, a spin-independent cross section is generated through the diagrams in Fig. 71. The triangle diagrams in the left panel of Fig. 71 are proportional to m_q while the box diagrams in the central and right panels of Fig. 71 are proportional to m_q^3 , thus the box diagrams are sub-leading as found in [?] (except for Type II with $\tan\beta \gtrsim 50$). The triangle diagram does not depend on the Yukawa sector of the 2HDM. ** cite our paper in preparation**

Similarly as in the scalar model, in the PS model the mixing arises through a term $ib_P P\Phi_1^\dagger\Phi_2 + h.c.$. The resulting mixing angle is defined by

$$b_P = -\frac{(M_A^2 - M_a^2)\sin 2\theta}{2v} \quad (6.5)$$

The low energy effective operator generated at 1 loop is

$$\mathcal{L}_{eff} = -\frac{y_\chi^2 m_q m_\chi}{16\pi^2 m_h^2 v^2} G\left(\frac{m_\chi^2}{M_A^2}, \frac{m_\chi^2}{M_a^2}, \frac{m_h^2}{m_\chi^2}, \theta\right) \bar{\chi}\chi\bar{q}q \quad (6.6)$$

$$G(x, y, z, \theta) = F_1(x)\sin^2\theta\hat{\mu}_{AAh} + F_1(y)\cos^2\theta\hat{\mu}_{aah} + F_2(x, y)\sin 2\theta\hat{\mu}_{Aah} \quad (6.7)$$

$$F_1(x) = \int_0^1 dz \frac{x(1-z)z}{xz^2 - z + 1} = \frac{(6x - 2)\log\left(\frac{\sqrt{1-4x}+1}{2\sqrt{x}}\right) + \sqrt{1-4x}((x-1)\log(x) - 2x)}{2\sqrt{1-4x}x} \quad (6.8)$$

$$\begin{aligned} F_2(x, y) &= \int_0^1 dz \frac{xyz\log\left(\frac{xyz^2-yz+y}{xyz^2-xz+x}\right)}{y-x} \\ &= \frac{1}{4xy(x-y)} \left(x^2((2y-1)\log(y) - 2y) + x^2\sqrt{1-4y} \left(\log(4y) - 2\log\left(\sqrt{1-4y} + 1\right) \right) \right. \\ &\quad \left. - 2xy^2(\log(x) - 1) + y^2\log(x) + \sqrt{1-4xy}^2 \left(2\log\left(\sqrt{1-4x} + 1\right) - \log(4x) \right) \right) \end{aligned} \quad (6.9)$$

where the coefficients μ are given in terms of either the couplings in the $\Phi_{1,2}$ basis or in the $\Phi_{h,H}$ basis (indicated as $\hat{\mu}$), respectively:

$$\mu_{AAh} = z \left(\cos^2\theta - \frac{2\lambda_3 v^2}{m_h^2} \right), \quad (6.11)$$

$$\mu_{aah} = -\frac{1}{2}\sin(2\theta) \left(\frac{1}{x} - \frac{1}{y} + z \right), \quad (6.12)$$

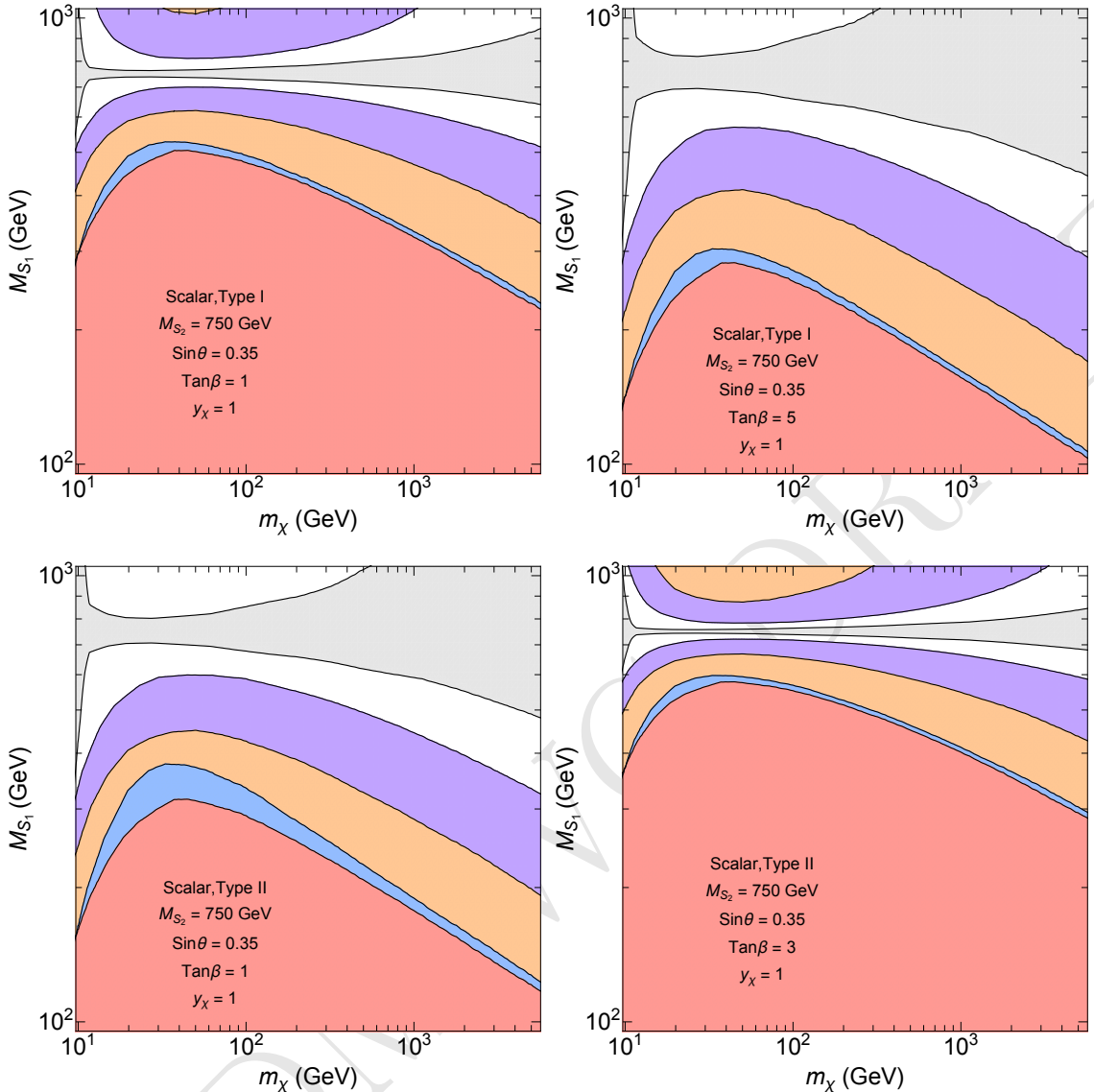


Figure 70: DD exclusion and projections for various experiments for the Scalar model. The various regions refer, in order, to LUX [?], XENON1T[?], XENON1T and XENONnT projections [?], and neutrino background [?]. The mixing angle is set to $\sin \theta = 0.35$, but results are equivalent also for $\cos \theta = 0.35$, while $M_{S_2} = 750\text{GeV}$ in all the panels.

$$\mu_{aah} = 2 \sin^2(\theta) \left(\frac{1}{x} - \frac{1}{y} + \frac{z}{2} \right) - z \frac{2\lambda_3 v^2}{m_h^2}, \quad (6.13)$$

$$\hat{\mu}_{AAh} = -\frac{1}{2} \sin^2(2\theta) \left(\frac{1}{x} - \frac{1}{y} \right) - z \frac{\hat{\lambda}_{34-5} v^2}{m_h^2} \cos^2 \theta - z \frac{2\hat{\lambda}_{P_1} v^2}{m_h^2} \sin^2 \theta, \quad (6.14)$$

$$\hat{\mu}_{Aah} = -\frac{1}{4} \sin(4\theta) \left(\frac{1}{x} - \frac{1}{y} \right) + \frac{z}{2} \frac{(\hat{\lambda}_{345P} - 2\hat{\lambda}_{P_1}) v^2}{m_h^2} \sin(2\theta), \quad (6.15)$$

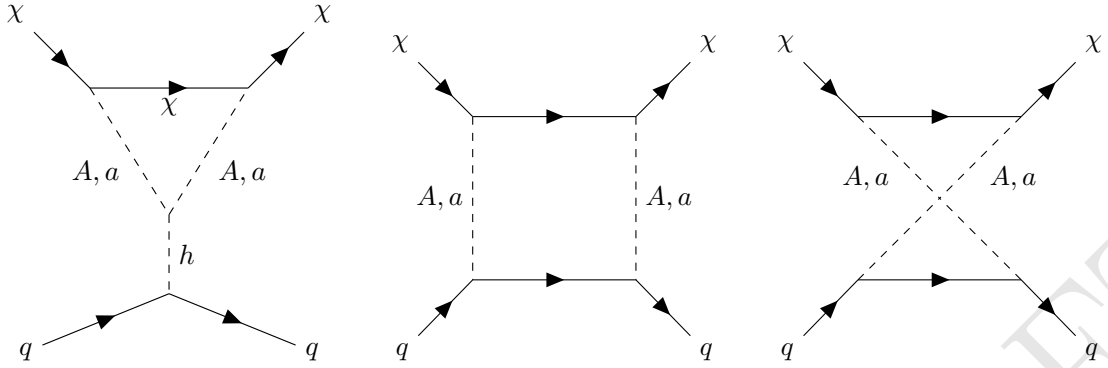


Figure 71: Spin-independent DM-nucleon scattering arises from the loop exchange of the mixing pseudoscalar mediators. Left panel: triangle diagrams. Central and right panel: box diagrams.

$$\hat{\mu}_{aah} = \frac{1}{2} \sin^2(2\theta) \left(\frac{1}{x} - \frac{1}{y} \right) - z \frac{\hat{\lambda}_{34-5} v^2}{m_h^2} \sin^2 \theta + z \frac{2\hat{\lambda}_{P_1} v^2}{m_h^2} \cos^2 \theta, \quad (6.16)$$

The coefficient μ have been written under the assumption of alignment, and imposing $M_A = M_H = M_{H^+}$ and $\lambda_3 = \lambda_{P_1} = \lambda_{P_2}$, while the coefficients $\hat{\mu}$ are using no assumption other than the alignment condition. The interference structure arising from gauge invariance is only manifest in the latter case. Note that the terms proportional to z arise from the terms in the 2HDM potential proportional to $\lambda_{1,2,3,4,5,P_1,P_2}$ ⁷, and in general their coefficient will depend on all these couplings and the value of $\tan \beta$. However, here we consider two example cases: the first one, where $\hat{\lambda}_{34-5} = \hat{\lambda}_3 + \hat{\lambda}_4 - \hat{\lambda}_5 = \hat{\lambda}_1 = \frac{m_h^2}{v^2}$ and $\hat{\lambda}_{P_1} = \hat{\lambda}_{P_2} = 0$, and the second one with $\lambda_3 = \lambda_{P_1} = \lambda_{P_2} = 3$ and $\lambda_{4,5}$ set by the condition $M_H = M_A = M_{H^+}$.

DD for the pseudoscalar model are presented in Fig. 72 and 73 for the first and second benchmark point respectively. Limits are calculated using 6.6. The heavier pseudoscalar is set to $M_A = 750\text{GeV}$, and the mixing angles are fixed to $\sin \theta = 0.7$ in the left panel, $\sin \theta = 0.35$ in the right panel and $\cos \theta = 0.35$ in the bottom panel. In the first case, current limits are able to exclude the portion of parameter space with $20\text{GeV} \lesssim m_\chi \lesssim 200\text{GeV}$ and $M_a \lesssim 40\text{GeV}$. Projected limits for XENON1T and XENONnT could expand the excluded region to $10\text{GeV} \lesssim m_\chi \lesssim 1\text{TeV}$ and $M_a \lesssim 150\text{GeV}$. The presence of the neutrino floor will prevent to be able to probe this model for $M_a \gtrsim 300\text{GeV}$ or $m_\chi \gtrsim 3\text{TeV}$ with conventional DD experiments. The second case is quite similar to the first, with the limits just slightly weakened by the smaller mixing angle. In the last case, for $\cos \theta = 0.35$, current DD experiments can only probe a tiny portion of the parameter space, with $20\text{GeV} \lesssim m_\chi \lesssim 70\text{GeV}$ and $M_a \lesssim 4\text{GeV}$. We can see that indeed the whole region ruled out by DD is contained in the region ruled out by Higgs width constraints. Projected limits expand the range to up $M_a \sim 40\text{GeV}$ and $m_\chi \sim 400\text{GeV}$, while neutrino background makes inaccessible to DD the region beyond $M_A \gtrsim 100\text{GeV}$ or $m_\chi \gtrsim 1\text{TeV}$. In the 3 panels we also report limits from Higgs invisible BR [? ?], coming from 2 and 3 body decays, as described in [?]. They rule out the low m_χ, M_a mass region.

⁷Relations between $\hat{\lambda}_i$ and λ_i can be found in [?].

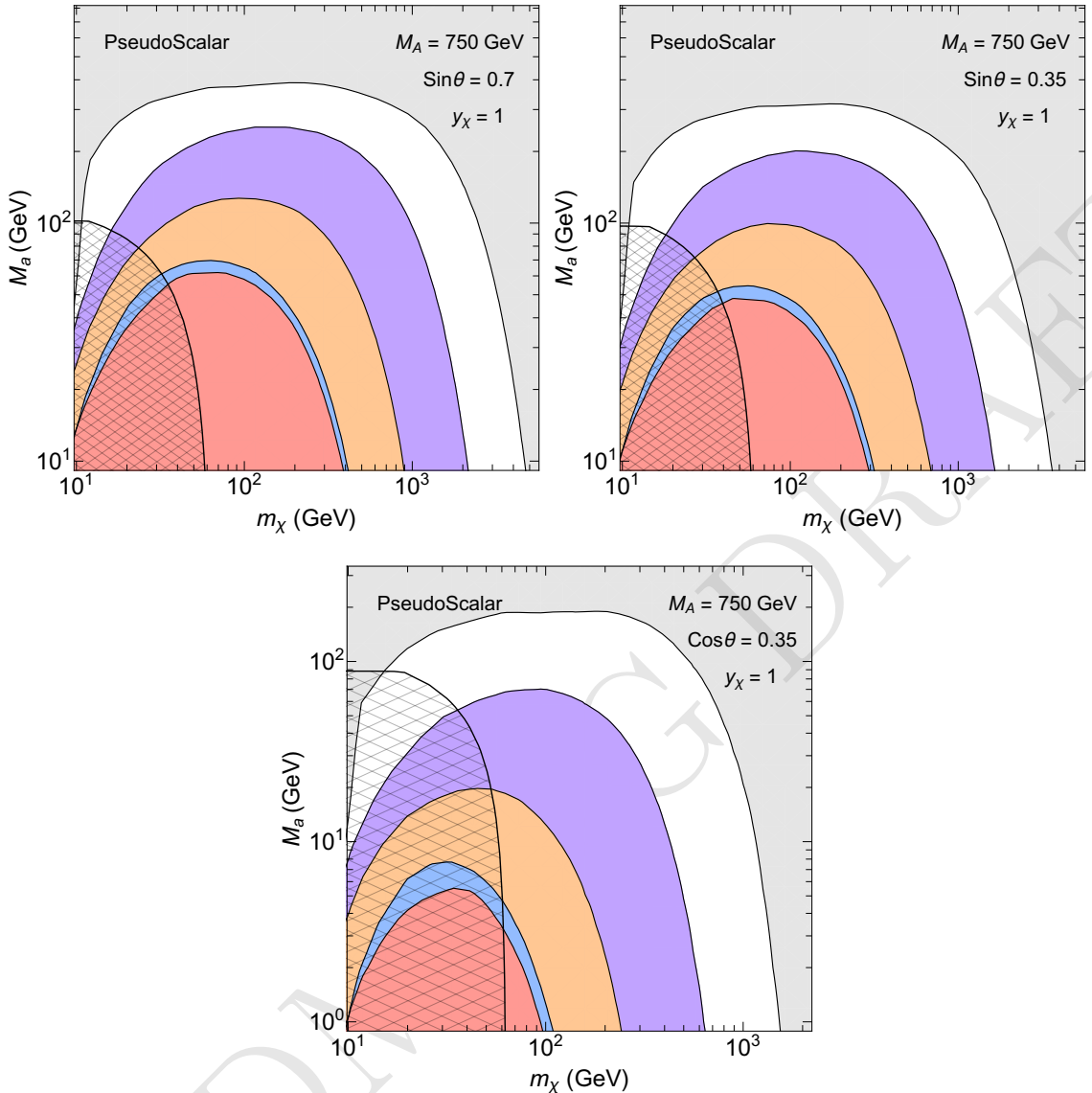


Figure 72: DD exclusion and projections for the first benchmark point for various experiments for the Pseudoscalar model. The various regions refer, in order, to LUX [?], XENON1T[?], XENON1T and XENONnT projections [?], and neutrino background [?]. Top Left panel uses $\sin \theta = 0.7$, top right panel uses $\cos \theta = 0.35$, bottom panel uses $\cos \theta = 0.35$, while $M_A = 750\text{GeV}$ in all the panels.

6.4 Indirect detection

Indirect detection signals for this model are quite complex, as an increasing number of distinct event topologies become kinematically accessible as well scan from light to heavy Dark Matter masses. Not only can the DM annihilate to various pairs of standard model particles, we see from figure 24 there are two more types distinct types of event topologies

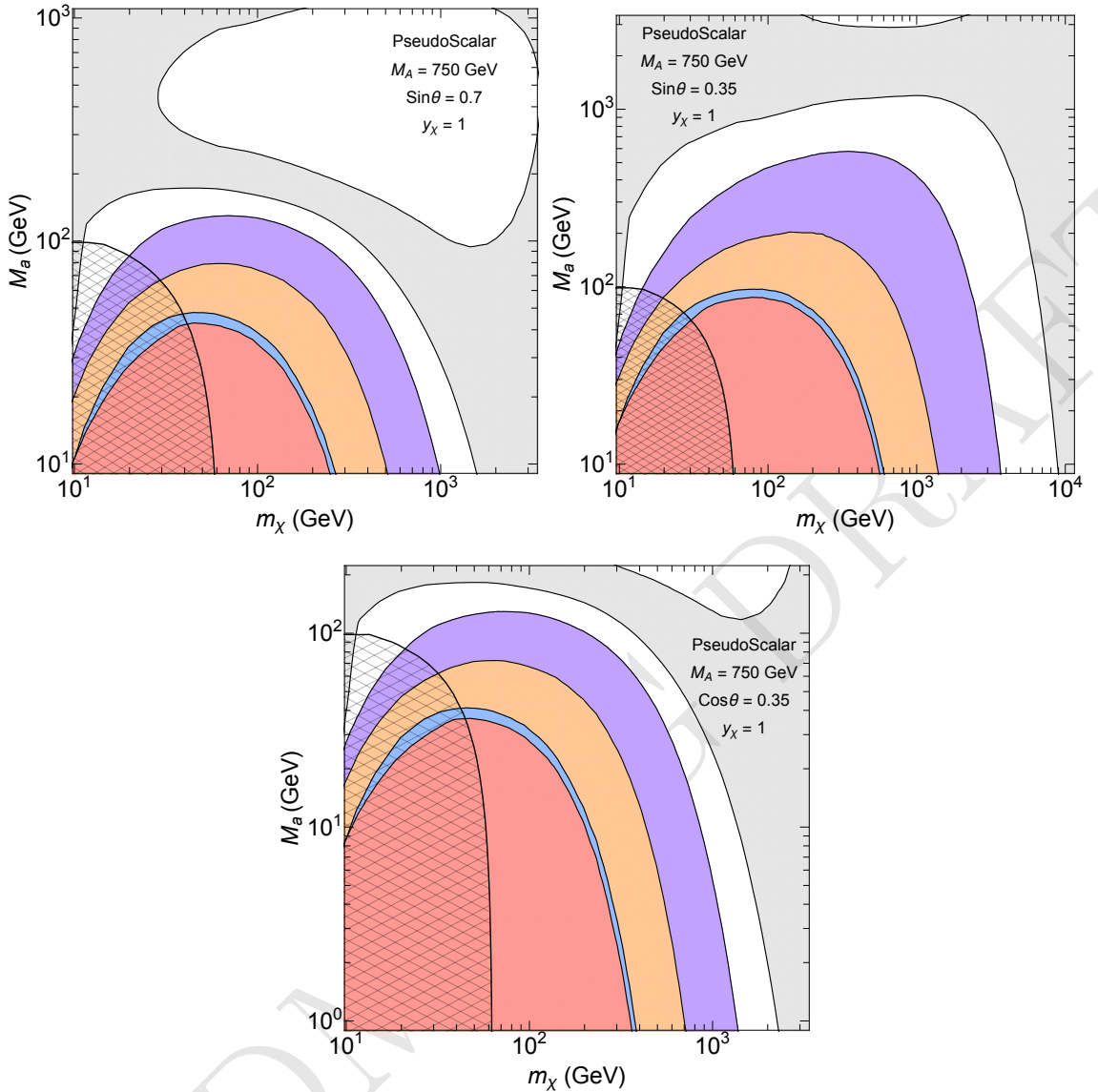


Figure 73: DD exclusion and projections for the second benchmark point for the first benchmark point for various experiments for the Pseudoscalar model. The various regions refer, in order, to LUX [?], XENON1T[?], XENON1T and XENONnT projections [?], and neutrino background [?]. Top Left panel uses $\sin \theta = 0.7$, top right panel uses $\cos \theta = 0.35$, bottom panel uses $\cos \theta = 0.35$, while $M_A = 750\text{GeV}$ in all the panels.

with characteristic kinematics that change the number of final-state Standard Model particles in the event. There are processes where a single SM particle is produced in association with an unstable Higgs sector particle, and processes where two Higgs sector particles are produced which decay to 4 SM particles. Here we briefly describe the important mass thresholds involved in the processes. In many points in parameter space several annihilation channels will contribute to over-all photon flux and limits obtained from flux observation

will require that these distinct spectra using a method similar to reference [?]. The total photon flux expected from DM annihilations will be

$$\Phi_\gamma = \frac{1}{4\pi} \sum_f \frac{\langle \sigma v \rangle_f}{2m_\chi^2} \int_{E_{\min}}^{E_{\max}} \left(\frac{dN_\gamma}{dE_\gamma} \right)_f dE_\gamma J, \quad (6.17)$$

where the the J-factor ($\text{GeV}^2\text{cm}^{-5}$) is the line of sight integral of the DM density ρ , integrated over a solid angle: $\Delta\Omega$, m_χ is the Dark Matter mass, and we must sum over all accessible partial annihilation rates $\langle \sigma v \rangle_f$, where f specifies the distinct final state. These predictions of total integrated flux may then be compared to observational measurements, for example of dwarf galaxies or the galactic center, which may constrain the partial annihilation rates and thus provide limits on the model parameters. In reference [?], complex models with several annihilation channels was constrained using the Fermi dwarf galaxy data, where the observations of each dwarf galaxy have stacked in a joint-likelihood analysis. Such a procedure would be optimal for setting limits on this model from existing observational data. Below we briefly describe the effect of various mass thresholds on the admixture of partial annihilation rates in our model.

For light Dark Matter masses, under about a 200 GeV threshold, the annihilation rate is dominated by b-quark pairs, as are the kinematically accessible particles that have the largest Yukawa coupling. This situation is a lot like the domination of a light Higgs boson decay rate by bottom quarks, though the Yukawa is not particularly large, it is the only non-hopeless kinematically accessible decay. A new annihilation into a Higgs and Z boson opens up when the threshold $m_{DM} \rightarrow m_h + m_Z$ is crossed. The next threshold to be crossed is $m_{DM} \rightarrow m_t$, where the di-top channel opens which may now dominate the annihilation rate. The next threshold to be crossed $2m_{DM} \rightarrow m_a + m_h$, where the light pseudo-scalar will decay to bottom quarks. The event is thus likely $2m_{DM} > 4b$, however the momentum distribution between the two pairs of bottoms will be asymmetric. It is expected that the total annihilation rate into this channel is appreciable since there is a large coupling between the Higgs and the pseudoscalar which also involves mass insertion. This type of event topology, $DMDM \rightarrow X + SM$, where X is a decaying hidden sector particle, has not been well studies on its own. New Higgs sector decays will open up as the threshold $2m_{DM} > m_V + m_H$ is crossed where V is the mass of a heavy vector boson, and H is a heavier Higgs sector field. Along with this the production models will begin to open in which the DM annihilated to two Higgs sector fields. The most important, and lowest threshold is $m_{DM} \rightarrow m_a$, where the annihilation channel into two pseudoscalars will open. After this threshold, we may cross the Threshold where DM annihilated to any pair of heavy(or one heavy and one light) Higgs sector field.

A few general notes are in order here. First, the effect of the new annihilation channels opening as thresholds are crossed may be witnesses in figure 26 which charts the relic density as a function of DM mass for fixed values of the Higgs-sector parameters. WE can see, for example, the effect of the di-top channel turning on as the overall annihilation rate is enhanced and the relic density drops. We see a similar powerful effect as the threshold $2m_{DM} \rightarrow m_a + m_h$ is crossed. The dramatic drop in relic density demonstrates that this is

an important annihilation channel which can compete or even dominate the ;list of partial annihilate rates. We also note the enhancement of the annihilate rate as the resonance thresholds $2m_{DM} = m_a, m_A$ are crossed, which will lead to stronger constraints from total photon flux measurements. Finally we note that the complexity of kinematics displayed in this model has not yet been well studies for models of DM annihilations. Some work has been done regarding shifts in the annihilation spectrum resulting a very symmetric process where DM pairs annihilate to 2 or more identical heavy states that then decay to pairs of SM particles [?]. Our model presents this as a possible annihilation process, along with others which have not yet been analysed. These include the asymmetric process where 2 decaying Higgs sector particles of differing masses are produced *and other asymmetric processes where light SM particle is produced in association with a heavier Higgs sector particle.* *The full parameter space of this model presents a wide area of admixtures of annihilation channels, and thus many possibilities for total integrates photon spectra.*

7 Conclusions